ELASTIC AND STRUCTURAL PROPERTIES OF SUPPORTED POROUS SILICON LAYERS

GORDON TODD ANDREWS

001311

ELASTIC AND STRUCTURAL PROPERTIES OF SUPPORTED POROUS SILICON LAYERS

By

©Gordon Todd Andrews

B.Sc. (Hons.), M.Sc., Memorial University of Newfoundland

A THESIS SUBMITTED TO THE SCHOOL OF GRADUATE
STUDIES IN PARTIAL FULFILLMENT OF THE
REQUIREMENTS FOR THE DEGREE OF
DOCTOR OF PHILOSOPHY

DEPARTMENT OF PHYSICS
MEMORIAL UNIVERSITY OF NEWFOUNDLAND
JANUARY 1999

ST. JOHN'S   NEWFOUNDLAND

Abstract

Brillouin spectroscopy has been used to investigate the elastic properties of (111)-oriented $\pi - Si$ samples formed from p^- and p^+ type $c - Si$ substrates. In the frequency regime studied, Brillouin spectra of low porosity (28%-40%) p^+ samples consist of a single set of inelastic peaks due to the surface acoustic wave. These surface waves were found to have velocities which are significantly lower than the corresponding $c - Si$ velocity, and, for samples of a given set, decreased with increasing porosity, ξ. Removal of the thin native oxide film present on low porosity p^+ type samples by an HF dip, results in a 3%-6% decrease in surface acoustic wave velocity compared to pre-dip values. Adsorbed water on the porous silicon surface appears to have no measurable effect on the surface acoustic wave velocity.

Complete sets of elastic constants for several low porosity layers formed from p^+ type substrates were determined from the directional dependence of the surface acoustic wave velocity in the (111) plane. The elastic constants C_{ij}, were found to be much smaller than those for $c - Si$ and, for a given set, decreased with increasing porosity. Empirical fitting of expressions of the form $C_{ij}^{\pi-Si} = C_{ij}^{c-Si}(1-\xi)^{m_{ij}}$ to the experimental data leads to the following relations for the porosity dependence of the elastic constants:

$$
\begin{aligned}
C_{11}^{\pi-Si} &= 168.5(1-\xi)^{3.00} \\
C_{12}^{\pi-Si} &= 62.6(1-\xi)^{6.23} \\
C_{44}^{\pi-Si} &= 79.0(1-\xi)^{2.30}.
\end{aligned}
\qquad (0.1)
$$

The exponents m_{11}, m_{12} and m_{44} differ from those of porous samples formed from p^- type substrates. This is attributed to microstructural differences between porous layers formed from p^- and p^+ type substrates. In addition, Young's modulus values were calculated

from the elastic constants and compared with those determined in other experiments. In contrast to other studies, elastic anisotropy is taken into account.

A limited number of Brillouin spectra was also obtained from intermediate porosity (50% and 60%) samples fabricated from p^- type substrates. These spectra exhibited multiple broad Brillouin peaks at relatively low frequency shifts ($< 15\ GHz$) and are qualitatively similar to those collected by Beghi *et al.* from samples with similar porosity formed from p^- type substrates.

The structural and light-emitting properties of $\pi - Si$ prepared from p^- and p^+ type (111)-oriented $c - Si$ substrates have been studied using Raman scattering. A detailed analysis of the Raman lineshapes was performed using a phonon confinement model with realistic longitudinal and transverse optic phonon dispersion curves. This model basically explains the reduced Raman shifts and asymmetric broadening of the Raman peaks in the porous silicon samples of the present work. Characteristic nanocrystallite sizes and shapes were determined for samples with porosities in the range 35% to 80%. The highly porous samples consist of fine Si spheres, while those of lower porosity are primarily wire-like. The photoluminescence spectra are less size-sensitive than the Raman spectra and no clear correlation between the Raman scattering structural information and the photoluminescence spectra has been observed.

Acknowledgements

I would like to thank my supervisors, Dr. M.J. Clouter and the late Dr. H. Kiefte, for their guidance throughout the course of this research and for sharing their expertise in the field of laser light scattering. My appreciation is also extended to Dr. J. Zuk who introduced me to porous silicon and collaborated with me on this interesting project.

I would also like to express my gratitude to Dr. N.H. Rich for help with the Raman scattering experiments and to Dr. J. Dutcher of the University of Guelph for advice on the experimental setup for surface Brillouin scattering and for the use of his Brillouin scattering apparatus. Thanks also to Dr. E. Nossarzewska-Orlowska for providing high quality porous silicon samples and Dr. Joe Hodych and Ms. Pam King of Memorial's Department of Earth Sciences for their assistance in native oxide removal. I would also like to thank my friends in the light scattering group - Dr. R. Goulding, Dr. C. Tulk and Dr. E. Grigoriants for stimulating discussions which often bordered on argument.

Finally, I would like to express my gratitude to Shelley for her patience and support and to my family for their encouragement during the writing of this thesis.

Table of Contents

List of Tables

List of Figures

xii

List of Abbreviations

$\alpha - Si$ - amorphous silicon

CDAS - computerized data acquisition and stabilization system

$c - Si$ - crystalline silicon

FTIR - Fourier transform infrared

FSR - free spectral range

$\pi - Si$ - porous silicon

PL - photoluminescence

RSW - Rayleigh surface wave

SAW - surface acoustic wave

SEM - scanning electron microscope

List of Symbols

η - anisotropy factor

J - anodization current density

B - bulk modulus

V_B - bulk phonon velocity

C - contrast

ρ - density

μ - dipole moment

l_i - direction cosines

$\vec{u}$ - displacement vector

C_{ij} - elastic constants

$\vec{E}$ - electric field

F - finesse

Γ - full width at half-maximum

θ_i - incident angle

$\vec{k}$ - light wavevector

L - nanocrystallite size

$\omega(q)$ - optic phonon dispersion relation

α - polarizability tensor

ξ - porosity

h - porous layer thickness

$\omega^{\pi-Si}$ - porous silicon Raman shift

$\vec{r}$ - position vector

n - refractive index

ρ_r - relative density

R - resistivity

γ - scattering angle

f_R - surface acoustic phonon frequency

V_R - surface acoustic phonon velocity

q_R - surface acoustic phonon wavevector

Chapter 1

Introduction

1.1 Porous Silicon

1.1.1 Historical Overview

Porous silicon ($\pi - Si$) was discovered inadvertently by Uhlir [1] in 1956 while he was trying to develop a technique for the smoothing and shaping of silicon using electrochemical etching with hydrofluoric acid (HF) as the electrolyte. He found that for certain combinations of etching current density and HF concentration his samples became covered with a matte black, brown or red film on the surface. In 1958, Turner, who was also studying the electropolishing of silicon in HF solutions, suggested that these films might be porous because he observed no discontinuity in the electrochemical cell resistance with film formation [2].

In the three decades following the initial discovery, the relationship between the formation conditions and the morphological and electronic properties of the resulting films was investigated in detail [3-8]. Collectively, these studies showed that the films consisted of a fragile crystalline silicon skeleton with an intricate network of minute pores. From an applications standpoint, the primary interest in $\pi - Si$ during this period was in its use in the dielectric isolation of devices in integrated circuits [3, 9, 10]. This was because it could be produced on the same silicon wafer as the electronic components and it could also be oxidized much more easily than crystalline silicon ($c - Si$) to form a thick insulating film [10].

1

Systematic investigation of the optical properties of $\pi - Si$ began in the mid-1980s. In 1984, Pickering *et al.* [11] performed photoluminescence (PL) measurements at liquid helium temperatures on $\pi - Si$ samples with a range of resistivities. They noted that some of their samples exhibited an intense broad PL peak at energies significantly above the $c - Si$ band gap (~ 1.1 eV) [11]. The energy of this peak was seen to be dependent on the density (*i.e.*, porosity) of the $\pi - Si$ layer. These low temperature results were reproduced for $\pi - Si$ films formed from p^- and p^+ type Si substrates by Canham [12] in 1990. (It should be noted that in this work, the notations p^+ and n^+ refer to samples with resistivities $< 0.05\ \Omega\cdot$cm while p^- and n^- denote samples with resistivities $> 0.05\ \Omega\cdot$cm). The most important finding of Canham's work, however, was the discovery of strong visible luminescence from high porosity $\pi - Si$ at room temperature. This was suggested to be due to a widening of the Si band gap from the infrared to the visible region of the spectrum. Evidence for an increased band gap was also observed in the optical transmission experiments of Lehmann and Gosele [13] who found that p^- type $\pi - Si$ was translucent to visible light. In both cases, the increase in band gap energy was attributed to two-dimensional quantum confinement in the nanometer-size Si regions or wires believed to make up the porous layers.

The discovery of strong visible PL from $\pi - Si$ and the suggestion that it was due to quantum confinement of carriers in tiny Si nanostructures started a flurry of activity in $\pi - Si$ research. Many groups quickly duplicated Canham's results and subsequent fundamental studies have been largely directed toward understanding the origin of the luminescence. Basic studies aimed at characterizing other properties of $\pi - Si$ are also being carried out. From a technological perspective, the principal goal is the development of new optoelectronic devices which may be incorporated into Si integrated circuits. There are also numerous potential applications of $\pi - Si$ in photovoltaic cells [14], biomaterials [15] and biosensors [16]. A review of the properties and possible uses of $\pi - Si$ may be

2

found in several excellent papers [17-19].

1.1.2 Formation and Characteristic Morphologies

Porous silicon is usually formed by the electrochemical anodization of $c - Si$ in hydrofluoric acid electrolytes (although it can also be formed by chemical dissolution and spark erosion) $i.e.$, by electrochemical etching. Pore formation occurs at lower current densities and higher HF concentrations than those required for the electropolishing of Si ($e.g.$, typical values used for preparation of the samples in the present work were ~ 10 mA·cm^{-2} and $\sim 43\%$) and involves complicated physical and surface-chemical phenomena which are still not completely understood [20, 21]. A discussion of recent models of pore formation may be found in the comprehensive review by John and Singh [21].

The morphology of $\pi - Si$ can be described as a delicate network of nanometer-size "wires" or spherical Si crystallites. X-ray diffraction investigations [22] indicate that these nanocrystallites retain the structure of the Si substrate, but with a small lattice expansion compared to bulk $c - Si$. The detailed nature of the porous layer, however, depends on several factors including dopant type and concentration, anodization current density and electrolyte composition.

The effect of dopant type and concentration of the starting Si wafer on the morphology of the resulting $\pi - Si$ layer has been well-studied [5, 20, 23, 24]. In fact, the resultant morphologies are so strongly dependent on these variables that they are often divided into groups on this basis (p^-, p^+, n^-, n^+). A $\pi - Si$ layer fabricated from a p^- type Si substrate typically exhibits a homogeneous and highly interconnected random pore network (in the sense that no obvious preferred direction of pore propagation is observed), resulting in a sponge-like structure [5, 20]. This structure has also been described as an interconnected network of nanometer sized Si ligaments [24]. The pore diameters and interpore spacings are very small, with characteristic sizes lying between
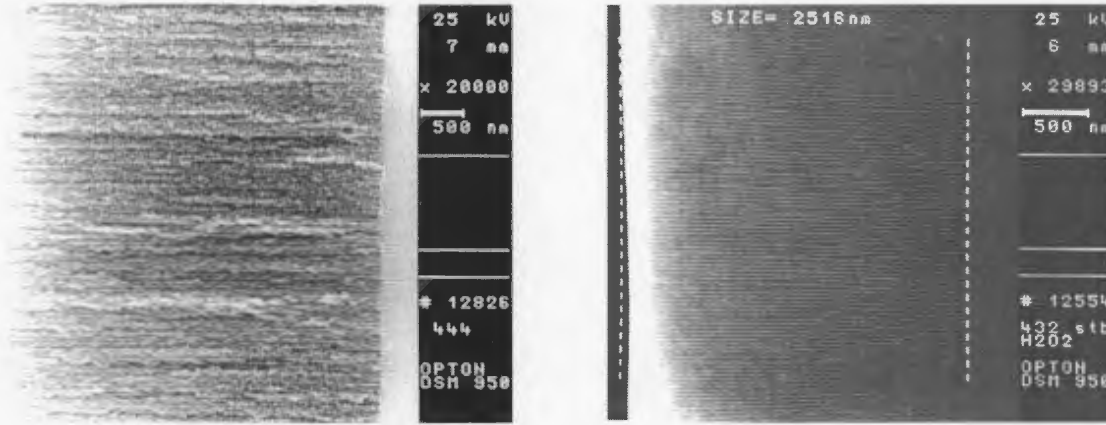
Figure 1.1: SEM photographs of p^+ (left) and p^- type (right) $\pi - Si$. Channel formation can be clearly seen in the p^+ type sample.

1 nm and 5 nm. For $\pi - Si$ formed on p^+ type $c - Si$ substrates, channel formation occurs in conjunction with significant sidebranching. The pore diameters and interpore spacings are larger than those of p^- type $\pi - Si$, with dimensions in the range 5 nm-15 nm [7, 8, 20]. The pore dimensions for both p^- and p^+ type $\pi - Si$ are characteristic for a large range of anodization current densities and HF concentrations. The differences in the nanostructures are clearly shown in the scanning electron microscopy (SEM) pictures of Figure 1.1.

The pore morphologies and diameters observed in $\pi - Si$ formed from n^+ type substrates are similar to those found in p^+ type $\pi - Si$. It is more difficult, however, to make a general statement about the morphology of $\pi - Si$ formed from n^- type substrates. This is because very different morphologies have resulted from similar anodization conditions. Recent work [20] suggests that the pore diameters in n^- type Si are considerably larger than p type Si and, in contrast to the randomly directed pore network of p^- type Si, show a strong tendency to form straight channels at low dopant concentrations. This conflicts with the results of an earlier study [5] which reports a randomly-directed pore structure with a pore size similar to that found in p^- type $\pi - Si$. In general, for n^- type Si, both the pore diameter and average interpore spacing decrease with increasing dopant

concentration.

The resultant morphology of a $\pi - Si$ layer is also dependent on the anodization current density and the HF concentration. Generally, an increase in current density causes a broadening of the pore size distribution [7] as well as an increase in mean pore diameter [5, 7]. This occurs regardless of the dopant type or concentration present in the starting Si wafer, although the effect is most pronounced for n^- type $\pi - Si$ [20]. In contrast, increasing the HF concentration results in a decrease in characteristic pore size and a narrowing of the pore size distribution.

1.1.3 Definition of Porosity

One of the most common parameters used to characterize $\pi - Si$ is its porosity ξ. It is defined as the ratio of the pore volume (V_p) to the total volume (V_t) of that part of the starting Si wafer which will be converted to $\pi - Si$.

$$\xi = \frac{V_p}{V_t}. \tag{1.1}$$

The samples used in the present work have porosities lying in the range $25\% \leq \xi \leq 80\%$ which are fairly typical values. However, samples with porosities as high as $\sim 95\%$ have been prepared using the method of supercritical drying [25].

It is important to note that porosity is not necessarily a measure of nanocrystallite size. For instance, a $\pi - Si$ film consisting of large Si particles and extremely large voids could have the same porosity as a film composed of very small nanocrystals and small pores. It is true in general, however, that as the porosity increases the pore size also increases (which implies a decrease in average nanocrystallite size).

The sample porosity may be varied by changing the anodization current density and the HF concentration. As a rule, for a given HF concentration, the porosity increases

with increasing current density. For fixed current density, the porosity increases with decreasing HF concentration.

1.2 Structural and Elastic Properties of $\pi - Si$

1.2.1 Raman Scattering Studies and Structural Properties

Raman scattering has been widely used for the structural characterization of semiconductor microcrystals due to its sensitivity to crystal sizes below a few tens of nanometres. Crystallites of comparable dimensions are also present in $\pi - Si$ and so it is not surprising that this nondestructive technique has been used to obtain information about the microstructure of this material [26-38]. This information can also provide valuable insight into the mechanism for visible PL in $\pi - Si$ when combined with complementary data on the optical properties.

The first-order Raman spectrum of $\pi - Si$ usually consists of an asymmetrically broadened peak located at a Raman shift ($\Delta\omega^{\pi - Si}$) which is lower than that for the symmetric first-order peak of $c - Si$ ($\Delta\omega^{c - Si} = 520.4$ cm^{-1}). A phenomenological model [39-42] based on the spatial confinement of phonons in small structures reproduces the main features of these spectra and has been used to estimate crystallite sizes in $\pi - Si$. The first work of this kind was carried out by Sui et $al.$ [27] who performed Raman scattering experiments on light-emitting $\pi - Si$ formed from p^- type substrates. Their Raman spectra, which consisted of single asymmetric peaks with shifts in the range 508.0 cm^{-1}-510.1 cm^{-1} and linewidths between 32 cm^{-1} and 42 cm^{-1}, were compared with spectra obtained using the phonon confinement model. A quadratic approximation of the true Si longitudinal optic (LO) dispersion curve was used in the calculation. Good agreement was obtained with theoretical spectra which assumed three dimensional phonon confinement ($i.e.$, spherical crystallites) and crystallite sizes of 2.5 nm-3.0 nm.

Gregora *et al.* [31] determined nanocrystallite sizes for 70% porous layers formed from p^- and p^+ type $c - Si$ substrates. Neglecting strain-induced effects and assuming spherical crystallites, diameters of 2.6 nm-3.9 nm were obtained for p^- type samples using their one-phonon Raman spectra and a well-known relationship between the Raman shift and linewidth (a major result of the phonon confinement model). For the p^+ type samples. characteristic sizes of 4 nm-5 nm were found assuming a columnar morphology. These results were in reasonable agreement with sizes of 4.0 nm and 4.1 nm for p^- type and p^+ type samples respectively, which they obtained from their low frequency Raman scattering data.

Munder *et al.* [29] performed a detailed Raman scattering study of $\pi - Si$ layers with porosities ranging from 36% to 65%. Excellent fits to the measured spectra were obtained using a complicated fitting procedure (based on the localization of phonons in nanocrystals) which incorporated the effects of strain in the $\pi - Si$ layers and optimized a distribution of nanocrystallite diameters. For p^+ type samples with 36% porosity. the best-fit distributions displayed a monotonic decrease in the number of nanocrystals with increasing nanocrystal diameter, while for all other p^+ type samples. maxima at ~ 2.5 nm and ~ 4.0 nm were observed. The existence of such small nanocrystals in the p^+ type $\pi - Si$ layers was attributed to the formation of a nanocrystalline film all over the pore walls. It was also noted that p^+ type samples with larger porosities consisted of a greater number of nanocrystals with diameters < 3.5 nm than similarly-doped samples of lower porosity. Only crystallites with diameters of < 3.5 nm were observed in the size distributions of porous films formed on p^- type substrates.

Raman scattering has also been used in the examination of structural depth inhomogeneities in $\pi - Si$ layers. Micro-Raman spectroscopy experiments have been carried out by Inoue *et al.* [26] on cross sections of $\pi - Si$ layers formed on n^- type Si substrates to

obtain depth profiles. Typical Raman spectra were obtained (each exhibiting an asymmetrically broadened peak located at a lower Raman shift than that of $c - Si$) with the peak position changing continuously from higher to lower and the linewidth varying from narrower to broader as the probed spot approached the sample surface. These effects were ascribed to a decrease in nanocrystallite size with decreasing depth. In the region very near the surface, an anomalous reduction in the shift of the first-order Raman line was observed, suggesting that the average crystallite size in that region was much smaller than in other parts of the porous layer.

Similar results were obtained by Mariotto et al. [43] in micro-Raman experiments on $\pi - Si$ layers formed from p^- type substrates. Their spectra were analyzed in terms of contributions from various phases of Si ($\alpha - Si$, $c - Si$ and nanocrystalline). The contribution from the nanocrystalline component was evaluated using a modification of the standard phonon confinement model which assumed an inhomogeneous distribution of crystallite sizes. The results indicated that, in addition to the predominant nanocrystalline phase, an $\alpha - Si$ component was present at all depths in the layer. A reduction in crystallite size near the layer/air interface was observed but no reason for this decrease was put forth.

Monin et al. [44] also performed micro-Raman scattering investigations on p^- type $\pi - Si$. Raman spectra were collected from a region close to the substrate and close to the layer surface and again it was found that the crystallite size (calculated using the phonon confinement model) was smaller near the surface. This was stated to be due to extra chemical dissolution of the already formed wafer. No peak was observed at 480 cm^{-1}, indicating no observable contribution from an amorphous phase. In addition, no splitting of LO and TO phonons was observed.

Depth-dependent information has also been obtained by examining the variation of the Raman linewidth and shift as a function of excitation wavelength. Zhang et al. [45]

recorded Raman spectra of p^- type $\pi - Si$ excited with incident laser wavelengths ranging from the violet to near infrared. In a set of spectra from one sample, they observed a change from a single sharp peak at a Raman shift of 520 cm^{-1} for the longest excitation wavelength to a broad asymmetric feature with a tail down to shifts less than 400 cm^{-1} for the shortest incident laser wavelength used. At intermediate wavelengths, both components were present in the spectra. Because longer wavelength excitation penetrates farther into the $\pi - Si$ layer, they concluded that the sharp peak originated from the Si substrate while the asymmetric feature was intrinsic to the $\pi - Si$ layer. The characteristics of spectra from other samples, including a freestanding layer and a thicker supported layer, were consistent with this hypothesis. The narrowing linewidth and increasing Raman shift with increasing excitation wavelength also led them to conclude that the average pore size and porosity decrease (implying an increase in nanocrystallite size) with increasing depth from the surface. A narrowing linewidth and increasing Raman shift with increasing excitation wavelength was also observed in similar experiments performed on freestanding $\pi - Si$ films fabricated from p^- type substrates [46, 47]. This was attributed to a resonance of the excitation energy with the electronic states of nanocrystallites in $\pi - Si$.

The depth inhomogeneity of $\pi - Si$ layers was also studied using Raman scattering [48]. To obtain depth-resolved information about the microstructure, Raman spectra were recorded with different excitation wavelengths and therefore with different penetration depths. It was found that for p^- type $\pi - Si$ the microstructure changes from small crystallites at the surface to large crystallites at the $\pi - Si$ /substrate interface. The thinning of the structure at the surface was said to be related to the effects of chemical etching because of the increasing storage time of the topmost layers in the electrolyte. For p^+ type samples, the gradient in microstructure changed from large crystallites at the surface to smaller ones at the $\pi - Si$ /substrate interface. This was attributed to a

decrease of the HF concentration with increasing thickness of the layer.

Raman scattering has also been used in conjunction with PL spectroscopy to investigate the light-emitting properties of $\pi - Si$. Such experiments allow the dependence of the optical energy gap on nanocrystallite diameter to be determined. Knowledge of this is important in understanding the origin of the strong visible luminescence in $\pi - Si$. For instance, the physical quantum confinement model predicts an inverse relationship between the energy gap and the crystallite diameter or, equivalently, an increase in the PL peak energy with a decrease in Raman shift.

A Raman scattering and PL study of p^- type $\pi - Si$ was carried out by Tsu *et al.* [35]. Spectra were collected from three different spots on one sample and a correlation between the Raman shift of the first-order line and the corresponding PL peak energy was noted; as the Raman shift decreased, the energy of the PL peak increased. On the sample spot which yielded the highest PL peak energy, a splitting of the usual single-peak Raman spectrum into two peaks was observed. No Raman peak was observed at a shift of 480 cm^{-1}, indicating no substantial $\alpha - Si$ contribution to the Raman spectrum. They concluded that these results provided strong evidence of the existence of crystallites with sizes of 2.0 nm-3.0 nm and that the luminescence originates in these nanostructures.

Analogous experiments on similarly doped samples were carried out by Lockwood *et al.* [49]. The Raman spectra exhibited a strong asymmetric line peaked below the bulk Si optical mode, indicative of phonon confinement effects in $c - Si$. The Raman shifts and widths were found to be consistent with theoretical predictions for spherical crystallites with diameters in the range 2.7 nm-4.9 nm. An inverse relationship between the PL peak energy and the Raman-determined nanocrystallite diameter was observed in accordance with a quantum confinement mechanism for the visible PL.

Sood *et al.* [38], however, observed no decrease in the shift of the first-order Raman line concomitant with an increase in the PL peak energy in their experiments on $\pi - Si$ formed

from p^- type substrates. The Raman lineshape was calculated for cylindrical crystallites using the phonon confinement model assuming a quadratic phonon dispersion which fit the experimental dispersion relation of $c - Si$ in the $\Gamma - X$ direction of the Brillouin zone. The characteristics of the experimental Raman spectra were not consistent with the model of phonon confinement in cylindrical geometries. They stated that these observations casted doubt on quantum confinement being responsible for the visible PL in $\pi - Si$. Deak *et al.* [50], however, used the trend (a decrease in the Raman peak position correlating with a decrease in PL peak energy, with one exception) seen in these Raman spectra as evidence for a chemical confinement theory of visible PL in $\pi - Si$. In this model, the shift of the band gap is not a size effect but occurs due to chemical substitution of the bond terminators of the Si atoms and is accompanied by a parallel shift in the first-order Raman line.

1.2.2   Brillouin Scattering and Related Studies of the Elastic Properties

Much emphasis has been placed on understanding the structural, electronic and optical properties of $\pi - Si$, however characterization of the elastic properties has received little attention. Knowledge of these properties is important for many device applications as well as from a fundamental standpoint as a test of theoretical models which attempt to describe the mechanical properties of porous media.

One of the most useful techniques for investigating the elastic properties of solids is Brillouin light scattering spectroscopy. This technique has been used to study $\pi - Si$ formed on both n^+ and p^- type Si substrates [51]. For n^+ type $\pi - Si$ with porosities of 30% and 40% the Brillouin peak due to longitudinal bulk phonons travelling in the [001] direction was seen to have a lower shift and a larger linewidth than that for $c - Si$. The transverse peak, clearly evident in the $c - Si$ spectrum, was not observed in those of the $\pi - Si$ samples. In addition, the Brillouin shift of the pseudo-surface mode was

11

smaller for the $\pi - Si$ samples than for $c - Si$. It was also noted that the longitudinal sound velocity (determined using the standard Brillouin equation with the refractive index calculated from an effective medium formula) for the n^+ type samples was higher than that for $c - Si$ leading them to conclude that their samples possessed a surface layer with a thickness of the order of the skin depth (1 μm) and a porosity much lower than the nominal one. This correlated with the twofold microstructure observed in SEM cross-section pictures of their n^+ type samples. The n^+ type samples also exhibited a transition from the pseudo-surface wave to Rayleigh wave regimes with very low dispersion and small relative shifts. This observation was said to be consistent with the behaviour of the bulk modes in the same specimens.

Beghi *et al.* [51] also observed that the Brillouin spectra of high porosity p^- type samples did not show any intrinsic bulk peaks. This was suggested to be due to a crossover (with respect to the characteristic scattering length perpendicular to the surface ($\lambda/2n$)) of the vibrational spectrum from translational invariance to self-similarity with fracton bulk peaks buried in the central peak at very low frequency shifts. The experimental widths of the surface wave peaks for the p^- type $\pi - Si$ samples were found to be significantly larger than those of surface waves in $c - Si$. This was also attributed to possible crossover from surface phonons to surface fractons. In addition, the dispersion curves for the Rayleigh mode and two other modes guided by the porous layer are presented. It was suggested that the strong observed dispersion is indicative of a strong gradient in the acoustic properties (and therefore of the microstructure) of the p^- type samples.

The elastic properties of $\pi - Si$ have also been investigated using X-ray diffraction. These experiments, carried out on p^+ type $\pi - Si$, revealed that its diffraction properties were equivalent to those of a nearly perfect crystal. Young's modulus values were estimated for samples with porosities of 34%, 54% and 72% and found to be much smaller than that for $c - Si$, with the value decreasing with increasing porosity. Poisson's ratio

12

was also determined for samples with 54% porosity and found to be lower than that for $c - Si$ by a factor of ~ 3. Based on these results they concluded that the elastic properties of $\pi - Si$ are different from those of $c - Si$ ($\pi - Si$ is less stiff than $c - Si$) and that they depend on the details of the porous structure.

Microacoustic techniques (microechography and acoustic signature) have been used to study the elastic properties of relatively low porosity (20%-55%) p^+ type $\pi - Si$ [52, 53]. The thicknesses of the $\pi - Si$ layers were measured and the longitudinal, shear and Rayleigh velocities and Young's modulus were obtained. Empirical equations which relate the acoustic wave velocities and Young's modulus to sample porosity were also proposed. In another study by the same group [54], the phase velocity of the Rayleigh mode and the first two Lamb modes as functions of the product of observation frequency and thickness for a sample of 40% porosity were determined. The porosity dependence of the velocity of these three modes for fixed frequency × thickness was also presented.

Bellet *et al.* [55] used the nanoindentation technique to determine Young's modulus for 10 μm thick p^- and p^+ type $\pi - Si$ samples. They found that Young's modulus was strongly dependent on the porosity with its value decreasing drastically with increasing porosity. For p^+ type $\pi - Si$, with porosities ranging from 36% to 90%, the dependence of Young's modulus on the relative density $(1 - \xi/100)$ was found to be quadratic. Reasonable agreement was obtained between their results and the X-ray diffraction [22] and microacoustic [53] results previously mentioned. Their results also agreed with a model developed by Gibson and Ashby [56] for cellular materials which states that Young's modulus varies as the square of the relative density. They also observed that Young's modulus depends on the doping level of the wafer. For a 70% p^- type $\pi - Si$ sample the measured value was a factor of five smaller than that for a p^+ type sample of the same porosity. This difference was attributed primarily to the difference in pore structure; p^- type $\pi - Si$ having a smaller pore size and stiffness, in general. In addition, in order

to study the effect of oxidation on Young's modulus, a p^+ type sample with a porosity of 60% was anodically oxidized in a KNO_3 aqueous solution at a constant current density for 300 s. The Young's modulus of this sample was found to be $\sim$ 20% smaller than that of a corresponding unoxidized sample. This relatively small difference was ascribed to a low volume fraction of SiO_2 in the oxidized sample.

Matthai et al. [57] used a modified diffusion-limited aggregation model to simulate the structure of $\pi - Si$. The bulk modulus for a structure with 75% porosity was obtained by calculating the change in energy for a homogeneous expansion of the entire crystal structure. The cubic elastic constants C_{11} and C_{12} for the same structure were calculated in a similar fashion. The bulk modulus was found to have a value comparable to that calculated for the simulated crystal which suggested that the porous structure retained bulk Si characteristics. Along particular directions, however, the elastic properties were altered quite significantly with the shear modulus reduced to half its bulk value. It should be noted here that the values of the $c - Si$ elastic moduli obtained in this study do not correspond to accepted values. Also, it is not clear if C_{11} and C_{12} have their standard meanings.

The only work which quotes complete sets of elastic constants (C_{11}, C_{12}, C_{44}) for $\pi - Si$ is that of Cho et al. [58-60] who measured the surface acoustic wave (SAW) velocity and attenuation dispersion along the [110] direction in p^- type $\pi - Si$ with porosities lying in the range 41%-60% by phase velocity scanning of interference fringes. They found that the SAW velocity decreased with increasing porosity. The measured velocity dispersion curves for the porous samples showed remarkable agreement with the phase velocity dispersion computed assuming the elastic constants of the $\pi - Si$ films to be $x\%$ those of $c - Si$. For example, for a layer with 50% porosity, elastic constants which were 13% of the corresponding $c - Si$ value gave the best fit to the experimental data. This percentage appears to have been arbitrarily chosen so that good fits to the

14

experimental data were obtained. No physical basis for this assumption was given.

1.3   Overview of the Present Work

The present work consists of a two-part inelastic light scattering investigation of $\pi - Si$. Raman spectroscopy has been used to study the structural properties of various supported $\pi - Si$ layers formed from p^- and p^+ type Si substrates, while the elastic properties of similarly-doped films were examined using Brillouin light scattering. In the Raman scattering experiments, characteristic nanocrystallite sizes and shapes were determined from the Raman data and the standard phonon confinement model. These results are correlated with complementary PL data. The Brillouin measurements yield acoustic wave velocities which allow calculation of complete sets of elastic constants for some samples. The influence of adsorbed water and native oxide films on the velocity of SAWs in $\pi - Si$ is also investigated. In addition, the Brillouin spectra of some high porosity samples are presented and discussed.

Chapter 2

Theory

2.1 Inelastic Light Scattering in Solids

2.1.1 Basic Concepts

In an inelastic light scattering experiment, photons of energy $\hbar\omega_i$ and momentum $\hbar\vec{k}_i$ are incident on a crystal and scattered to give photons of energy $\hbar\omega_s$ and momentum $\hbar\vec{k}_s$. Raman scattering in a monatomic solid such as Si occurs when the incident photons create or destroy optic phonons in the crystal, whereas Brillouin scattering involves the creation or annihilation of acoustic phonons. In both cases, energy and momentum must be conserved, $i.e.$,

$$\hbar\omega_i = \hbar\omega_s \pm \hbar\omega \tag{2.1}$$

$$\hbar\vec{k}_i = \hbar\vec{k}_s \pm \hbar\vec{q}, \tag{2.2}$$

where ω_i, $\vec{k}_i$ (ω_s, $\vec{k}_s$) are the angular frequency and wavevector of the incident (scattered) light and ω, $\vec{q}$ are the corresponding quantities for the phonon. Thus the incident light may gain (anti-Stokes component) or lose (Stokes component) energy depending on whether a phonon is destroyed or created. Typical frequency shifts for (lattice mode) Raman scattering range from 10 cm^{-1}-1000 cm^{-1}, while Brillouin scattering frequency shifts are normally < 1 cm^{-1} [61]. It should be noted that light scattering experiments are usually carried out with visible incident light with a wavelength that is typically three orders of magnitude greater than the lattice spacing, and so only phonons near the center

16
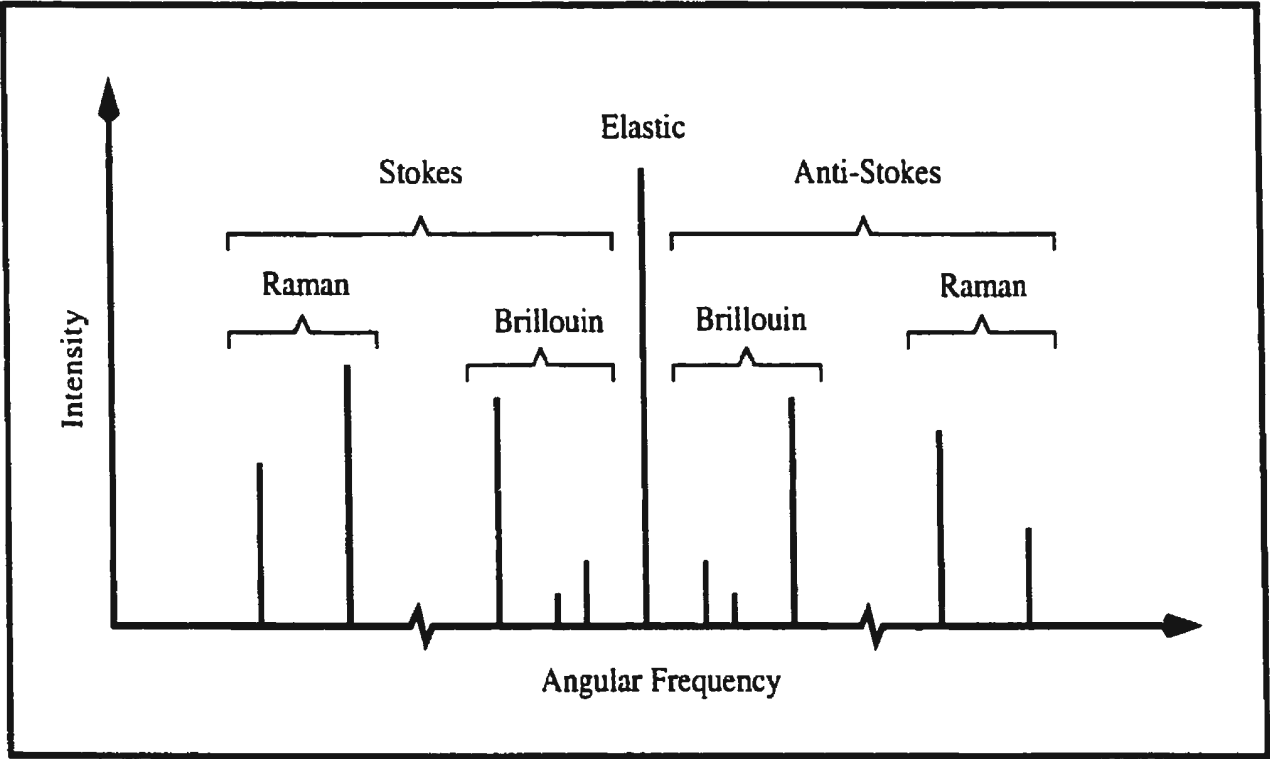
Figure 2.1: A schematic representation of the spectrum of scattered light.

of the Brillouin zone are probed. A more thorough theoretical treatment of inelastic light scattering may be found in the numerous books on the subject [61-64].

2.1.2 Raman Scattering

The first treatment of Raman scattering from optic phonons was given by Born and Bradburn in 1947 [65]. A comprehensive review of the Raman effect in crystals has also been given by Loudon [66]. The standard approach makes use of classical radiation theory to obtain the intensity of the scattered light.

When light with an electric field $\vec{E} = \vec{E}_i \cos(\omega_i t)$ is incident on a solid it induces an oscillating dipole moment $\vec{\mu}$ given by

$$\vec{\mu} = \tilde{\alpha}\vec{E} = \tilde{\alpha}\vec{E}_i \cos(\omega_i t), \qquad (2.3)$$

17

where $\vec{E}_i$ is the vector amplitude of the incident electric field and $\tilde{\alpha}$ is the second rank electronic polarizability tensor. It is usually assumed that the strongest mechanism for phonon scattering involves coupling of the light to the vibrations through the crystal electrons (*i.e.*, through the electron-lattice interaction). The polarizability is therefore affected by the crystal vibrations and varies as

$$\tilde{\alpha} = \tilde{\alpha_o} + \tilde{\alpha_1}\cos(\omega t) + \dots ,$$ (2.4)

where $\tilde{\alpha_o}$ is a property of the non-vibrating lattice and $\tilde{\alpha_1} = (\partial\tilde{\alpha}/\partial r)\Delta r$, where Δr is the vibrational normal mode amplitude. The second term on the right hand side of equation 2.4 is responsible for first-order (single-phonon) Raman scattering. Additional higher order terms contribute to multi-phonon scattering.

Substitution of equation 2.4 into 2.3 and application of a simple trigonometric identity yields

$$\vec{\mu} = \tilde{\alpha_o}\vec{E}_i \cos(\omega_i t) + \frac{1}{2}\tilde{\alpha_1}\vec{E}_i(\cos[(\omega_i - \omega)t] + \cos[(\omega_i + \omega)t]) + \dots .$$ (2.5)

This expression shows that the induced dipole moment oscillates with the angular frequency of the incident light ω_i, which leads to elastic scattering, and also at frequencies $\omega_i \pm \omega$, leading to Raman scattering. Since the intensity of the scattered light is proportional to μ^2, this results in a spectrum with a central peak due to elastic scattering and Raman peaks located at shifts of $\pm\omega$ on either side of it (see Figure 2.1). These are the Stokes ($-\omega$) and anti-Stokes ($+\omega$) components referred to earlier.

In the case of scattering from optic phonons, the intensity of the Stokes component is normally larger than that of the anti-Stokes component. This is because the anti-Stokes process requires that phonons already exist in the solid, whereas the Stokes component is due to the creation of phonons by the incident light. The intensity ratio of the two components is

$$\frac{I(+\omega)}{I(-\omega)} = e^{-\hbar\omega/k_B T},$$ (2.6)

18
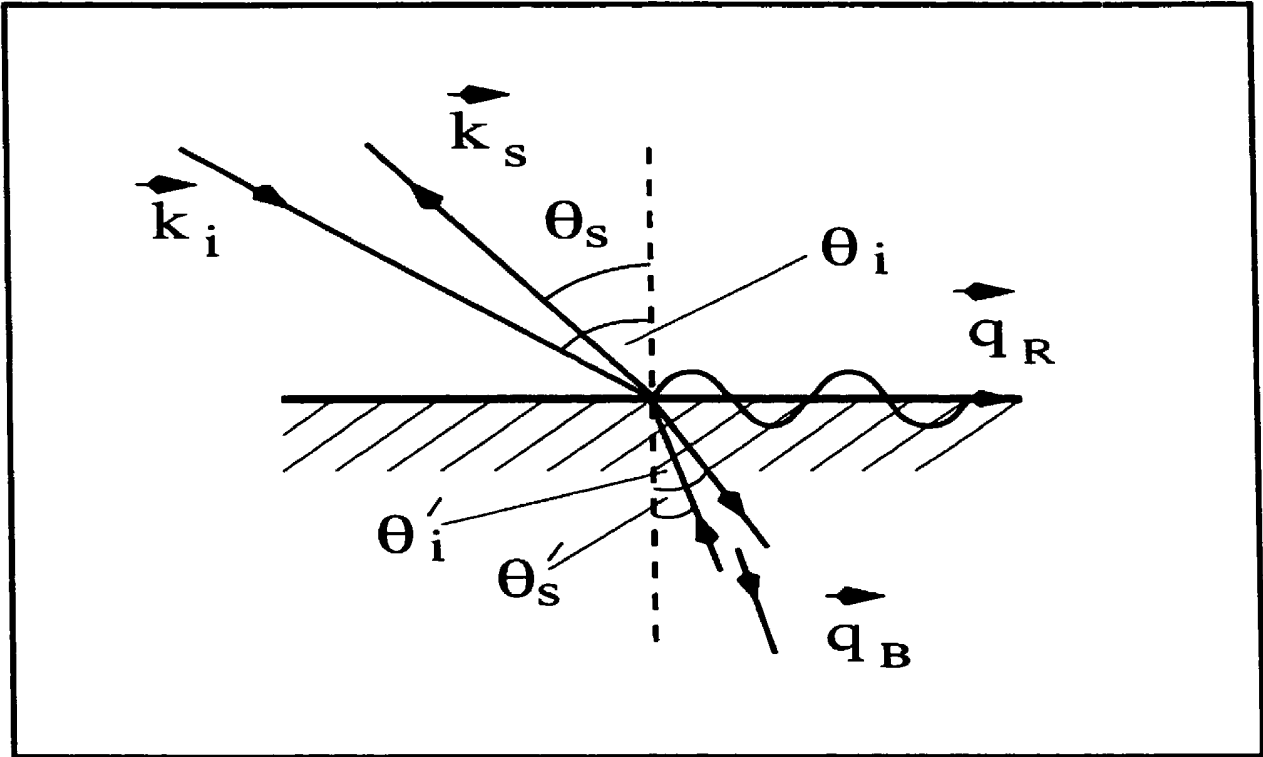
Figure 2.2: Brillouin scattering geometry

where k_B is Boltzmann's constant and T is the absolute temperature [67]. From an experimental point of view, usually only the Stokes component is chosen for study due to its greater intensity in the scattered light spectrum.

2.1.3 Brillouin Scattering

As previously mentioned, Brillouin scattering is the scattering of light by thermally excited acoustic phonons. The theory of Brillouin scattering in solids has been discussed by several authors. One of the most notable early works is that of Benedek and Fritsch [68]. In the present study, most $\pi - Si$ films have thicknesses which are much greater than the acoustic phonon wavelength and hence the theory of Brillouin scattering developed for semi-infinite opaque solids is applicable [69-74] .

In a semi-infinite solid, there are two distinct mechanisms by which acoustic phonons may scatter light [73, 75]. First there is the bulk elasto-optic mechanism in which the coupling of incident and scattered light occurs due to the acoustic modulation of the sample dielectric constant. The second is the surface ripple effect in which light is reflected from the dynamic acoustic deformation of the sample surface. The spectrum of scattered light, therefore, contains information about both bulk and surface acoustic phonons.

The optical transparency of the solid is the primary determinant of the relative importance of the two scattering mechanisms [75]. For a very transparent material, where the incident light illuminates a comparatively large volume of the sample, scattering via the elasto-optic mechanism dominates. In this case, scattering from a bulk acoustic phonon can occur if the phonon wavevector $\vec{q} = \vec{q}_B$ satisfies the momentum conservation requirement 2.2. It is this mechanism which produces the traditional Brillouin spectrum exhibiting peaks due to quasilongitudinal and quasitransverse acoustic phonons.

With reference to figure 2.2 and simple application of Snell's law, equation 2.2 may be written in terms of components parallel and perpendicular to the surface as,

$$q_B^{\parallel} = nk_i \sin\theta_i' + nk_s \sin\theta_s' = k_i \sin\theta_i + k_s \sin\theta_s \tag{2.7}$$

$$q_B^{\perp} = nk_i \cos\theta_i' + nk_s \cos\theta_s', \tag{2.8}$$

where n is the index of refraction. Using equations 2.7 and 2.8 along with the fact that the dispersion relation is linear for the acoustic phonons accessible by Brillouin scattering, it is possible to obtain an expression for the frequency shift of the incident light (which is equal to the acoustic phonon frequency),

$$\omega_B = q_B V_B = 2nk_i V_B \sin\left(\frac{\gamma}{2}\right), \tag{2.9}$$

where the standard approximation $k_i \simeq k_s$ has been used. The quantity V_B is the bulk acoustic phonon velocity and $\gamma = \pi + \theta_s' - \theta_i'$ is the scattering angle (i.e., the angle between

the wavevectors of the incident and scattered light). Equation 2.9 is the well-known Brillouin equation for scattering from bulk acoustic phonons. It permits calculation of bulk phonon velocities from the Brillouin spectrum if n, γ and $k_i = 2\pi/\lambda_i$, where λ_i is the wavelength of the incident light, are known.

As the sample transparency decreases, the wavevector conservation in the direction perpendicular to the surface (condition 2.8) breaks down. This is because the incident light is only able to penetrate a short distance below the surface and thus couples to phonons with a range of possible wavevectors in accordance with the uncertainty principle. This results in a broadening of the bulk Brillouin spectrum and is discussed in greater detail elsewhere [76-79] . In addition, the increasing opacity results in a smaller scattering volume which leads to a reduction of the cross section for the bulk elasto-optic mechanism. In this situation, scattering via the surface ripple mechanism becomes important and may even dominate [75].

In the case of scattering from surface modes, the wavevector conservation condition 2.8 fails again, this time because the phonon amplitude becomes negligible at a distance ~ 1 wavelength below the sample surface. Condition 2.7 remains valid and now takes the form

$$q_R = k_i \sin \theta_i + k_s \sin \theta_s = k_i(\sin \theta_i + \sin \theta_s), \tag{2.10}$$

where q_R is the magnitude of the Rayleigh surface phonon wavevector. Hence, a sharp peak should be observed in the scattered light at a frequency shift given by

$$\omega_R = q_R V_R = k_i V_R(\sin \theta_i + \sin \theta_s), \tag{2.11}$$

where V_R is the surface phonon velocity.

In a backscattering geometry, such as that used here, equations 2.9 and 2.11 take on

the particularly simple forms

$$\omega_B = 2nk_iV_B = \frac{4\pi nV_B}{\lambda_i} \tag{2.12}$$

and

$$\omega_R = 2k_iV_R\sin\theta_i = \frac{4\pi V_R\sin\theta_i}{\lambda_i}. \tag{2.13}$$

since $\gamma = 180°$ and $\theta_i = \theta_s$.

2.2 Elasticity Theory

2.2.1 Surface Acoustic Waves and Elastic Constants

The surface and bulk acoustic phonons probed in Brillouin scattering have wavelengths much greater than the primitive cell dimensions and therefore behave like sound waves in a continuous medium [61]. In such a case, the crystal may be treated as an elastic continuum and the equations of motion of these waves become [80],

$$\rho\frac{\partial^2 u_i}{\partial t^2} = C_{ijkl}\frac{\partial^2 u_l}{\partial x_j \partial x_k}, \tag{2.14}$$

where ρ is the density, $\vec{u}$ is the displacement vector, and $\vec{r} = x_i\hat{e}_i$ is the position vector. The C_{ijkl} form a tensor of rank four known as the elastic constants tensor which, in the case of cubic crystals (such as Si), takes the form

$$\begin{pmatrix} C_{11} & C_{12} & C_{12} & 0 & 0 & 0 \\ C_{12} & C_{11} & C_{12} & 0 & 0 & 0 \\ C_{12} & C_{12} & C_{11} & 0 & 0 & 0 \\ 0 & 0 & 0 & C_{44} & 0 & 0 \\ 0 & 0 & 0 & 0 & C_{44} & 0 \\ 0 & 0 & 0 & 0 & 0 & C_{44} \end{pmatrix}, \tag{2.15}$$

where the standard notation of Voigt has been used to reduce the number of indices from four to two. As is evident, there are three independent elastic constants which are conventionally denoted C_{11}, C_{12}, C_{44}.

Before discussing the connection between surface acoustic waves and elastic constants, it is first necessary to define the coordinate system to be used. The semi-infinite solid is assumed to occupy the region $x_3 \leq 0$, with the free surface in the (x_1, x_2) plane. The positive x_3 direction is the outward normal to the free surface and the x_1 axis is chosen to lie along some convenient direction in the (x_1, x_2) plane. The surface plane is assumed to be stress-free, which means

$$C_{3jkl}\frac{\partial u_k}{\partial x_l} = 0 \quad \text{at} \quad x_3 = 0 \quad \text{for} \quad j = 1, 2, 3. \tag{2.16}$$

In contrast to the usual bulk wave problem, the solutions (to equation 2.14) of interest here are surface waves which propagate on the free surface with velocity V_R and whose displacement amplitudes decay rapidly with depth below the surface [81]. In other words, the solutions are assumed to be linear combinations of terms of the form

$$u_j = a_j e^{iq_R b_3 x_3} e^{iq_R(b_1 x_1 + b_2 x_2 - V_R t)}, \tag{2.17}$$

which satisfy the wave equation 2.14 and the boundary conditions 2.16 simultaneously [82]. In this expression, the b_n are the direction cosines of the surface acoustic wavevector. It should be noted that the imaginary part of b_3 in each of the terms of the solution must be negative so that the amplitudes of all the displacement components vanish as $x_3 \rightarrow -\infty$.

Substituting equation 2.17 into 2.14 and performing the necessary differentiations yields the set of equations

$$[\Gamma_{il} - \rho V_R^2 \delta_{il}] a_l = 0, \tag{2.18}$$

where $\Gamma_{il} = C_{ijkl} b_j b_k$. This is the same set of equations that results for the case of bulk acoustic waves in an infinite solid, but here b_3 is not initially known. For nontrivial

23

solutions it is necessary that

$$|\Gamma_{il} - \rho V_R^2 \delta_{il}| = 0, \tag{2.19}$$

where for cubic crystals,

$$\Gamma_{il} = \begin{cases} (C_{11} - C_{44})b_i^2 + b^2 C_{44} & i = l \\ (C_{12} + C_{44})b_i b_l & i \neq l. \end{cases} \tag{2.20}$$

Equation 2.19 is a sextic equation in b_3 with real coefficients for a given value of V_R [81, 82]. In general, there are three roots $b^{(n)}$ lying in the lower half of the complex plane that give solutions which satisfy the wave equation and vanish with depth below the sample surface. The assumed solution then becomes

$$u_j = \sum_{n=1}^{3} C_n a_j^{(n)} e^{iq_R(b_1 x_1 + b_2 x_2 + b_3^{(n)} x_3 - V_R t)}. \tag{2.21}$$

where the $a_j^{(n)}$ are the components of the eigenvector of equation 2.18 corresponding to the root $b_3^{(n)}$.

Substituting the assumed solution 2.21 into the boundary conditions 2.16 yields the set of three homogeneous equations,

$$\sum_{n=1}^{3} d_{jn} C_n = 0, \quad j = 1, 2, 3. \tag{2.22}$$

Here $d_{jn} = C_{3jkl} a_k^{(n)} b_l^{(n)}$. For nontrivial solution it is required that

$$|d_{mn}| = 0. \tag{2.23}$$

This is called the boundary-value determinant and is, in general, complex. For an arbitrary choice of velocity it is not possible to choose a set of weighting coefficients to satisfy the boundary conditions. There is, however, one particular value of V_R for which the boundary conditions will be satisfied and this is the velocity of the surface wave.

It is clear from the above theory that the surface acoustic wave velocity V_R depends on the density of the solid and the elastic constants. This fact, in conjunction with Brillouin

24

scattering data, may be exploited to permit determination of previously unknown sets of elastic constants.

2.2.2 Derived Quantities

Once the complete set of elastic constants is known for a particular material of cubic symmetry (e.g., Si), several other related quantities may be determined. One of the most important in this study is the anisotropy factor η given by

$$\eta = \frac{2C_{44}}{C_{11} - C_{12}}. \tag{2.24}$$

For an elastically isotropic solid $\eta = 1$. A fairly typical value is that for $c - Si$, $\eta = 1.56$.

A second important parameter is the bulk modulus B which is the reciprocal of the volume compressibility. For cubic crystals,

$$B = \frac{C_{11} + 2C_{12}}{3}. \tag{2.25}$$

This expression also holds for isotropic solids [83].

Also of interest are directionally dependent quantities such as Young's modulus E which is given by

$$\frac{1}{E} = \frac{C_{11} + C_{12}}{(C_{11} + 2C_{12})(C_{11} - C_{12})} + \left[\frac{1}{C_{44}} - \frac{2}{C_{11} - C_{12}} \right] (l_x^2 l_y^2 + l_x^2 l_z^2 + l_y^2 l_z^2). \tag{2.26}$$

Here, the l_i are the direction cosines of a unit vector in the direction of interest.

The bulk acoustic wave velocities also vary with direction of propagation in the crystal. Expressions for the velocities in the most common high symmetry directions are given in Table 2.1.

2.3 Phonon Confinement Model

The first-order Raman spectrum of $\pi - Si$ may be modelled using a theory based on the spatial confinement of phonons in nanometer-size crystallites [39-42]. This theory has

25

Table 2.1: Expressions for bulk acoustic wave velocities in high symmetry directions in cubic crystals.

Direction	V_L^2	$V_{T_1}^2$	$V_{T_2}^2$
[100]	$\dfrac{C_{11}}{\rho}$	$\dfrac{C_{44}}{\rho}$	$\dfrac{C_{44}}{\rho}$
[110]	$\dfrac{C_{11} + C_{12} + 2C_{44}}{2\rho}$	$\dfrac{C_{44}}{\rho}$	$\dfrac{C_{11} - C_{12}}{2\rho}$
[111]	$\dfrac{C_{11} + 2C_{12} + 4C_{44}}{3\rho}$	$\dfrac{C_{11} - C_{12} + C_{44}}{3\rho}$	$\dfrac{C_{11} - C_{12} + C_{44}}{3\rho}$

been found to be useful in accounting for both the peak-position shift and the asymmetric broadening observed in the Raman spectra of numerous nanocrystalline semiconductors. The main ingredient of this model, which was originally developed for microcrystalline Si, is a relaxation of the conservation of crystal momentum in the creation and decay of phonons in microcrystals. Here, a brief outline of this theory for the case of three dimensional confinement in spherical crystallites is given with relevant equations.

The wavefunction of a phonon of wavevector $\vec{q_o}$ in an infinite crystal is a plane wave,

$$\Phi(\vec{q_o}, \vec{r}) = u(\vec{q_o}, \vec{r})e^{i\vec{q_o} \cdot \vec{r}}, \qquad (2.27)$$

where the function $u(\vec{q_o}, \vec{r})$ has the periodicity of the lattice. If this phonon is now restricted to a spherical nanocrystal with diameter L, its wavefunction is modified (it is no longer a plane wave) and may be written as

$$\Psi(\vec{q_o}, \vec{r}) = W(\vec{r}, L)\Phi(\vec{q_o}, \vec{r}) = \Psi'(\vec{q_o}, \vec{r})u(\vec{q_o}, \vec{r}), \qquad (2.28)$$

where $W(\vec{r}, L)$ is the phonon weighting function which describes the confinement. For

three dimensional phonon confinement, the weighting function takes the form of a Gaussian,

$$W(\vec{r}, L) = e^{-8\pi^2 r^2/L^2}. \tag{2.29}$$

This function was chosen because it takes into account the fact that a distribution of many nanocrystals is sampled. It also shows good agreement with experimental data.

To obtain an expression for the Raman spectrum. $\Psi'(\vec{q_o}, \vec{r})$ is expanded in a Fourier series

$$\Psi'(\vec{q_o}, \vec{r}) = \int C(\vec{q_o}, \vec{q}) e^{i\vec{q} \cdot \vec{r}} d^3 q. \tag{2.30}$$

with the corresponding Fourier coefficients given by,

$$C(\vec{q_o}, \vec{q}) = \frac{1}{(2\pi)^3} \int \Psi'(\vec{q_o}, \vec{r}) e^{-i\vec{q} \cdot \vec{r}} d^3 r. \tag{2.31}$$

If equation 2.29 is substituted into 2.30 and the integration carried out. the Fourier coefficients become,

$$C(0, q) \propto e^{-q^2 L^2/32\pi^2}. \tag{2.32}$$

In this expression, $\vec{q_o}$ has been set equal to zero, which is appropriate for one-phonon Raman scattering.

The first-order Raman spectrum is proportional to the integral of weighted phonon Lorentzian profiles. In the case of spherical crystallites,

$$I(\omega) \propto \int \frac{|C(0, \vec{q})|^2 d^3 q}{[\omega - \omega(q)]^2 + (\Gamma/2)^2} \quad \propto \quad \int \frac{q^2 e^{-q^2 L^2/16\pi^2} dq}{[\omega - \omega(q)]^2 + (\Gamma/2)^2}, \tag{2.33}$$

where Γ is the linewidth ($FWHM$) of the $c - Si$ Raman line (~ 5 cm^{-1} in the present work), $\omega(q)$ is the dispersion relation for optic phonons in $c - Si$ and the integration is performed over the entire Brillouin zone which is assumed to be spherical. The expression for the Raman spectrum demonstrates that the weighting function influences the Raman lineshape through the Fourier coefficients and therefore its form is very important.

27

A similar argument for two dimensional confinement (*i.e.*, cylindrical crystallites) leads to a similar integral for the first-order Raman spectrum. In this case, L is the diameter of a cylinder with infinite length and the other quantities are the same as in the three dimensional case.

Chapter 3

Experiment

3.1 Samples

The $\pi - Si$ samples used in these experiments were formed on the polished surfaces of (111)-oriented p^- or p^+ type single crystal Si wafers by standard electrochemical etching in HF-alcohol solutions. They are divided into three groups. The first set of $\pi - Si$ samples (Set I) (provided by Dr. V. Bondarenko, Belorussian State University, Minsk, Byelarus) was used for Raman scattering experiments only, while Sets II and III (provided by Dr. E. Nossarzewska-Orlowska, Institute of Electronic Materials Technology, Warsaw, Poland) were studied using Brillouin scattering. In nearly all cases, the porosity ξ (determined using a gravimetric method with 5% accuracy) and layer thicknesses h of the samples in each set were known prior to the light scattering studies.

As is evident from Table 3.1, Set I consists of five layers prepared on both p^- and p^+ type B doped substrates. Anodization was performed in a 40% HF-ethanol solution with current densities ranging from $J = 2.5$ mA·cm^{-2} to $J = 40$ mA·cm^{-2}. The resulting films had porosities of 35%, 65% and 80%. The film thicknesses were determined using infrared reflectance and ranged from 5 μm to 80 μm (the porous layer thickness for sample E is not known).

The samples comprising Set II were formed on two different types of starting wafers (see Table 3.2). Layers #1-#4 were etched on standard Czochralski-grown p^+ type substrates ($R \sim 0.01$ Ω·cm), while 10 μm-thick epitaxial layers of p^- type Si ($R = 10$ Ω·cm)

Table 3.1: Anodization conditions and related parameters for Set I.

Sample #	Substrate type	Resistivity ($\Omega \cdot$cm)	Current density (mA$\cdot$cm^{-2})	Layer thickness (μm)	Porosity (%)
A	p^-	10.0	20.0	5	80
B	p^-	10.0	40.0	20	80
D	p^+	0.03	15.0	80	80
C	p^+	0.03	5.0	10.5	65
E	p^+	0.005	2.5	—	35

deposited on p^+ type substrates were used for samples #5 to #7: the low resistivity substrate allowing good electrical contact during anodization. In the latter case, due to the thickness of the epitaxial layers, the porous films extended only into the p^- type material. All wafers were etched in an HF-isopropyl alcohol solution at a constant current density of 10 mA$\cdot$cm^{-2}. The HF concentration was varied to produce layers with a range of porosities. with higher porosity correlating with lower HF concentration as mentioned in Section 1.1.3. Individual layer thicknesses were measured using SEM. Pictures of several samples in this set are shown in Figure 3.1.

Set III consists of samples formed on p^+ type substrates ($R = 0.01\ \Omega \cdot$cm) with a relatively small range of porosities but a wide variation in layer thickness (see Table 3.3). Since the porous layer thickness is nearly linearly dependent on the anodization time, this

Table 3.2: Anodization conditions and related parameters for Set II.

Sample #	Substrate type	HF concentration (%)	Etching time (min)	Layer thickness (μm)	Porosity (%)
1	p^+	43	2	2.7	30
2	p^+	40	1.5	1.9	32
3	p^+	38	1.5	1.8	35
4	p^+	35	4	4.0	40
5	p^-/p^+	35	4	1.6	50
6	p^-/p^+	28	6	2.1	60
7	p^-/p^+	20	2	0.5	70
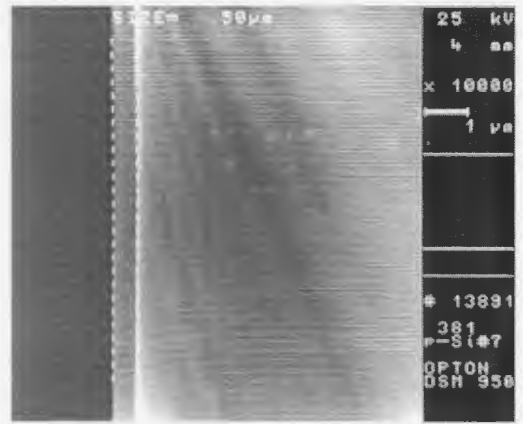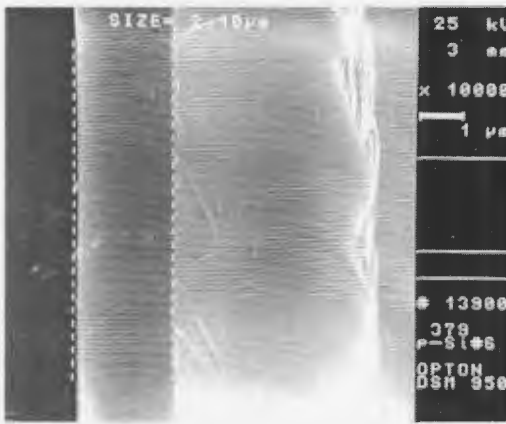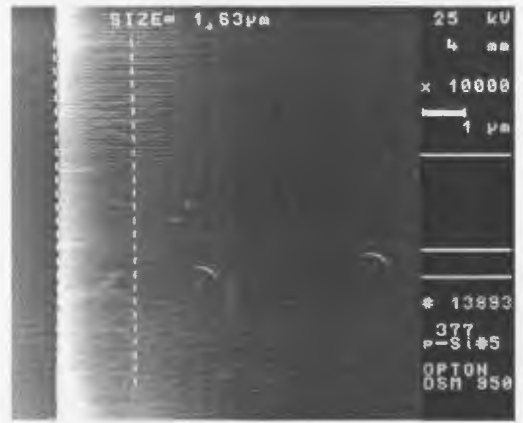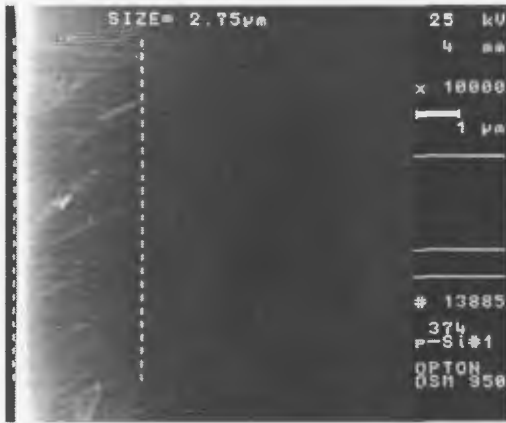
Figure 3.1: Electron micrographs of some samples of Set II (top left - #1, top right - #2, center left - #4, center right - #5, bottom left - #6, bottom right - #7). The porous layer is contained between the two vertical dashed lines on each micrograph.

Table 3.3: Anodization conditions and related parameters for Set III.

Sample #	Etch time (s)	Substrate type	ρ (Ω·cm)	J (mA·cm^{-2})	h (SEM) (μm)	h (IR) (μm)	ξ (%)
539	1800	p^+	0.01	10.0	39.26	40.2	32
540	900	p^+	0.01	10.0	20.85	21.7	31
541	450	p^+	0.01	10.0	11.40	11.4	28
542	192	p^+	0.01	10.0	5.50	5.5	25
543	96	p^+	0.01	10.0	2.43	2.7	28
557	63	p^+	0.01	10.0	1.65	2	29

variation was achieved by holding the HF concentration and current density constant (at values of 43% and 10 mA·cm^{-2}, respectively) and varying the etching time. The layer thicknesses were determined using SEM and independent confirmation was obtained by infrared reflectance for some of the samples. The variation in thickness for a given layer was found to be $\pm 5\%$.

3.2 Optical Systems

3.2.1 Raman Scattering

The Raman experiments (and also some PL experiments) were carried out in air at room temperature with the optical system shown in Figure 3.2. They were performed in collaboration with Dr. N.H. Rich. Incident light was provided by an Ar$^+$ laser operating at either 488.0 nm or 514.5 nm with a beam power of $<$ 40 mW. The laser beam was polarized perpendicular to the plane of Figure 3.2 (i.e., parallel to the grating rulings of the spectrometer). Lens L_1 was used to slightly focus the light onto the $\pi - Si$ samples such that the typical spot diameter was $\sim$ 1 mm. The low beam power and slight focusing resulted in a small power density which minimized sample heating. The backscattered light was collected by a Cassegrain light collector (Applied Photophysics Inc.) which also served to focus the scattered light onto the entrance slit (S_1) of the spectrometer.
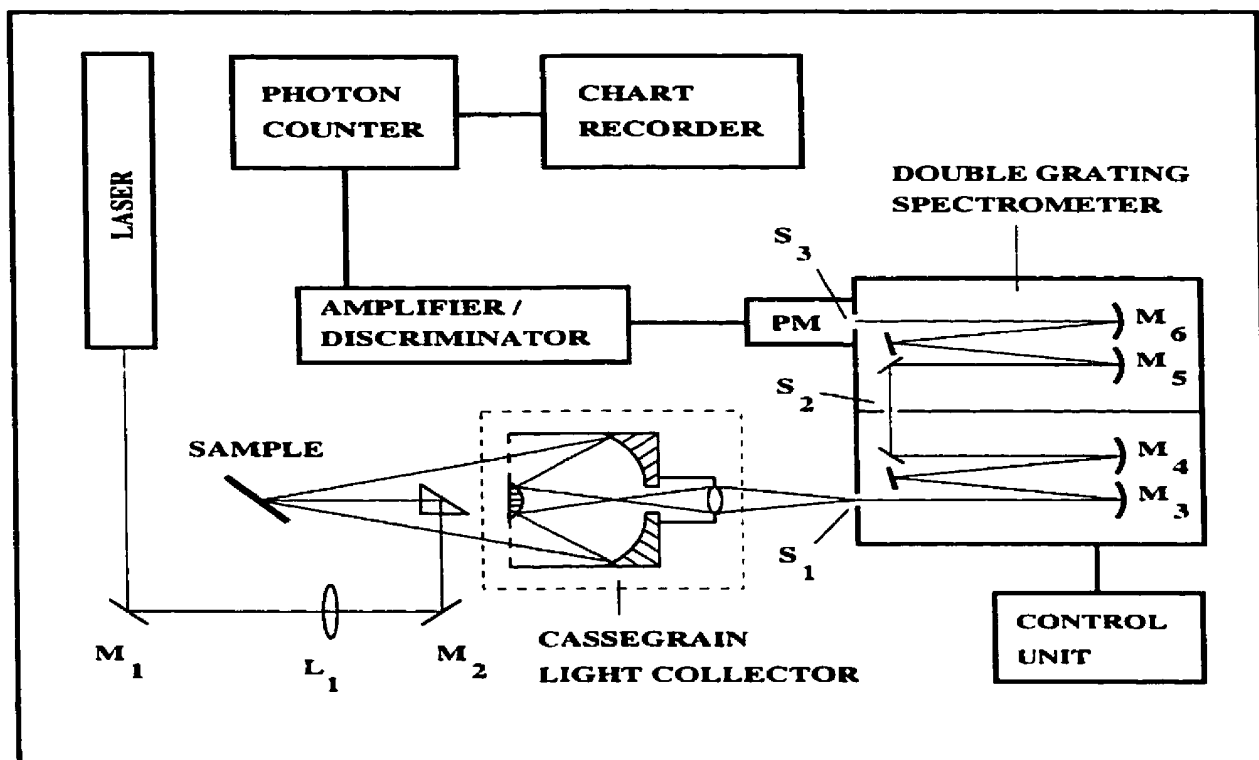
Figure 3.2: Experimental setup for Raman scattering from $\pi - Si$. The M_x are mirrors and the S_x are slits.

The Raman spectrometer consists of a double grating monochromator (Spex model 1401) with a focal length of 0.85 m and an aperture of $f/7.8$. It utilizes first order diffraction from holographic gratings (1800 grooves·mm^{-1}, dimensions 102 mm × 102 mm), which results in a theoretical resolving power of $\sim 10^5$. For optimum resolution, it was important to ensure that the light which exited slit S_1 completely filled the spectrometer's first collimating mirror (M_3) (and therefore was incident upon the full width of the grating). The light dispersed by the first grating was then focused by mirror M_4 onto a plane mirror. This mirror reflected the light through intermediate slit S_2 and into the second compartment of the monochromator where it was again rendered parallel by mirror M_5. The light was dispersed by the second grating and focused by mirror M_6 onto exit slit S_3. In the present experiments, all three spectrometer slits (S_1, S_2 and S_3)

33

were opened to 300 μm corresponding to a spectral bandpass of approximately 4 cm^{-1} for both 488.0 nm and 514.5 nm excitation. The spectral region of interest was scanned at speeds of $\sim$ 0.01 cm$^{-1}\cdot$s^{-1}.

The light leaving the exit slit (S_3) of the monochromator was detected by a cooled photomultiplier tube (PM) (RCA 31034). The tube's output was then sent to a counter (typical sampling time $\sim$ 10^7 μs) via an amplifier/discriminator and displayed on a standard strip chart recorder. Absolute wavenumber calibration was performed using various Ar$^+$ plasma lines which appeared in the spectra.

3.2.2 Brillouin Scattering

The experimental setup used for most of the Brillouin studies is shown in Figure 3.3. A single mode Ar$^+$ laser (Coherent Innova 90-5) operating at a wavelength of 514.5 nm and a beam power of $\leq$ 100 mW served as the incident light source. A half-wave plate (HWP) was used to rotate the plane of polarization such that the light was p-polarized (*i.e.*. polarized in the plane of incidence) just before hitting the sample. This minimized losses due to reflection. Lens L_1 ($f = 1.0$ m) served to slightly focus the beam so that the diameter was reduced when incident upon the acousto-optic modulator (AOM). This resulted in greater diffraction efficiency.

The primary purpose of the acousto-optic modulator was to prevent saturation of the photomultiplier tube (PM) by the intense scattered light which was present when scanning over the elastic peak in the $\pi - Si$ spectrum. To achieve this the modulator was operated in first-order mode. This configuration resulted in only a small percentage of the full power of the zeroth-order beam being diffracted into first-order when scanning over this region of the spectrum. It also served to reduce sample heating since, during this part of the scan, only a fraction of the full power of the incident beam was incident on the sample.
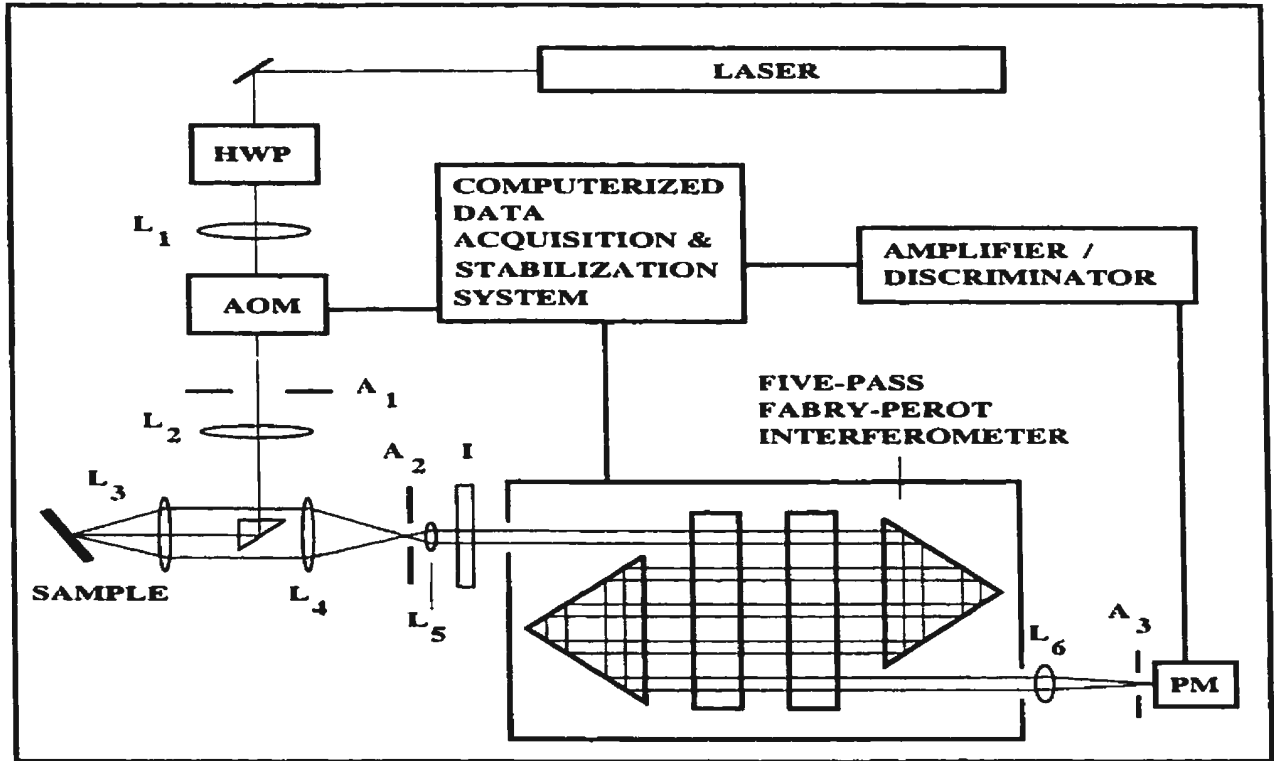
Figure 3.3: Experimental setup for Brillouin scattering from $\pi - Si$. The A_x are apertures and the L_x are lenses.

Light exiting the modulator was recollimated by lens L_2 and directed to the focusing/collecting lens L_3 (Nikon. $f/1.8$, $f = 5.0$ cm) using a small prism (3 mm $\times$ 3 mm). Lens L_3 focused the incident light on the sample at angles of incidence in the range $25° \leq \theta_i \leq 75°$. The diameter d of the focused spot on the sample surface produced by this lens was estimated using the far-field (focal length of lens $\gg$ incident spot size) relation for focusing a Gaussian beam with a lens [84],

$$d = \frac{4\lambda_i f}{\pi D}.$$ (3.1)

In this case, $f = 5.0$ cm and $\lambda_i = 514.5$ nm. To obtain a numerical value for D, the intensity profile of the laser beam was obtained. A 25 μm pinhole was positioned perpendicular to the beam between the prism and lens L_3. This pinhole was then stepped

35
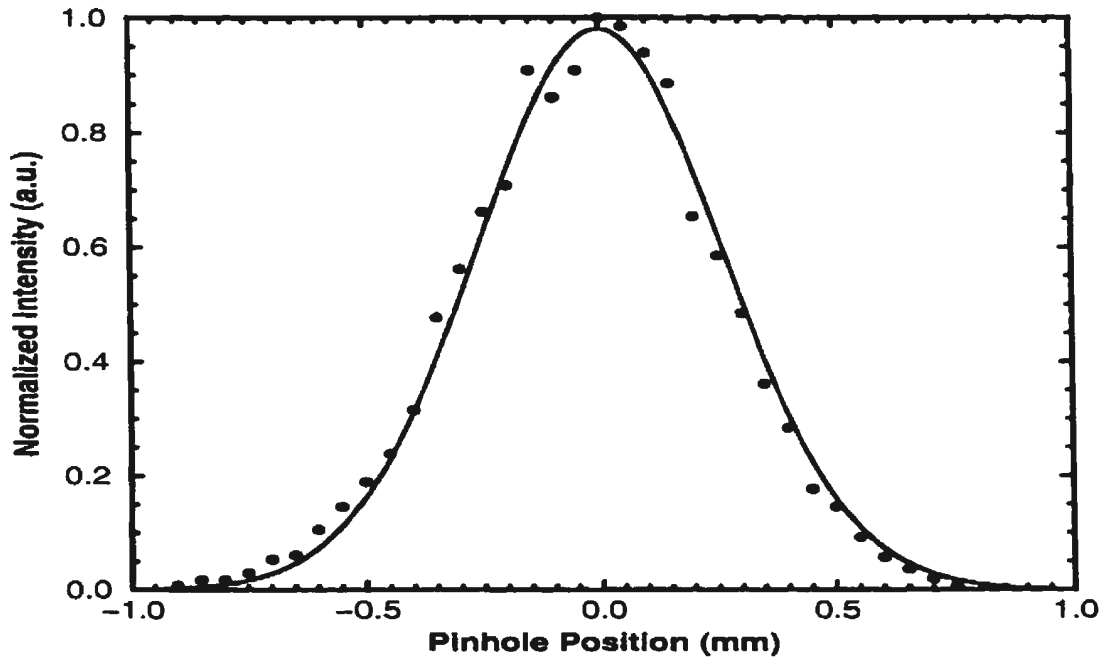
Figure 3.4: Horizontal laser beam intensity profile. The filled circles are the experimental data points and the solid line is the best-fit Gaussian function $I(x) = 0.98 \exp(-7.2 \times 10^{-1} x^2)$.

across the beam in 50 μm intervals with the power of that part of the beam passing through the pinhole measured at each interval. A Gaussian function was fitted to the experimental points as shown in Figure 3.4. At the $1/e$ points the beam radius was found to be 3.7×10^2 μm corresponding to a diameter of $D = 7.4 \times 10^2$ μm. Substituting these values into equation 3.1 yields a spot diameter of approximately 50 μm, corresponding to a power density of ≤ 50 W·mm^{-2} at the sample surface.

The backscattered light was collected by the same lens (i.e., L_3). The f-number of this lens was set to 2.8 to minimize spherical aberration and also to minimize broadening of the Brillouin lines due to finite aperture effects. The collimated scattered light leaving L_3 was focused by lens L_4 ($f = 20.0$ cm) onto a 200 μm pinhole (A_2). Lens L_5 ($f = 5.0$ cm)

recollimated the scattered light. The degree of collimation was checked by measuring the spot diameter at a position close to the lens and also a few meters away. If the diameter remained constant, then the collimation was considered acceptable. Otherwise, the lens position was adjusted until no change in diameter was observed. A narrow bandpass filter (I), with a width of ± 10 nm centered on the laser wavelength, was placed immediately in front of the Fabry-Perot to block all light other than that in the range of the Brillouin spectrum.

The light was analyzed by a five-pass piezoelectrically scanned Fabry-Perot interferometer (Burleigh RC-110). The plates were flat to $\lambda/200$ and had a reflectivity of 88% giving a theoretical five-pass finesse $F \simeq 62$ and a contrast $C \simeq 7 \times 10^{11}$. The experimental finesse values were somewhat lower ($F = 30 - 40$). An estimate of the contrast was not obtained, but is usually about an order of magnitude lower than the theoretical value [85]. The free spectral range (FSR) of the interferometer was changed as required but was typically around 20 GHz. An estimate of each FSR was obtained by measuring the interferometer plate separation, but accurate determination required that a spectrum of fused quartz be collected. The FSR could then be determined using the well-known frequency shifts of the longitudinal and transverse acoustic phonons in quartz.

After exiting the interferometer, the light was focused onto pinhole A_3 (diameter $= 1.0$ mm, 800 μm or 600 μm) by lens L_6 ($f = 1.0$ m). The light was detected by a water-cooled photomultiplier (ITT FW130) operated at a voltage of 1700 V. The dark count rate was < 1 s^{-1}. The output from the photomultiplier was sent to a computerized data acquisition and stabilization system (CDAS) via an amplifier/discriminator. In addition to its use as a multichannel analyzer, the CDAS provided the ramp voltage necessary to scan the interferometer. It also continuously compensated for drift of the Fabry-Perot cavity and optimized interferometer finesse.

As alluded to earlier, some of the Brillouin scattering experiments (especially those

37

on samples with porosities $\geq$ 50%) were carried out using a different optical system than that outlined above. The primary difference between the two systems is that the second employed a Sandercock-type six-pass (3+3) tandem Fabry-Perot interferometer (see Figure 3.5) to analyze the scattered light. The plate reflectivity of the tandem interferometer was 91% and the experimental finesse was again 30 -- 40. Despite the similarity of these values to those for the five-pass interferometer, the tandem instrument did offer some inherent advantages. These included greater contrast as well as elimination of overlap of neighbouring interference orders which allows the FSR to be greatly increased (a factor of 10 to 20 times larger than that of a single interferometer).

A second important difference between the two systems was the use of a slit (width = 1 mm) in the scattered light in the tandem setup. This substantially reduced the broadening due to the finite aperture of the collecting lens (f-number = 1.4) since it limited the range of scattering wavevectors sampled. An attempt at using a similar slit arrangement in the five-pass setup failed because it caused a drastic reduction in the Brillouin signal and thus unreasonably long collection times were necessary to obtain acceptable spectra.

3.3 Adsorbed Water Removal

To examine the effect of adsorbed water on the velocity of surface acoustic waves on $\pi - Si$, it was first necessary to develop a method by which any adsorbed water could be removed. Brillouin spectra could then be recorded both before and after the removal of any adsorbed water on the sample surface.

The procedure adopted here was straightforward and made use of the apparatus shown in Figure 3.6. The sample was placed in an air-tight glass cell and heated with a resistance wire heater to a temperature of approximately 150 °C while the cell was

38
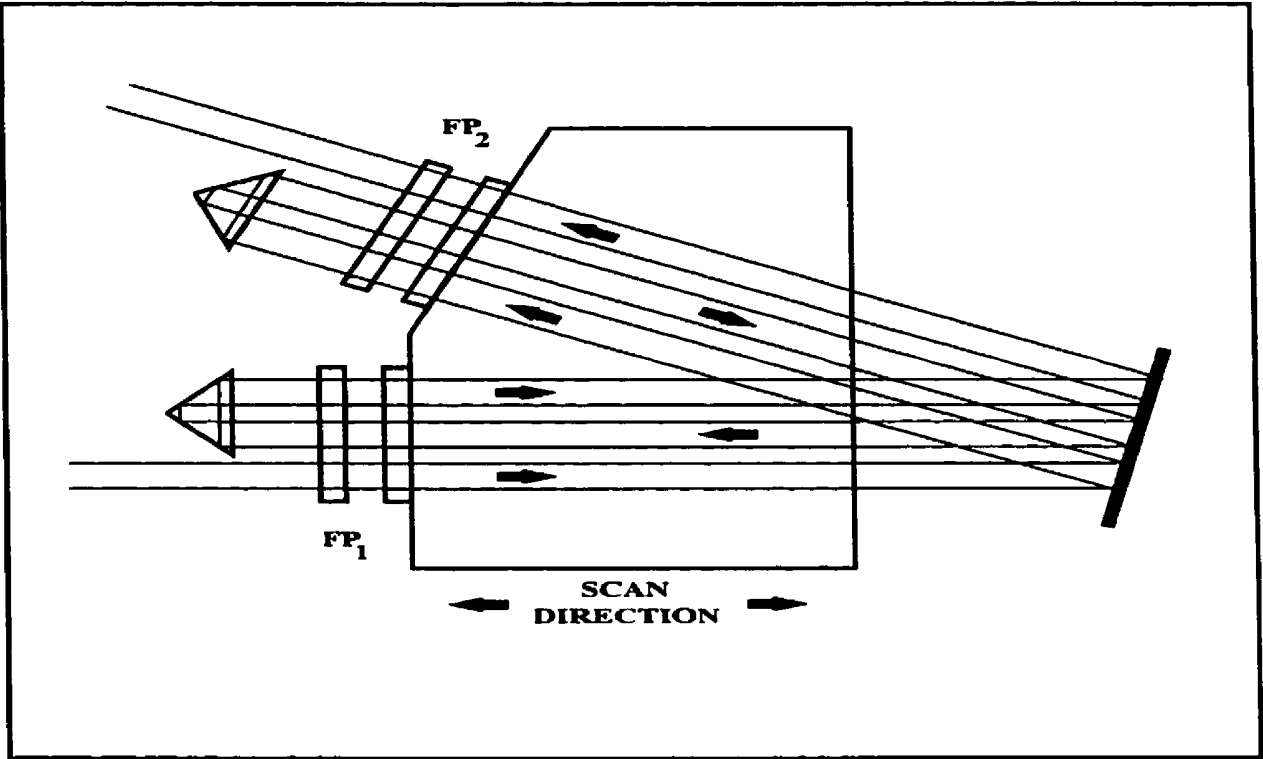
Figure 3.5: Sandercock-type (3+3)-pass tandem Fabry-Perot interferometer.

simultaneously being pumped on with a rotary/diffusion vacuum pump system. This part of the process lasted a minimum of 24 h and pressures around 10^{-6} mbar were maintained over this time interval. Following this, the sample was cooled back to room temperature ($\sim$ 18 °C) and the vacuum was broken using nitrogen gas. The sample was then removed from the glass cell, affixed to the sample holder and placed in a continuous stream of nitrogen gas for the entire time that the Brillouin spectrum was collected. The maximum exposure time to air was approximately 15 min. The use of nitrogen gas and the limited exposure time to air helped to prevent the readsorption of water onto the $\pi - Si$ surface.
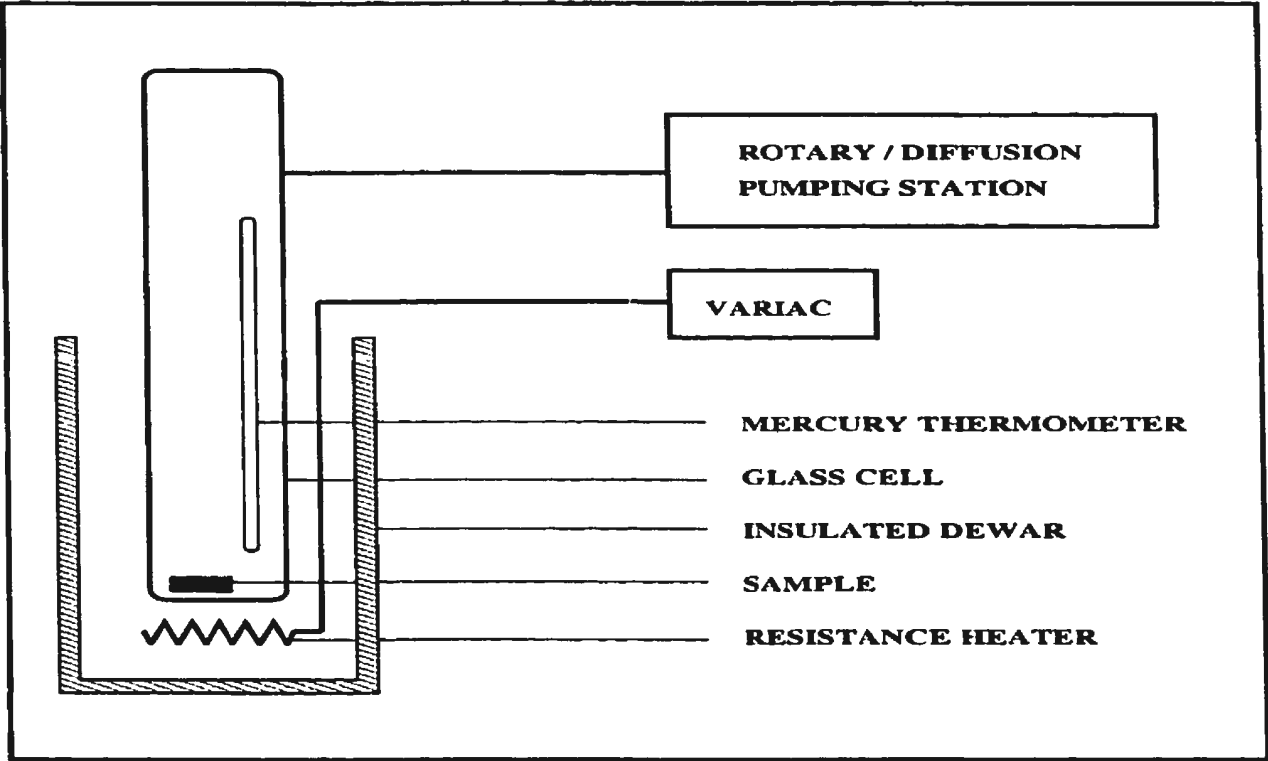
Figure 3.6: Apparatus for removal of water adsorbed on $\pi - Si$.

3.4 Native Oxide Film Removal

It is well-known that a thin native oxide film forms on the surface of $\pi - Si$ when it is exposed to air, but the effect of such films on the $\pi - Si$ surface acoustic phonon velocity has not been studied. To investigate this, Brillouin scattering experiments were performed on films with and without the oxide layer.

The procedure for the removal of the oxide films made use of the fact that HF vigorously attacks SiO_2 but etches Si at a rate of only nanometers per hour. Each sample was first divided into two pieces. One piece of each sample was dipped in a 10% solution of HF (distilled water and concentrated HF (49%)) for approximately 10 s to remove any native oxides, while the second piece was left untreated. Following the dip, the samples were dried in a stream of nitrogen gas. The HF-treated pieces were stored

40

in vacuum prior to collection of Brillouin spectra. Spectra were also collected from the untreated pieces during this time. To keep airborne molecules off the surface of these pieces, a stream of nitrogen gas flowed over the $\pi - Si$ layers for the entire spectrum accumulation time (typically a few hours).

Chapter 4

Results

4.1 Brillouin Scattering

4.1.1 General Features of the Brillouin Spectra of $\pi - Si$

Several hundred Brillouin spectra were collected from $\pi - Si$ samples with a wide range of porosities ($\xi = 28\% - 60\%$). The primary focus here is on the low porosity samples ($\xi = 28\% - 40\%$) since they could be satisfactorily studied with the in-house optical system which incorporated the five-pass Fabry-Perot interferometer. This is because their Brillouin spectra generally had only one pair of Brillouin peaks (due to the Rayleigh surface wave) in the frequency regime of interest. In contrast, the higher porosity ($\xi = 50\% - 60\%$) samples exhibited multiple and/or broadened Brillouin peaks and therefore required the use of the tandem interferometer system. Due to time constraints, however, only a limited number of spectra could be collected from these samples. It was noted that acceptable Brillouin spectra could be obtained much more quickly with the setup incorporating the tandem interferometer than with the five-pass interferometer. Typical collection times for tandem spectra were less than 1 h while the five-pass spectra required times of at least a few hours.

A typical Brillouin spectrum (collected with the tandem interferometer system set at an FSR = 30 GHz) of a low porosity (35%) sample (E of Set I) formed from a p^+ type $c-Si$ substrate is shown in Figure 4.1 along with a spectrum collected from the nonporous (crystalline) part of the same wafer. The features labelled R and E are due to the Rayleigh
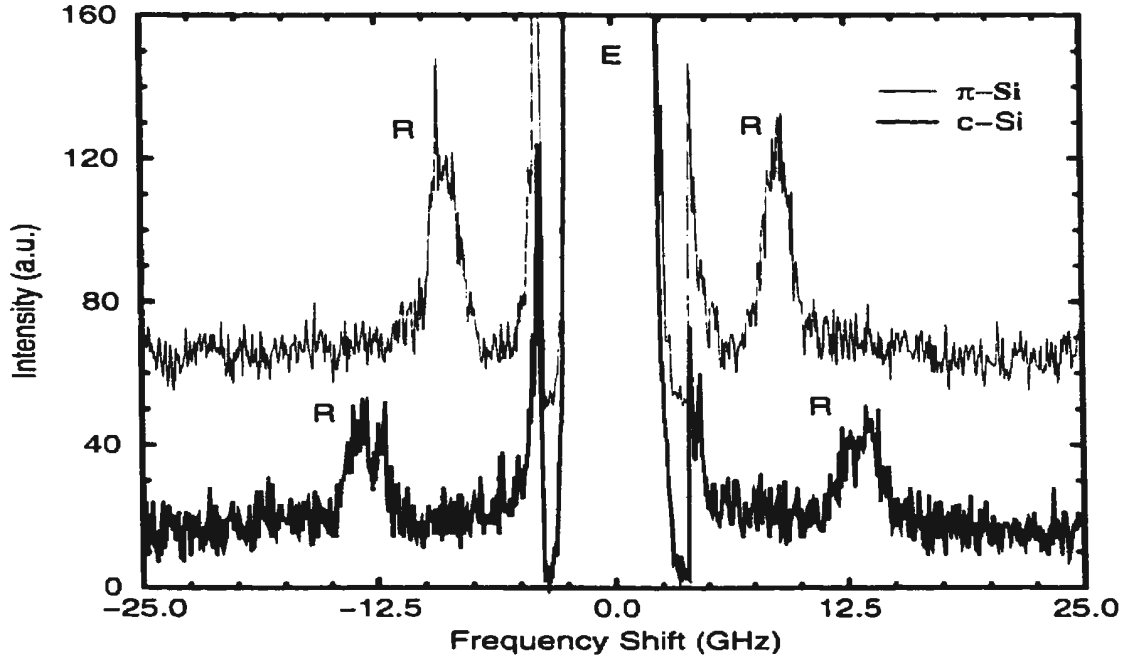
Figure 4.1: Brillouin spectra collected from the porous (upper trace) and nonporous (lower trace) regions of sample E of Set I. The collection time for the $\pi - Si$ spectrum was approximately 16 min while that for $c - Si$ was 20 min. Both spectra were collected using the tandem Fabry-Perot interferometer system with the angle of incidence set to 45°.

surface mode and elastic scattering, respectively. The $FWHM$ of the elastic peak is approximately 1.2 GHz, while the Rayleigh lines have widths which are about 0.5 GHz larger. It is clear that the frequency of the surface phonon propagating in the porous layer is significantly lower than that of the corresponding phonon travelling in the nonporous part of the sample. This was found to be true in general for low porosity $\pi - Si$ and, for the particular case shown in the Figure 4.1, the frequency shift of the $\pi - Si$ Rayleigh phonon peak is 9.08 ± 0.08 GHz while that for the nonporous ($c - Si$) region is 13.05 ± 0.08 GHz. The errors associated with the frequency shifts are due to the estimated uncertainty in determination of the Brillouin peak positions from the spectra ($\sim \pm 1$ channel on the

43
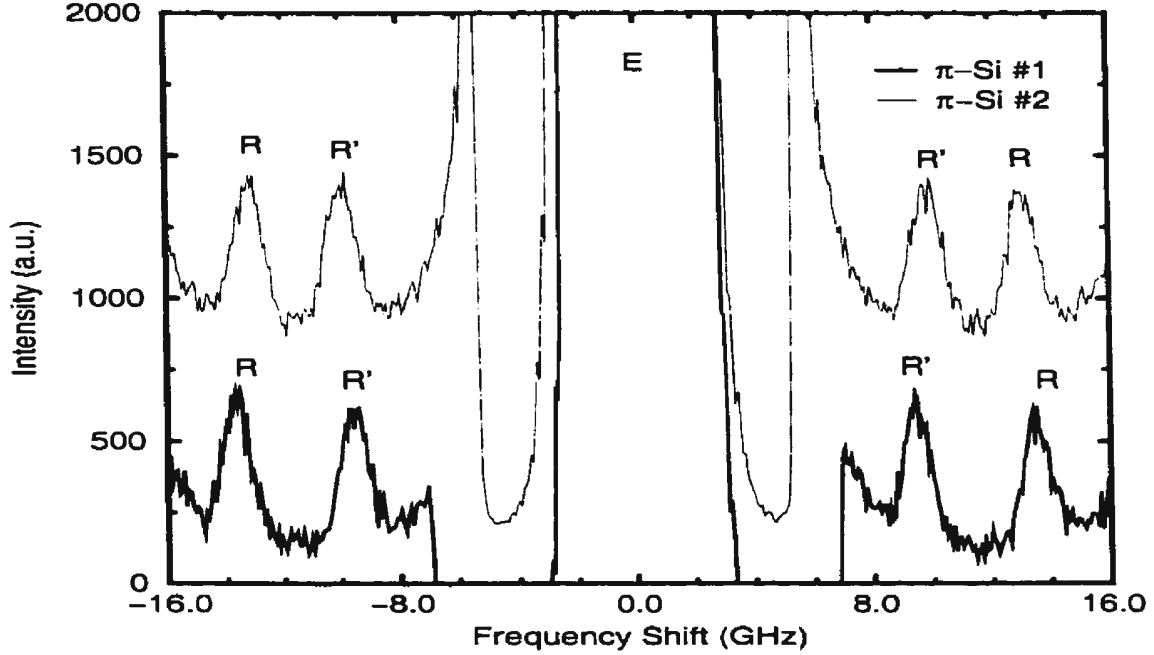
Figure 4.2: Brillouin spectra collected from the porous regions of samples #1 and #2 of Set II. Both spectra were collected using the five-pass Fabry-Perot interferometer system with the angle of incidence set to 70°. The phonon propagation direction is $[2\bar{1}\bar{1}]$. The $FWHM$ of the elastic peak is ~ 1.0 GHz. The $FWHM$ of the SAW peak is ~ 1.2 GHz.

CDAS). Using Equation 2.13, the SAW velocity for phonons propagating in the porous region of the wafer was found to be $V_R^{\pi-Si} = 3303$ m·s^{-1}. This is approximately 30% lower than that for the nonporous region of the sample ($V_R^{c-Si} = 4748$ m·s^{-1}).

It is also evident in Figure 4.1 that the intensities of the $\pi - Si$ Rayleigh peaks are greater than those for $c - Si$. This was found to be true in general and may be due to a resonance effect similar to that seen in Raman scattering. The intensity may also be greater because a larger scattering volume is accessible to the incident light due to the reduced effective refractive index of $\pi - Si$ compared to $c - Si$.

Brillouin spectra collected from $\pi - Si$ samples #1 (30% porosity) and #2 (32%
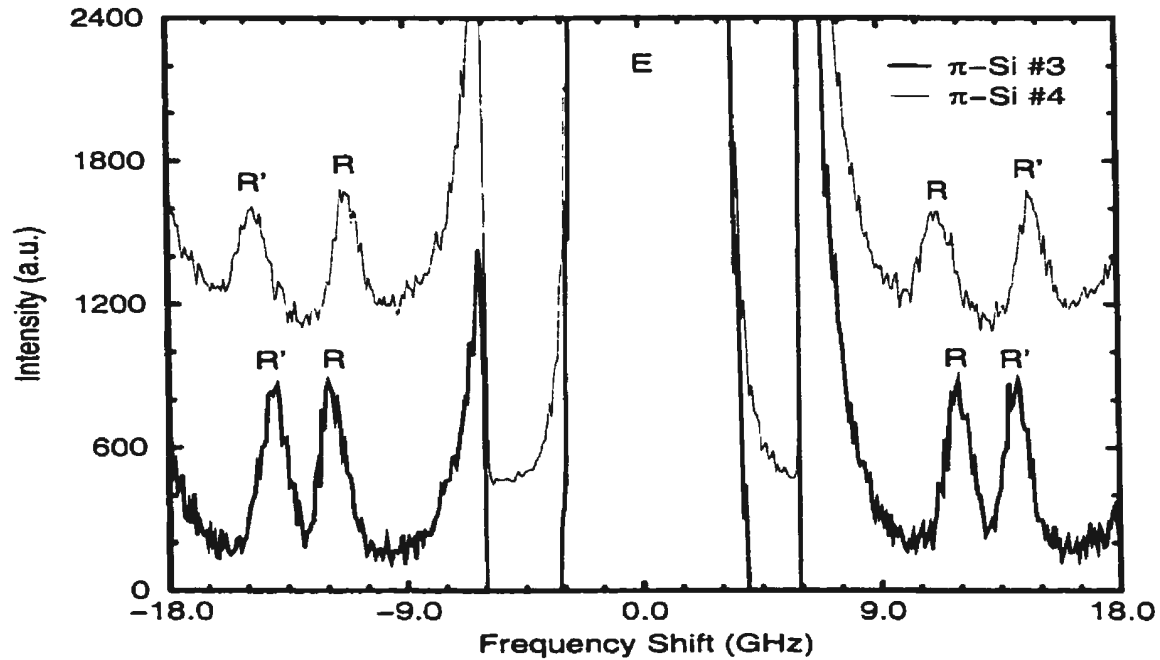
Figure 4.3: Brillouin spectra collected from the porous regions of samples #3 and #4 of Set II. Both spectra were collected using the five-pass Fabry-Perot interferometer system with the angle of incidence set to 60°. The phonon propagation direction is [2$\bar{1}\bar{1}$].

porosity) of Set II with the optical system incorporating the five-pass interferometer system are shown in Figure 4.2. The angle of incidence is 70° and the phonon propagation direction is [2$\bar{1}\bar{1}$]. The presence of four Rayleigh peaks (as opposed to two peaks in Figure 4.1) is due to overlap of neighbouring orders of interference with the unprimed peaks belonging to the same order. Such overlap is characteristic of (non-tandem) Fabry-Perot interferometers. The frequency shifts for samples #1 and #2 are 13.62 ± 0.08 GHz and 13.18 ± 0.08 GHz, respectively and correspond to SAW velocities of 3729 m·s^{-1} and 3608 m·s^{-1}. Thus even for a porosity difference of 2%, a measurable difference in surface wave velocity can be observed.

Brillouin spectra collected from samples #3 and #4 of Set II are shown in Figure 4.3.
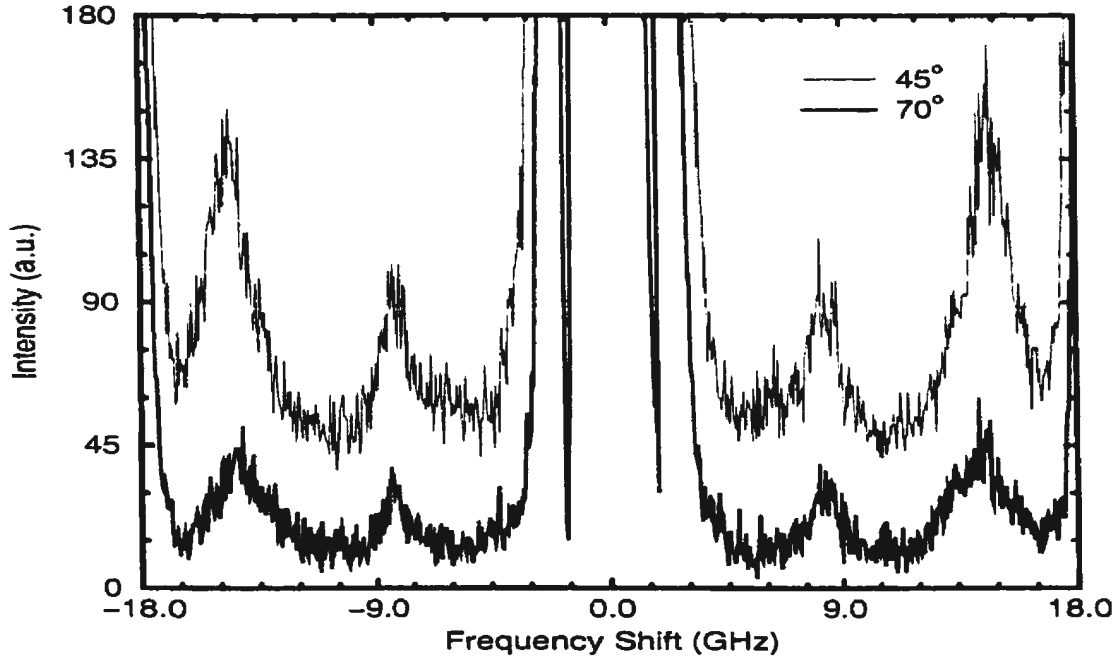
Figure 4.4: Brillouin spectra obtained from $\pi - Si$ #5 of Set II at scattering angles of 45° and 70°. The collection time for each spectrum was approximately 20 minutes. A slit was located in the scattered beam during accumulation of both spectra. These spectra were collected using the optical system which incorporated the tandem Fabry-Perot interferometer. The $FHWM$ of the elastic peak is $\sim$ 0.7 GHz.

These two samples have porosities of 35% and 40% respectively. As for samples #1 and #2, the Brillouin frequency shift for the lower porosity sample (11.97 ± 0.08 GHz) is greater than that for the sample of higher porosity (11.32 ± 0.08 GHz). Thus, the SAW velocity of sample #3 (3555 m·s^{-1}) is greater than that of sample #4 (3362 m·s^{-1}). In fact, for the first four samples of Set II (*i.e.*, #1-#4), there is a clear trend of decreasing SAW velocity with increasing porosity. The samples studied from Set III show analogous behaviour.

Figure 4.4 shows spectra collected from sample 5 of Set II using the tandem interferometer system. (It proved impossible to obtain acceptable Brillouin spectra of the

46

high porosity p^- samples using the five-pass Fabry-Perot interferometer). The phonon propagation direction is not known, but was the same for both angles of incidence (45° and 70°). In contrast to the samples #1-#4 of Set II, (which were all formed from p^+ type substrates), this sample was formed from p^- type $c-Si$ and has a porosity of 50%. As is evident in the figure, the spectra collected from this sample are very different from the spectra of the lower porosity layers formed from p^+ type substrates (at least in the spectral region studied here). The spectra exhibit two broad peaks located at low frequency shifts. Similar spectra were obtained from sample #6 of Set II ($\xi = 60\%$) as seen in Figure 4.5.

The frequency shifts and $FWHM$ of the Brillouin peaks shown in Figures 4.4 and 4.5 are tabulated in Table 4.1. With reference to the table, the subscripts 1 and 2 simply label the peaks with the lower and higher frequency shifts, respectively. It can be seen that peak 1 has a frequency shift which varies little over a large range in incident angle, while the shift of peak 2 changes quite noticeably. With the exception of peak 1 of sample #5, the $FWHM$ of the peaks in the table are very large compared to the width of the elastic peak (~ 1 GHz). It should be noted that a narrow slit was placed in the scattered beam while collecting the spectra and so the large linewidths are not due to collection lens broadening.

Qualitatively similar spectra have been obtained in another Brillouin scattering investigation of $\pi-Si$ ($\xi = 60\%$ and $\xi = 70\%$) formed from p^- type $c-Si$ substrates [51]. As in the present work, multiple Brillouin peaks with very large linewidths (2.5 GHz $\leq$ $FWHM \leq 4.2$ GHz for $\xi = 70\%$) were observed at low frequency shifts (2.5 GHz $\leq f^{\pi-Si}$ ≤ 12.5 GHz for $\xi = 70\%$). These peaks were ascribed to scattering from surface modes (Rayleigh and guided modes). In addition, no intrinsic bulk peaks were observed in the spectra. These spectral features (*i.e.*, large $FWHM$ and the lack of bulk peaks) were proposed [51] to be due to a crossover from translational invariance to self-similarity. A

47
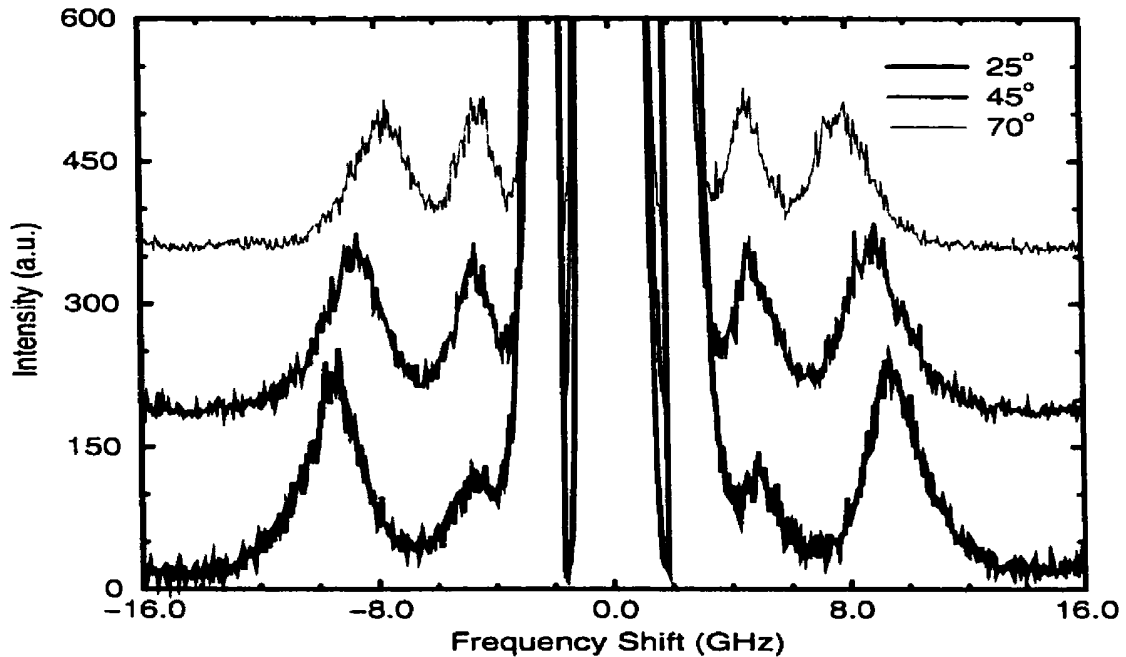
Figure 4.5: Brillouin spectra obtained from sample #6 of Set II at scattering angles of 25°, 45° and 70°. The collection time for each spectrum was approximately 20 minutes. A slit was located in the scattered beam during accumulation of all three spectra. These spectra were collected using the optical system which incorporated the tandem Fabry-Perot interferometer.

discussion of this in any detail is outside the scope of the present work and hence will not be pursued further.

4.1.2 Elastic Constants of Low Porosity $\pi - Si$ Layers

Complete sets of elastic constants for several low porosity $\pi - Si$ layers formed from p^+ type $c - Si$ substrates were determined from the directional dependence of the surface acoustic wave velocity on the (111) plane. Brillouin measurements were performed on samples #1-#4 of Set II and samples 543 and 557 of Set III. Data was also collected from the nonporous region of sample #2 of Set II for reference. The porous layers had

Table 4.1: Brillouin peak frequency shifts ($f^{\pi-Si}$) and corresponding $FWHM$ of samples #5 and #6 of Set II. The subscripts 1 and 2 refer to the peaks with the lower and higher frequency shifts in a given spectrum, respectively.

Sample	Incident Angle ($\pm0.5°$)	$f_1^{\pi-Si}$ (±0.08 GHz)	$f_2^{\pi-Si}$ (±0.08 GHz)	$FWHM_1^{\pi-Si}$ (±0.16 GHz)	$FWHM_1^{\pi-Si}$ (±0.16 GHz)
#5	45	8.27	14.72	1.02	1.52
	70	8.27	14.35	0.85	1.99
#6	25	4.77	9.47	1.64	1.97
	45	4.66	8.78	1.50	2.18
	70	4.59	7.78	1.42	2.00

porosities ranging from 28% to 40% and the layer thicknesses were $h \geq 1.6$ μm (see Tables 3.2 and 3.3), which are several times the acoustic wavelength.

To ensure that the porous layers could be treated as semi-infinite for calculational purposes, the SAW dispersion (dependence of SAW frequency on wavevector) was measured by varying the angle of incidence. This dispersion must be linear for a semi-infinite material. The resulting data are shown in Tables 4.2 and 4.3 along with corresponding data for $c - Si$ collected from the nonporous regions of samples #1 and #2. The phonon propagation direction was near [$2\bar{1}\bar{1}$]. In all cases, good fits to the data were obtained using linear functions (see Figures 4.6 and 4.7), indicating that the SAW velocities show little dispersion and hence are independent of wavevector.

The directional dependence of the SAW velocity on the (111) plane for the various samples is presented in Tables 4.4-4.10. For each sample, the Brillouin frequency shift was measured over a range of directions on the (111) plane separated by 5° increments. The angle of incidence was set to 60° to take advantage of the fact that a maximum in the ripple-scattering cross section occurs there [75]. This also prevented the recording of any artificial shifts due to the rapid changes in cross section with angle which occur for

Table 4.2: Rayleigh mode frequency shift as a function of acoustic wavevector for the nonporous parts of samples #1 and #2 of Set II and the porous parts of samples 543 and 557 of Set III.

Incident Angle ($\pm 0.5°$)	Wavevector ($\times 10^5$ cm^{-1})	Frequency Shift (± 0.08 GHz)			
		$c - Si$ #1	$c - Si$ #2	$\pi - Si$ 543	$\pi - Si$ 557
25.0	1.032 ± 0.003	8.19	7.75	—	
30.0	1.221 ± 0.003	9.84	9.90	6.77	—
35.0	1.401 ± 0.003	—	—	8.12	7.51
40.0	1.570 ± 0.003	—	12.43	—	8.52
45.0	1.727 ± 0.002	13.23	13.33	9.54	9.31
50.0	1.871 ± 0.002	14.37	14.37	10.56	10.22
55.0	2.001 ± 0.002	15.18	15.05	11.31	—
60.0	2.115 ± 0.002	16.32	16.13	11.84	11.23
65.0	2.214 ± 0.001	—	—	12.29	11.66
70.0	2.295 ± 0.001	—	—	12.89	12.15
75.0	2.359 ± 0.001	—	—	—	12.48

Table 4.3: Rayleigh mode frequency shift as a function of acoustic wavevector for the porous parts of samples #1-#4 of Set II.

Incident Angle ($\pm 0.5°$)	Wavevector ($\times 10^5$ cm^{-1})	Frequency Shift (± 0.08 GHz)			
		$\pi - Si$ #1	$\pi - Si$ #2	$\pi - Si$ #3	$\pi - Si$ #4
35.0	1.401 ± 0.003	8.69	8.49	8.48	—
40.0	1.570 ± 0.003	9.59	9.21	9.43	8.79
45.0	1.727 ± 0.002	10.60	10.05	10.11	9.49
50.0	1.871 ± 0.002	—	—	10.77	10.13
55.0	2.001 ± 0.002	—	—	11.51	10.77
60.0	2.115 ± 0.002	12.68	12.25	11.97	11.32
65.0	2.214 ± 0.001	13.19	12.82	12.44	11.75
70.0	2.295 ± 0.001	13.62	13.18	—	12.08
75.0	2.359 ± 0.001	14.01	13.51	—	12.55
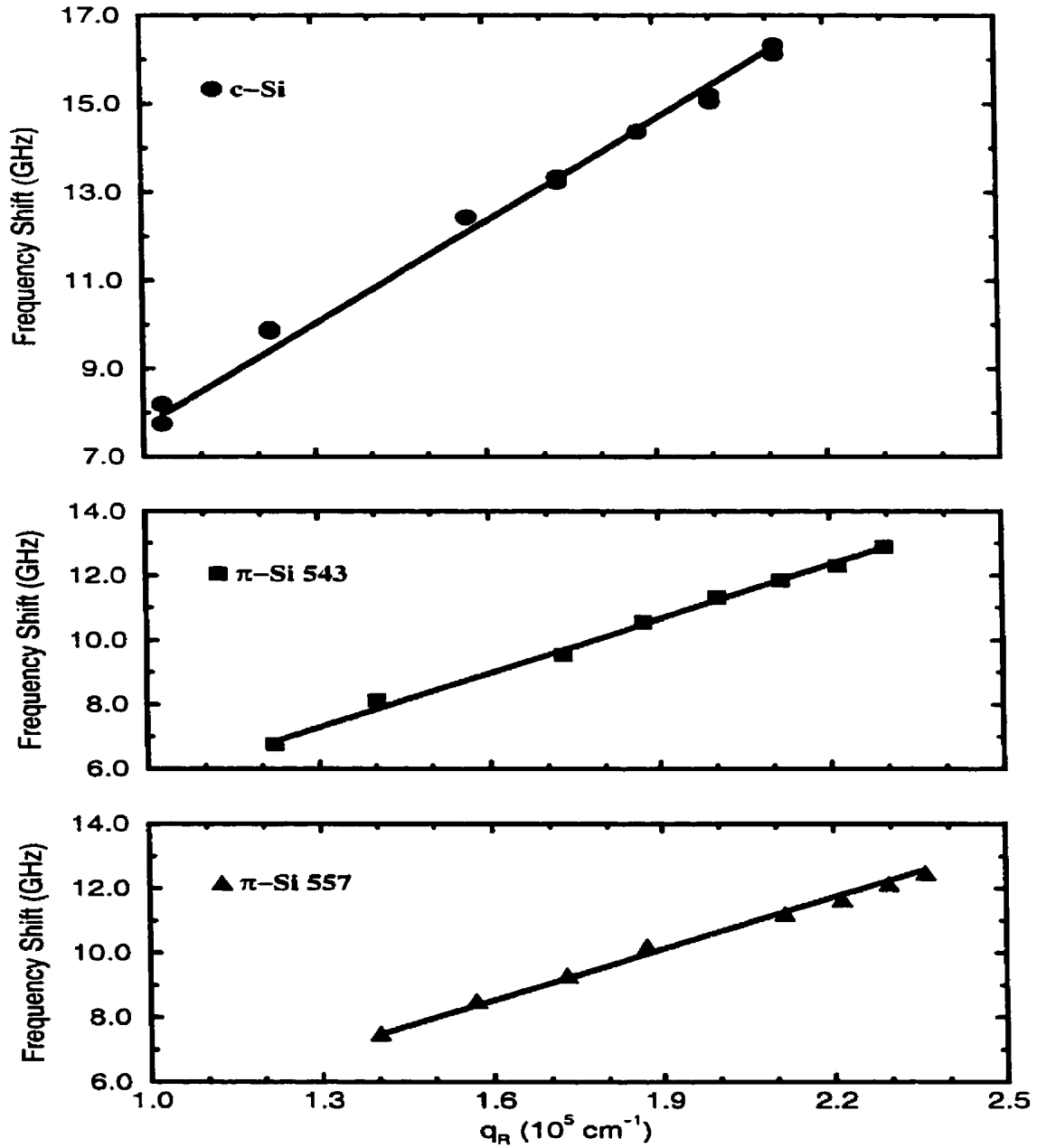
Figure 4.6: Brillouin frequency shift as a function of acoustic wavevector in $\sim$ [2$\bar{1}\bar{1}$] direction for $c - Si$ and $\pi - Si$ samples 543 and 557 from Set III.
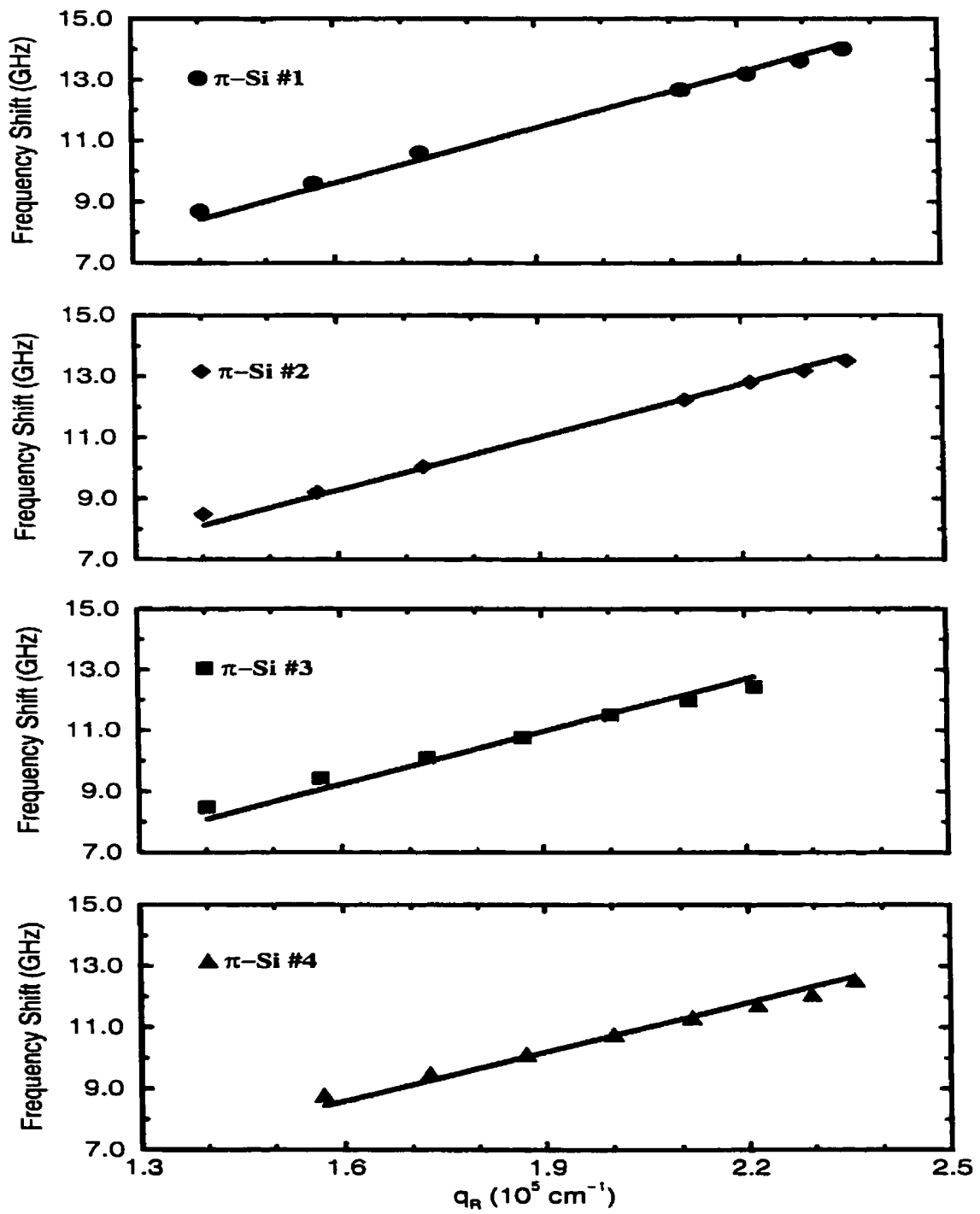
Figure 4.7: Brillouin frequency shift as a function of acoustic wavevector in ~ [2$\bar{1}\bar{1}$] direction for $\pi - Si$ samples #1-#4 from Set II.

angles greater than $\sim 65°$. The SAW velocities were determined using Equation 2.13. For all samples, an oscillatory behaviour in the SAW velocity with angular period $60°$ is observed as expected for the (111) plane of a cubic crystal.

It is well known that the SAW velocity on the (111) plane of cubic crystals depends on the material density ρ and the three elastic constants C_{11}, C_{12} and C_{44}. To determine the elastic constants of the $\pi - Si$ layers from the directional dependence of the SAW velocity, the density and starting values for the three elastic constants are required.

The SAW wavelengths probed in these experiments are much larger than the characteristic crystallite sizes found in p^+ type $\pi - Si$. For instance, an angle of incidence of $60°$ gives an acoustic wavelength of 297 nm, while a typical nanocrystallite diameter is ~ 10 nm. In such a case, the effective density of a $\pi - Si$ layer may simply be written,

$$\rho^{\pi-Si} = \rho^{c-Si}(1 - \xi),\tag{4.1}$$

where ρ^{c-Si} is the density of bulk crystalline silicon and ξ is the layer porosity. It should be noted that the small lattice expansion of $\pi - Si$ compared to $c - Si$ is neglected in this approximation.

Initial estimates of the elastic constants were calculated using various well-known expressions which relate the acoustic velocities to the elastic constants. In the $< 110 >$ directions the Rayleigh surface wave (RSW) velocity is given by $V_R \sim \beta\sqrt{C_{44}/\eta\rho}$, where $\beta \sim 0.9$ and $\eta = 2C_{44}(C_{11} - C_{12})^{-1}$ is the anisotropy factor. Using this relation with the measured values of $V_R^{\pi-Si}$ in the $[1\bar{1}0]$ direction, and assuming η lies between the value for $c - Si$ ($\eta = 1.56$) and that for an isotropic solid ($\eta = 1.00$), a reasonably good initial value of C_{44} was calculated. To obtain an estimate of C_{11}, the longitudinal acoustic velocity for a layer of identical porosity was determined from reference [52] and used along with the fact that, for an isotropic solid, this velocity depends only on C_{11} according to $V_L \sim \sqrt{C_{11}/\rho}$. Finally, a starting value for C_{12} was obtained by noting that

Table 4.4: Rayleigh mode frequency shifts and corresponding experimental and calculated velocities for various propagation directions on the (111) plane of sample #2 (nonporous region).

Raw Angle ($\pm0.5°$)	Angle from [$1\bar{1}0$] ($\pm0.5°$)	f_R^{c-Si} (±0.08 GHz)	$(V_R^{c-Si})_{exp}$ (±34 m·s^{-1})	$(V_R^{c-Si})_{cal}$ (m·s^{-1})
185.0	14.0	15.75	4678	4680
190.0	19.0	15.81	4696	4723
195.0	24.0	16.02	4759	4760
200.0	29.0	16.06	4771	4779
205.0	34.0	16.04	4765	4771
210.0	39.0	15.86	4711	4739
215.0	44.0	15.71	4667	4697
220.0	49.0	15.53	4613	4657
225.0	54.0	15.48	4598	4628
230.0	59.0	15.49	4601	4615
235.0	64.0	15.55	4619	4621
240.0	69.0	15.68	4658	4644
245.0	74.0	15.80	4693	4680
250.0	79.0	15.93	4732	4723
255.0	84.0	15.98	4747	4760
260.0	89.0	16.10	4782	4779
265.0	94.0	16.14	4794	4771
270.0	99.0	16.10	4782	4739
275.0	104.0	15.89	4720	4697
280.0	109.0	15.74	4676	4657
285.0	114.0	15.75	4678	4628

Table 4.5: Rayleigh mode frequency shifts and corresponding experimental and calculated velocities for various propagation directions on the (111) plane of sample #1.

Raw Angle ($\pm 0.5°$)	Angle from $[1\bar{1}0]$ ($\pm 0.5°$)	$f_R^{\pi-Si}$ (± 0.08 GHz)	$(V_R^{\pi-Si})_{exp}$ (± 30 m·s⁻¹)	$(V_R^{\pi-Si})_{cal}$ (m·s⁻¹)
70.0	-3.0	12.51	3716	3691
75.0	2.0	12.46	3701	3690
80.0	7.0	12.55	3728	3698
85.0	12.0	12.51	3716	3714
90.0	17.0	12.64	3755	3734
95.0	22.0	12.67	3764	3753
100.0	27.0	12.61	3746	3765
105.0	32.0	12.72	3778	3766
110.0	37.0	12.71	3775	3756
115.0	42.0	12.62	3749	3738
120.0	47.0	12.49	3710	3718
125.0	52.0	12.39	3680	3701
130.0	57.0	12.44	3695	3691
135.0	62.0	12.33	3663	3690
140.0	67.0	12.51	3716	3698
145.0	72.0	12.46	3701	3714
150.0	77.0	12.49	3710	3734
155.0	82.0	12.62	3749	3753
160.0	87.0	12.67	3764	3765
165.0	92.0	12.68	3767	3766
170.0	97.0	12.61	3746	3756
175.0	102.0	12.55	3728	3738
180.0	107.0	12.50	3713	3718
185.0	112.0	12.45	3698	3701
190.0	117.0	12.44	3695	3691
195.0	122.0	12.34	3666	3690

Table 4.6: Rayleigh mode frequency shifts and corresponding experimental and calculated velocities for various propagation directions on the (111) plane of sample #2.

Raw Angle ($\pm 0.5°$)	Angle from [1$\bar{1}$0] ($\pm 0.5°$)	$f_R^{\pi-Si}$ (± 0.08 GHz)	$(V_R^{\pi-Si})_{exp}$ (± 30 m·s^{-1})	$(V_R^{\pi-Si})_{cal}$ (m·s^{-1})
180.0	5.0	12.17	3615	3599
185.0	10.0	12.03	3573	3611
190.0	15.0	12.15	3609	3628
195.0	20.0	12.25	3639	3646
200.0	25.0	12.21	3627	3660
205.0	30.0	12.25	3639	3665
210.0	35.0	12.10	3594	3660
215.0	40.0	12.11	3597	3646
220.0	45.0	12.05	3579	3628
225.0	50.0	12.05	3579	3611
230.0	55.0	12.09	3591	3599
235.0	60.0	12.18	3618	3595
240.0	65.0	12.17	3615	3599
245.0	70.0	12.23	3633	3611
250.0	75.0	12.30	3654	3628
255.0	80.0	12.37	3674	3646
260.0	85.0	12.43	3692	3660
265.0	90.0	12.51	3716	3665
270.0	95.0	12.49	3710	3660
275.0	100.0	12.41	3686	3646
280.0	105.0	12.35	3669	3628
285.0	110.0	12.24	3636	3611

Table 4.7: Rayleigh mode frequency shifts and corresponding experimental and calculated velocities for various propagation directions on the (111) plane of sample #3.

Raw Angle ($\pm 0.5°$)	Angle from [1$\bar{1}$0] ($\pm 0.5°$)	$f_R^{\pi-Si}$ (± 0.08 GHz)	$(V_R^{\pi-Si})_{exp}$ (± 30 m·s^{-1})	$(V_R^{\pi-Si})_{cal}$ (m·s^{-1})
85.0	-5.0	11.71	3478	3515
90.0	0.0	11.72	3481	3512
95.0	5.0	11.64	3458	3515
100.0	10.0	11.90	3535	3524
105.0	15.0	12.00	3565	3536
110.0	20.0	11.97	3556	3549
115.0	25.0	11.97	3556	3559
120.0	30.0	12.01	3568	3562
125.0	35.0	11.91	3538	3559
130.0	40.0	11.91	3538	3549
135.0	45.0	11.83	3514	3536
140.0	50.0	11.82	3511	3524
145.0	55.0	11.82	3511	3515
150.0	60.0	11.71	3478	3512
155.0	65.0	11.83	3514	3515
160.0	70.0	11.84	3517	3524
165.0	75.0	11.91	3538	3536
170.0	80.0	12.09	3591	3549
175.0	85.0	11.94	3547	3559
180.0	90.0	11.91	3538	3562
185.0	95.0	11.95	3550	3559
190.0	100.0	12.06	3582	3549
195.0	105.0	12.03	3573	3536
200.0	110.0	12.01	3568	3524
205.0	115.0	11.95	3550	3515
210.0	120.0	12.08	3588	3512

Table 4.8: Rayleigh mode frequency shifts and corresponding experimental and calculated velocities for various propagation directions on the (111) plane of sample #4.

Raw Angle ($\pm 0.5°$)	Angle from $[1\bar{1}0]$ ($\pm 0.5°$)	$f_R^{\pi-Si}$ (± 0.08 GHz)	$(V_R^{\pi-Si})_{exp}$ (± 29 m·s^{-1})	$(V_R^{\pi-Si})_{cal}$ (m·s^{-1})
175.0	-20.0	11.28	3351	3331
170.0	-15.0	11.24	3339	3319
165.0	-10.0	11.23	3336	3308
160.0	-5.0	11.20	3327	3300
155.0	0.0	11.22	3333	3298
150.0	5.0	11.17	3318	3300
145.0	10.0	11.23	3336	3308
140.0	15.0	11.30	3357	3319
135.0	20.0	11.33	3366	3331
130.0	25.0	11.37	3377	3339
125.0	30.0	11.30	3357	3342
120.0	35.0	11.32	3363	3339
115.0	40.0	11.10	3297	3331
110.0	45.0	11.11	3300	3319
105.0	50.0	11.09	3294	3308
100.0	55.0	11.09	3294	3300
95.0	60.0	11.00	3268	3298
90.0	65.0	10.97	3259	3300
85.0	70.0	11.04	3279	3308
80.0	75.0	11.09	3294	3319
75.0	80.0	11.12	3303	3331
70.0	85.0	11.20	3327	3339
65.0	90.0	11.14	3309	3342
60.0	95.0	11.14	3309	3339
55.0	100.0	11.29	3354	3331

Table 4.9: Rayleigh mode frequency shifts and corresponding experimental and calculated velocities for various propagation directions on the (111) plane of sample 543.

Raw Angle ($\pm 0.5°$)	Angle from $[1\bar{1}0]$ ($\pm 0.5°$)	$f_R^{\pi - Si}$ (± 0.08 GHz)	$(V_R^{\pi - Si})_{exp}$ (± 30 m·s^{-1})	$(V_R^{\pi - Si})_{cal}$ (m·s^{-1})
225.0	-1.0	12.09	3517	3527
230.0	4.0	12.15	3514	3530
235.0	9.0	12.10	3514	3539
240.0	14.0	12.03	3541	3554
245.0	19.0	12.08	3541	3571
250.0	24.0	12.05	3559	3584
255.0	29.0	12.10	3576	3591
260.0	34.0	11.92	3588	3588
265.0	39.0	11.81	3579	3577
270.0	44.0	11.88	3538	3561
275.0	49.0	11.92	3541	3545
280.0	54.0	11.91	3529	3533
285.0	59.0	12.05	3508	3527
290.0	64.0	12.08	3541	3530
295.0	69.0	12.04	3594	3539
300.0	74.0	11.98	3579	3554
305.0	79.0	11.92	3588	3571
310.0	84.0	11.92	3573	3584
315.0	89.0	11.83	3594	3591
320.0	94.0	11.83	3609	3588
325.0	99.0	11.84	3591	3577

Table 4.10: Rayleigh mode frequency shifts and corresponding experimental and calculated velocities for various propagation directions on the (111) plane of sample 557.

Raw Angle ($\pm 0.5°$)	Angle from $[1\bar{1}0]$ ($\pm 0.5°$)	$f_R^{\pi-Si}$ (± 0.08 GHz)	$(V_R^{\pi-Si})_{exp}$ (± 29 m·s^{-1})	$(V_R^{\pi-Si})_{cal}$ (m·s^{-1})
232.0	-2.0	11.44	3330	3338
237.0	3.0	11.43	3336	3339
242.0	8.0	11.46	3363	3347
247.0	13.0	11.42	3363	3360
252.0	18.0	11.40	3354	3376
257.0	23.0	11.38	3392	3389
262.0	28.0	11.32	3392	3397
267.0	33.0	11.27	3389	3396
272.0	38.0	11.28	3371	3387
277.0	43.0	11.16	3380	3373
282.0	48.0	11.25	3351	3357
287.0	53.0	11.28	3342	3345
292.0	58.0	11.38	3315	3338
297.0	63.0	11.35	3351	3339
302.0	68.0	11.41	3348	3347
307.0	73.0	11.42	3363	3360
312.0	78.0	11.42	3380	3376
317.0	83.0	11.29	3386	3389
322.0	88.0	11.32	3392	3397
327.0	93.0	11.32	3404	3396
332.0	98.0	11.23	3395	3387
337.0	103.0	11.21	3398	3373

the bulk modulus $B = \rho(3\bar{V}_L^2 - 4\bar{V}_T^2)/3$ may be calculated if the average transverse and longitudinal acoustic velocities, $\bar{V}_T$ and $\bar{V}_L$, are known. Taking the values of transverse and longitudinal velocities determined from the empirical expressions of reference [53] as the average velocities, it was possible to determine the bulk moduli for layers of relevant porosities. For a cubic crystalline solid the bulk modulus is related to the elastic constants by $B = (C_{11} + 2C_{12})/3$. Thus, once an initial estimate of C_{11} was known. a starting value for C_{12} could be determined. It proved necessary to include the constraint $3B = C_{11} + 2C_{12}$ in the fitting routine to prevent problems in achieving a best-fit.

The three initial guesses for the elastic constants and the density serve as input for a nonlinear least-squares fitting program based on the simplex method [86]. The quantity to be minimized was

$$\chi^2 = \sum_{i=1}^{n} \frac{((V_R^{\pi-Si})_{exp}^i - (V_R^{\pi-Si})_{cal}^i)^2}{\sigma^2} \tag{4.2}$$

where $(V_R^{\pi-Si})_{exp}^i$ are the n observed surface acoustic wave velocities, $(V_R^{\pi-Si})_{cal}^i$ are the n calculated velocities and σ is the estimated uncertainty in the measured velocities. To test that the program was working properly, data collected from the nonporous region of sample #2 of Set II (see Table 4.4) was used to determine the zero porosity $(c-Si)$ elastic constants. The best-fit to the experimental data is shown in Figure 4.8. The results are given in Table 4.11 and agree with the accepted values for $c - Si$ ($C_{11}^{c-Si} = 166.0$ GPa, $C_{12}^{c-Si} = 63.9$ GPa, $C_{44}^{c-Si} = 79.6$ GPa [87]) to better than 2%.

Once it was ascertained that the program was working properly, the elastic constants of several $\pi - Si$ layers were determined from the directional dependence of the surface wave velocity. The best-fit elastic constants are shown in Table 4.11. The indicated uncertainties in the elastic constants were determined by adding the average difference between the experimental and best-fit velocities to all the experimental velocities and rerunning the fitting routine to obtain a second set of elastic constants. The respective
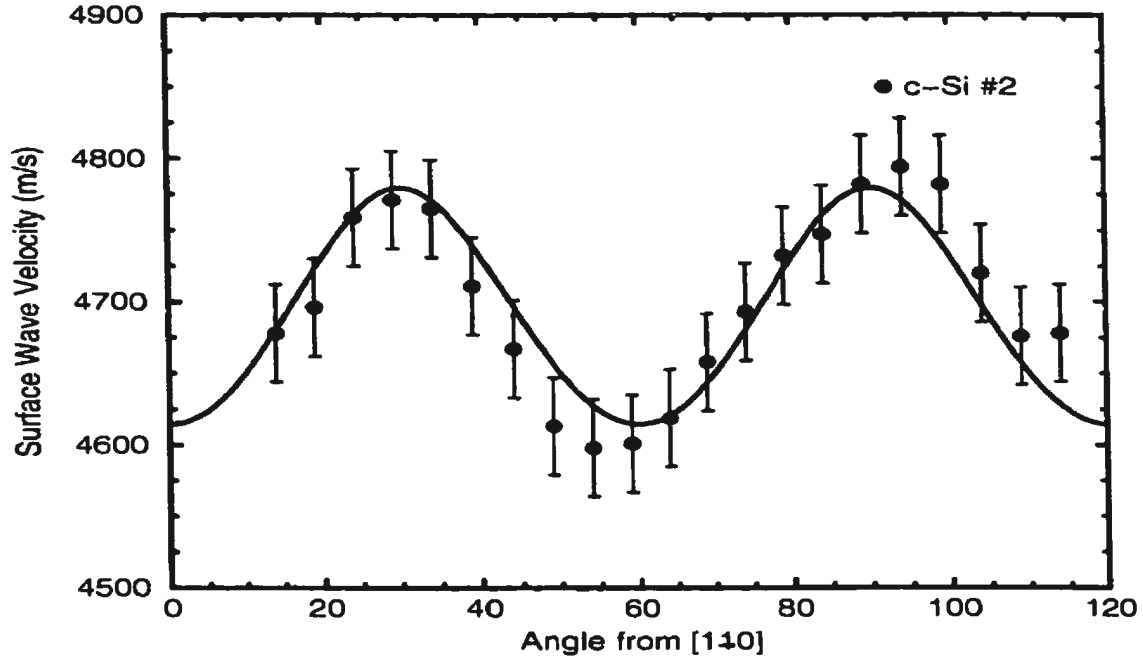
Figure 4.8: Directional dependence of SAW velocity for the nonporous (crystalline) part of sample #2. The theoretical curve (solid line) was obtained from best-fit elastic constants given in Table 4.11.

differences between the two sets of constants were taken as the approximate statistical errors. Sample fits are shown in Figure 4.9 and the agreement with the experimental data is quite good.

As is evident, the elastic constants for all the $\pi - Si$ layers are significantly lower than those for $c - Si$, especially C_{12}, which is lower by about an order of magnitude. Also, given in Table 4.12 are Young's modulus in the [100] direction $E = C_{11} - 2C_{12}^2(C_{11} + C_{12})^{-1}$, Poisson's ratio $\sigma = C_{12}(C_{11} + C_{12})^{-1}$ and the elastic anisotropy factor η. In each case, the elastic anisotropy η lies in the range $1.00 \leq \eta \leq 1.56$ as expected. The fact that it is greater than unity in all cases implies that the $\pi - Si$ layers are not elastically isotropic as suggested by other authors [22, 52, 53] but retain, at least partially, the crystalline
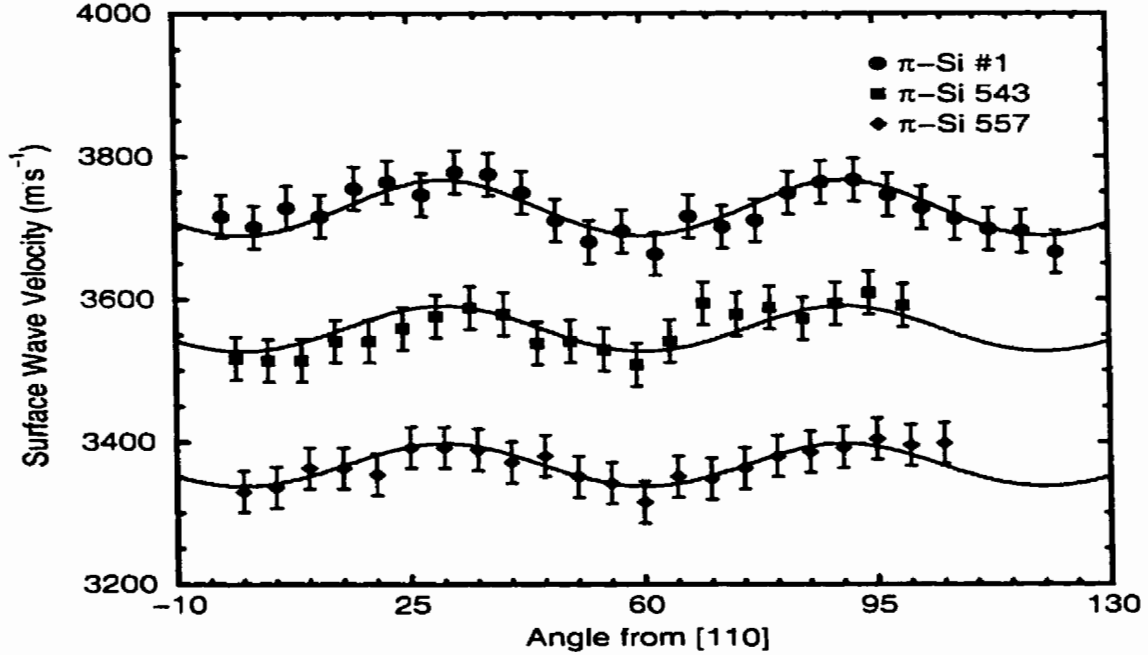
Figure 4.9: Directional dependence of SAW velocity for sample #1 of Set II and samples 543 and 557 of Set III. The theoretical curves (solid lines) were obtained from the best-fit elastic constants given in Table 4.11.

character of the parent wafers. It is interesting to note that for samples #1-#4 of Set II, the anisotropy decreases with increasing porosity as do Poisson's ratio and Young's modulus. This may be due to some misorientation of crystallites.

4.1.3 Influence of Adsorbed Water on the Velocity of Surface Acoustic Phonons in Low Porosity $\pi - Si$

Brillouin spectra were collected from samples 539 ($\xi = 32\%$) and 557 ($\xi = 29\%$) of Set III at angles of incidence of 50° and 60°, respectively, using the optical system which incorporated the five-pass spectrometer. The FSR was set at 19.04 GHz for all spectra. Spectra were collected from the same spot on each sample before and after the treatment

Table 4.11: Elastic constants for the crystalline region of sample #2 and various $\pi - Si$ layers.

Sample	ξ (%)	C_{11} (GPa)	C_{12} (GPa)	C_{44} (GPa)
$c - Si$ #2	0	168.5 ± 1.2	62.6 ± 0.6	79.0 ± 1.3
$\pi - Si$ #1	30	56.4 ± 0.7	6.4 ± 0.3	35.9 ± 0.8
$\pi - Si$ #2	32	52.1 ± 0.7	5.8 ± 0.4	32.7 ± 0.6
$\pi - Si$ #3	35	47.2 ± 0.6	4.3 ± 0.3	28.9 ± 0.7
$\pi - Si$ #4	40	38.1 ± 0.6	3.0 ± 0.3	23.5 ± 0.6
$\pi - Si$ 543	28	56.3 ± 0.3	9.5 ± 0.2	32.0 ± 0.3
$\pi - Si$ 557	29	51.5 ± 0.2	10.4 ± 0.1	27.8 ± 0.2

described in Section 3.3. No obvious changes in the appearance of the spectra occurred as a result of the heat treatment. The Brillouin frequency shifts and corresponding velocities are summarized in Table 4.13. For both samples, the frequency shift of the RSW prior to the heat treatment is the same as the post-heat treatment value within experimental error. Thus no measurable change in the RSW velocity was observed for either sample.

4.1.4 Influence of Thin Native Oxide Films on the Velocity of Surface Acoustic Phonons in Low Porosity $\pi - Si$

Brillouin scattering experiments were carried out on three separate $\pi - Si$ samples to determine the effect of native oxide films on the Rayleigh surface acoustic wave velocity. In total, 30 Brillouin spectra were collected from both the air stored and HF dipped pieces of samples 541, 542 and 557. Five separate spectra were obtained from five different locations on each piece giving five SAW velocities (sample orientation remained fixed). These velocities were then used to calculate an average SAW velocity for each piece. As can be seen in Table 4.14, the average SAW velocities (and, in fact, each individual velocity) for the HF-dipped pieces are measurably lower than those for the corresponding

Table 4.12: Young's modulus (E) in the [100] direction, Poisson's ratio (σ) and anisotropy factor (η) for the crystalline region of sample #2 and various porous layers.

Sample	ξ (%)	E [100] (GPa)	σ	η
$c - Si$ #2	0	134.6 ± 1.3	0.271 ± 0.003	1.49 ± 0.03
$\pi - Si$ #1	30	55.1 ± 0.7	0.102 ± 0.005	1.44 ± 0.04
$\pi - Si$ #2	32	50.9 ± 0.7	0.100 ± 0.007	1.41 ± 0.04
$\pi - Si$ #3	35	46.5 ± 0.6	0.083 ± 0.006	1.35 ± 0.04
$\pi - Si$ #4	40	37.7 ± 0.6	0.073 ± 0.007	1.34 ± 0.04
$\pi - Si$ 543	28	53.6 ± 0.3	0.144 ± 0.003	1.37 ± 0.02
$\pi - Si$ 557	29	48.0 ± 0.2	0.168 ± 0.002	1.35 ± 0.01

undipped pieces. It is also worth noting that the relatively small range of velocities within each set of five suggests that the layers are very uniform (acoustically).

A pair of Brillouin spectra collected from the undipped and HF-dipped pieces of sample 541 of Set III is shown in Figure 4.10. The surface mode for the undipped sample has a frequency shift of 11.47 GHz corresponding to a velocity of 3407 m·s^{-1}. The frequency shift for the HF-dipped, sample is 10.87 GHz giving a surface phonon velocity of 3229 m·s^{-1}. Shifts of similar magnitude were also observed for samples 542 and 557 (see Table 4.14). In fact, the average SAW velocities for the HF-dipped pieces range from 3% to 6% smaller than those of the corresponding pieces which were not HF-dipped.

Table 4.13: SAW frequency shifts and corresponding velocities for samples 539 and 557 of Set II both before and after the treatment described in section 3.3.

Sample	ξ (%)	θ_i ($\pm0.5°$)	Pre-heat-treatment		Post-heat-treatment	
			$f_R^{\pi-Si}$ (±0.08 GHz)	$V_R^{\pi-Si}$ (m·s^{-1})	$f_R^{\pi-Si}$ (±0.08 GHz)	$V_R^{\pi-Si}$ (m·s^{-1})
$\pi - Si$ 539	32	50	8.49	2851 ± 34	8.40	2821 ± 34
$\pi - Si$ 557	29	60	11.05	3282 ± 29	11.04	3279 ± 29

Table 4.14: Surface acoustic wave frequencies and corresponding velocities before and after a 10 s dip in a 5% HF solution. The FSR was 19.04 GHz in all cases.

Sample	No HF Dip			HF Dip		
	$f_R^{\pi-Si}$ (±0.08 GHz)	$V_R^{\pi-Si}$ (±30 m·s^{-1})	$< V_R^{\pi-Si} >$ (m·s^{-1})	$f_R^{\pi-Si}$ (±0.08 GHz)	$V_R^{\pi-Si}$ (±30 m·s^{-1})	$< V_R^{\pi-Si} >$ (m·s^{-1})
541	11.46	3404	3418	10.84	3220	3212
	11.47	3407		10.86	3226	
	11.53	3425		10.72	3184	
	11.45	3401		10.77	3199	
	11.62	3452		10.87	3229	
542	11.92	3541	3559	11.34	3369	3398
	11.97	3556		11.44	3398	
	12.00	3565		11.31	3360	
	12.04	3576		11.67	3467	
	11.98	3559		11.44	3398	
557	11.17	3318	3310	10.77	3199	3216
	11.07	3288		10.82	3214	
	11.18	3321		10.89	3234	
	11.09	3294		10.84	3220	
	11.20	3327		10.81	3211	

4.2 Raman Scattering

4.2.1 General Features of the Raman Spectrum of $\pi - Si$

First-order Raman spectra were collected from samples A-E of Set I. This set consists of porous layers fabricated from both p^- and p^+ type substrates as shown in Table 3.1. A Raman spectrum was also collected from the nonporous (crystalline) region of sample #1 of Set II for reference.

A plasma line which appeared in the Raman spectra excited by the Ar^+ blue line at 487.986 nm (20492.4 cm^{-1}) [88] was used as a standard and allowed the Raman shifts of the first-order peaks to be determined with an accuracy of $\sim$ 0.5 cm^{-1}. The wavelength of the plasma discharge light which causes this plasma line is 500.9334 nm (19962.73 cm^{-1}) and so it appears in the Raman spectra (excited by the Ar^+ blue line) at a shift of
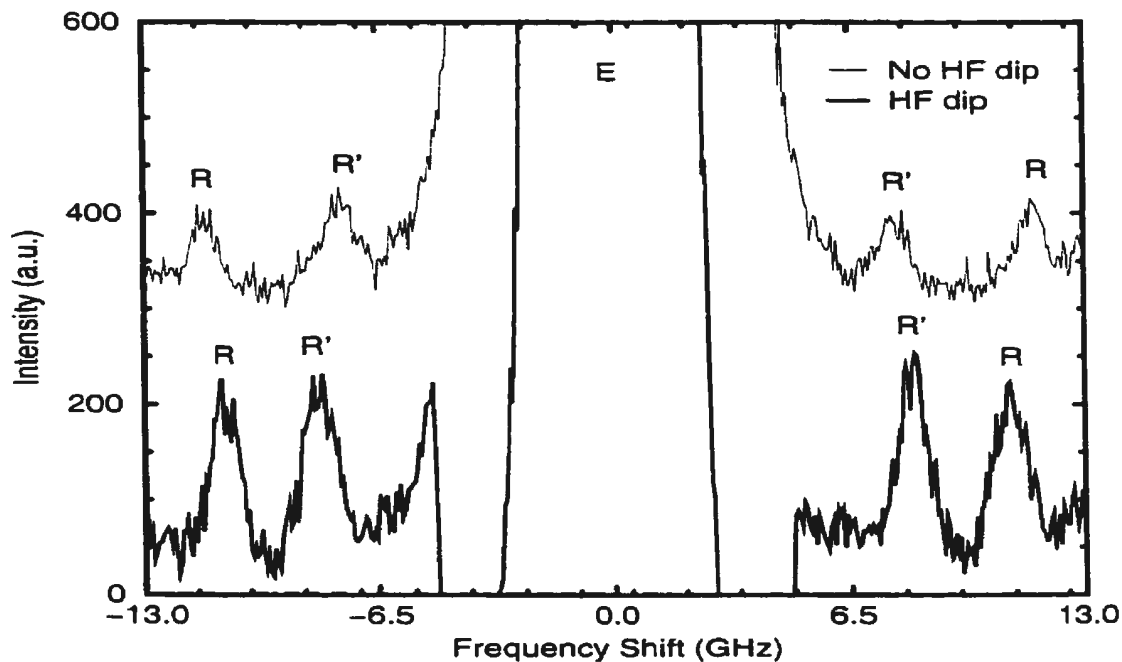
Figure 4.10: Brillouin spectra of the HF-dipped and undipped pieces of sample #541. The FSR for both spectra was 19.04 GHz and the angle of incidence was 60°. The phonon propagation direction was along [2$\bar{1}\bar{1}$].

529.7 cm^{-1}. In the case of the $c - Si$ spectrum, the plasma line (fitted to a Gaussian) was located at a shift of 512.2 cm^{-1}, resulting in a correction of 17.5 cm^{-1} being applied to this spectrum. Similar corrections were applied to other Raman spectra of the present study. A Lorentzian was fitted to the first-order $c - Si$ Raman peak and its $FWHM$ and uncorrected shift were determined to be 5.5 cm^{-1} and 502.9 cm^{-1}, respectively. The corrected first-order $c - Si$ Raman peak shift was 520.4 cm^{-1} which agrees very well with numerous other studies [27, 28, 31, 37, 45].

The Raman spectra collected from samples A-E of Set I are shown in Figures 4.11 and 4.12. Nearly all of them have first-order Raman peaks at smaller shifts than the first-order peak of $c - Si$ and linewidths ($FWHM$) which are greater than the $FWHM$
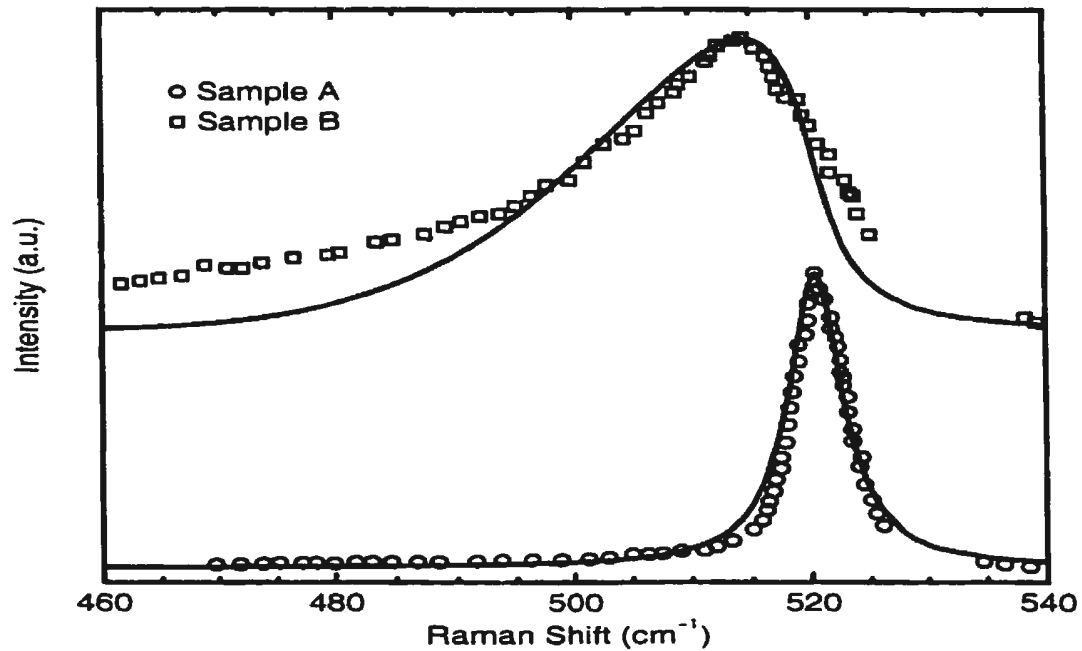
Figure 4.11: Room temperature Raman spectra of $\pi - Si$ layers formed from p^- type Si substrates. Sample A has a porosity of 80% and a layer thickness of 5 μm. Sample B has a porosity of 80% and a layer thickness of 20 μm. The spectra were recorded with the 488.0 nm Ar^+ laser line in a quasi-backscattering geometry. The solid curves are theoretical spectra calculated from the phonon confinement model outlined in Chapter 2.

of $c - Si$.

The Raman spectra of samples A and B (formed from p^- type substrates), both of 80% porosity, have asymmetric shapes with extended tails at low Raman shifts (see Figure 4.11). The Raman peak of layer A (5 μm thickness) is practically unshifted from the $c - Si$ peak position and its $FWHM$ is about the same (~ 5 cm^{-1}). The bulk-like character of this peak may be indicative of the presence of crystallites with characteristic sizes larger than 20 nm. This would be very unusual for such a layer (formed from a p^- type substrate and of high porosity). It is more likely that, due to the high layer
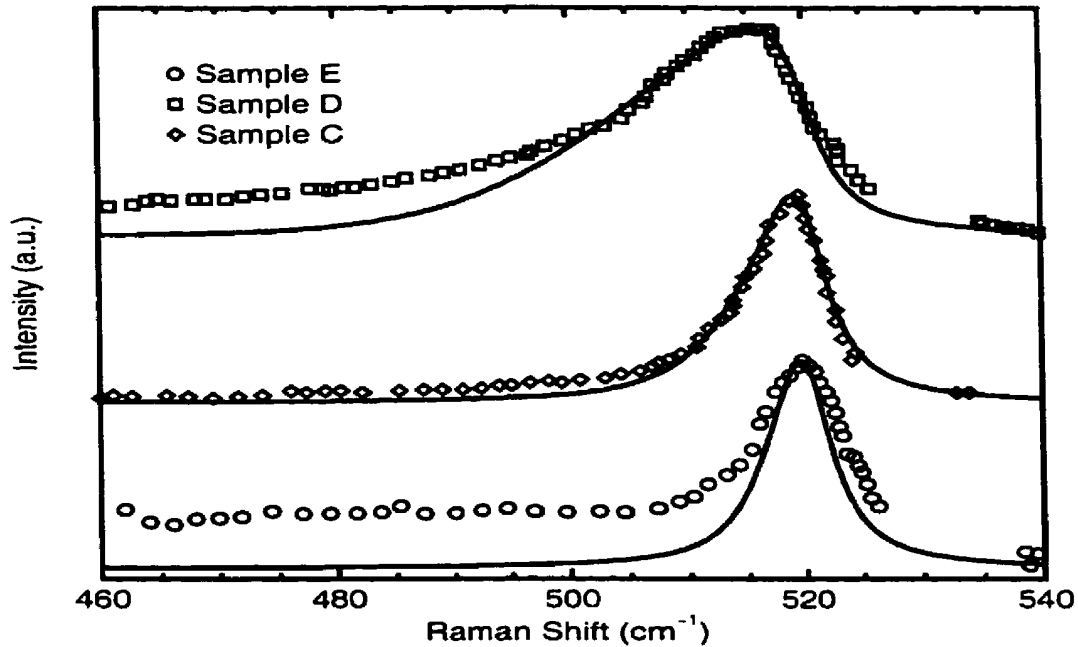
Figure 4.12: Room temperature Raman spectra of $\pi - Si$ layers formed from p^+ type Si substrates. Sample C has a porosity of 65% and a thickness of 10.5 μm. Sample D has a porosity of 80% and a thickness of 80 μm. Sample E has a porosity of 35% and an unknown layer thickness. The spectra were recorded with the 488.0 nm Ar^+ laser line in a quasi-backscattering geometry. The solid curves are theoretical spectra calculated from the phonon confinement model outlined in Chapter 2.

porosity, a strong Raman signal from the substrate dominates the scattering. In fact, it may be argued that the slight asymmetry of the first-order Raman line of sample A is evidence of this. Layer B, with a thickness of 20 μm, exhibits a completely different, much broader, Raman band. This $\pi - Si$ layer was prepared at an anodization current density of $J = 40$ mA·cm^{-2}, $i.e.$, at twice the current for sample A. The Raman peak of sample B has a large $FWHM$ of 24 cm^{-1} and a shift of 513.9 cm^{-1}, which is 6.5 cm^{-1} lower than the Raman shift of the first-order line of $c - Si$. These two values ($FWHM$ = 24 cm^{-1} and $\Delta\omega^{\pi-Si}$ = 6.5 cm^{-1}) are the largest of all the samples in the present work

Table 4.15: First-order Raman peak shifts, $FWHM$ and asymmetry factors for porous samples C, D and E of Set I.

Sample	Porosity (%)	Raman Shift (± 0.5 cm^{-1})	$FWHM$ (± 1.0 cm^{-1})	Γ_a/Γ_b
E	35	519.5	10.0	1.1
C	65	518.9	8.3	1.4
D	80	514.7	19.9	2.0

(see Table 4.16).

Three different $\pi - Si$ samples (C, D and E) formed on p^+ type substrates were also studied. Their Raman spectra are shown in Figure 4.12 and the corresponding shifts and linewidths are given in Table 4.15. The Raman shift of the first-order peak decreases with increasing porosity (see Table 4.15). The peak asymmetry, measured using the ratio of the $HWHM$ on the low Raman shift side to the $HWHM$ on the high Raman shift side, Γ_a/Γ_b, also increases with increasing porosity. The Raman peaks of samples C and E, with porosities of 65% and 35%, respectively, have maxima located at slightly lower Raman shifts (< 2 cm^{-1}) than the $c - Si$ line and are moderately broadened ($FWHM$ of $8 - 10$ cm^{-1}) (see Table 4.16). The first-order peak in the Raman spectrum of sample D (80 μm thickness, 80% porosity) has a linewidth of 19.9 cm^{-1} and is located at a Raman shift which is 5.7 cm^{-1} lower than the corresponding line for $c - Si$. These values are larger than the typical ones for p^+ type $\pi - Si$ and, in fact, are quite similar to those of sample B, fabricated on the p^- type Si substrate.

To investigate the effect of excitation wavelength on the Raman spectrum of $\pi - Si$, spectra were collected from sample D using Ar^+ wavelengths of 488.0 nm and 514.5 nm. It was noticed that increasing the laser excitation wavelength from 488.0 nm to 514.5 nm resulted in an increase in the Raman shift of the first-order $\pi - Si$ peak accompanied by a decrease in linewidth. In addition, a double-peak structure was observed when using

514.5 nm Ar$^+$ laser excitation but only a single Raman peak was present under 488.0 nm excitation. The double-peak structure consisted of a sharp peak located at a Raman shift of 521 cm^{-1} and a broad asymmetric component at lower Raman shift (typical of $\pi - Si$).

Initially, the sharply-peaked component was thought to be due to a contribution to the Raman spectrum from the $c - Si$ substrate since the Raman shift of the first-order $c - Si$ peak is 520.4 ± 0.5 cm^{-1}. However, the layer thickness of 80 μm made this origin seem unlikely. It was subsequently discovered that this peak was still observed after the sample had been replaced with a piece of white cardboard and hence was not due to Raman scattering. In fact, the narrow 521 cm^{-1} component of the spectrum recorded using 514.5 nm incident light corresponds to an Ar$^+$ plasma line at 528.7 nm.

It is obvious that the near coincidence of this line with the Stokes component of the $c - Si$ Raman spectrum ($\Delta\omega^{c-Si} = 520.4 \pm 0.5$ cm^{-1}) or other lines located at similar Raman shifts could be a source of misinterpretations (for 514.5 nm Ar$^+$ excitation). Some of the 514.5 nm-excited Raman spectra of the present work showed no evidence of the plasma line. Its appearance and intensity in the Raman spectrum probably depend on the reflectivity of a particular sample and the scattering geometry which both influence how much plasma discharge light is detected by the collection optics.

Double-peak structure has been observed in Raman spectra excited with other Ar$^+$ lines [35, 45, 89]. In these instances there are no Ar$^+$ plasma lines located as close to the interesting spectral region and the peak with the higher Raman shift must be due to some other effect such as the LO contribution to the spectrum arising from LO-TO splitting [35] or contributions from the $c - Si$ substrate in the case of thin and/or highly porous layers [45, 89]. No splitting of LO and TO phonon modes has been observed in the present experiment. Also, computer simulations of the Raman line shapes, based on the phonon confinement model described in Chapter 2, did not exhibit double peaks because

of large broadenings of the LO and TO contributions in comparison to their separations.

4.2.2 Estimates of Nanocrystallite Size and Shape

It is of interest to know the average size, L, of the nanocrystals in a given $\pi - Si$ sample. The phonon confinement model outlined in Section 2.3 may be used for such a purpose. For a given crystallite size and shape (in this work spherical or cylindrical), the calculated Raman spectrum has a specific linewidth and Raman shift. Thus, by varying L and comparing the calculated and experimental spectra, an estimate of the characteristic nanocrystallite size present in a sample can be obtained. This method was used to determine crystallite sizes for samples B through E of Set I. Estimates of nanocrystallite size could not be obtained from sample A of Set I using this procedure because the shift and linewidth of the first-order peak were very similar to those for $c - Si$. As discussed in the previous section, this indicates that the characteristic crystallite size in this layer is > 20 nm and/or that the Raman signal from the porous layer is swamped by scattering from the $c - Si$ substrate.

In order to calculate the Raman spectrum produced by crystallites of average size L from the phonon confinement model, expressions for the $c - Si$ optical phonon dispersion curves ($\omega(q)$) were required. These were obtained by fitting cubic expressions of the form $\omega(q) = W + Xq + Yq^2 + Zq^3$ to the combined neutron scattering data of Kulda et al. [90] and Dolling et al. [91] in the [100] direction. Here, q is the reduced wavevector (expressed in units of $2\pi/a$) and $W = 520.4$ cm^{-1} (the Raman shift of the first-order peak of $c - Si$). The best-fits reproduced the experimental results very well. The resulting expressions were $\omega_T(q) = 520.4 - 20.1q - 188.1q^2 + 147.7q^3$ and $\omega_L(q) = 520.4 + 4.0q - 83.3q^2 - 28.2q^3$ for the TO and LO phonons, respectively. In all cases it was assumed that the LO and TO phonons contributed equally to the Raman spectrum. These expressions along with the $FWHM$ of the first-order $c - Si$ Raman line (~ 5.5 cm^{-1}) and the lattice

Table 4.16: Raman shifts ($\Delta\omega^{\pi-Si}$), full widths at half maximum ($FWHM$) and photoluminescence (PL) maxima for the $\pi - Si$ samples of Set I. L is the characteristic crystallite size determined from the phonon confinement model. S and W denote the characteristic crystallite shape (spherical or wire-like).

Sample	Type	ϵ (%)	$\Delta\omega^{\pi-Si}$ (±0.5 cm^{-1})	$FWHM$ (±1.0 cm^{-1})	L (nm)	PL (±0.01 eV)
A	p^-	80	520.4	5.2	—	1.69
B	p^-	80	513.9	24.3	4.6 ± 0.2 s	1.78
C	p^+	65	518.9	8.3	9.5 ± 0.5 w	1.63
D	p^+	80	514.7	19.9	5.2 ± 0.2 s	1.67
E	p^+	35	519.5	10.0	16.0 ± 1.0 w	1.60

parameter of $c - Si$ (0.543 nm) were then substituted into Equation 2.33 or its two-dimensional analogue to yield the Raman spectrum of the relevant layer. Figure 4.11 shows a comparison of the experimental and theoretical Raman line shapes for samples A and B of Set I. Similar spectra for samples C, D and E of Set I are given in Figure 4.12. The estimated values of the nanocrystallite diameters are given in Table 4.16. The indicated uncertainties in L were estimated by incrementally changing the nanocrystallite size until a there was a noticeable difference between the optimum calculated spectrum (*i.e.*, the one which best-fit the experimental spectrum) and the experimental spectrum. The difference in these two values for L was taken as the approximate uncertainty.

In the case of sample A, with a first-order Raman peak shifted the same amount as that for $c - Si$, the calculations were performed using a very large (essentially infinite) crystallite size. In such a case the shape is irrelevant. For sample B (porosity 80%), a spherical crystallite diameter of 4.6 nm gave the best agreement between theory and experiment. This shape and small crystallite size are characteristic of high porosity $\pi - Si$ layers formed from p^- type substrates. The similarity of the experimental and calculated spectra is quite evident in Figure 4.11, but it is also clear that the full Raman spectrum of sample B can be modelled in such a simple way in a first approximation only.

The tail at low Raman shifts, as well as the discrepancy for shifts above 520.4 cm^{-1}, indicate that crystallites of other sizes are present in this sample.

In contrast to sample B, the best agreement between the calculated and experimental Raman spectra of samples C and E (65% porosity) was obtained using cylindrical (wire-like) rather than spherical nanocrystallite shapes. The characteristic wire diameters were 9.5 nm and 16.0 nm for samples C and E, respectively. Sample D (porosity 80%), which was also fabricated from p^+ type $c - Si$, has a significantly smaller Raman shift and a larger linewidth than samples C and E of lower porosity (see Table 4.16). In this instance, the best agreement between theory and experiment was obtained using a spherical crystallite of diameter 5.2 nm.

4.2.3 Photoluminescence Spectra

PL spectra of all five $\pi - Si$ samples are shown in Figure 4.13. These spectra were recorded using the same experimental setup as for the Raman scattering experiments, but were excited with the Ar$^+$ green line at 514.5 nm. The PL peak energies have been tabulated in Table 4.16 along with the Raman data.

Samples A and B, which were both formed on p^- type Si and have the same porosity, have very different PL spectra. The spectrum of sample A is one of the most intense observed in the present study and is relatively typical for a high porosity $\pi - Si$ layer formed from a p^- type substrate. The PL spectrum on sample B, on the other hand, shows a very feeble emission (approximately two orders of magnitude lower than that for sample A) peaked at about 1.78 eV.

The PL spectra collected from the samples prepared from p^+ type Si (C, D and E) exhibit a trend. For these layers, it is clear from Figure 4.13 and Table 4.16 that the PL spectrum intensity increases and blue-shifts with increasing sample porosity. This is in

74
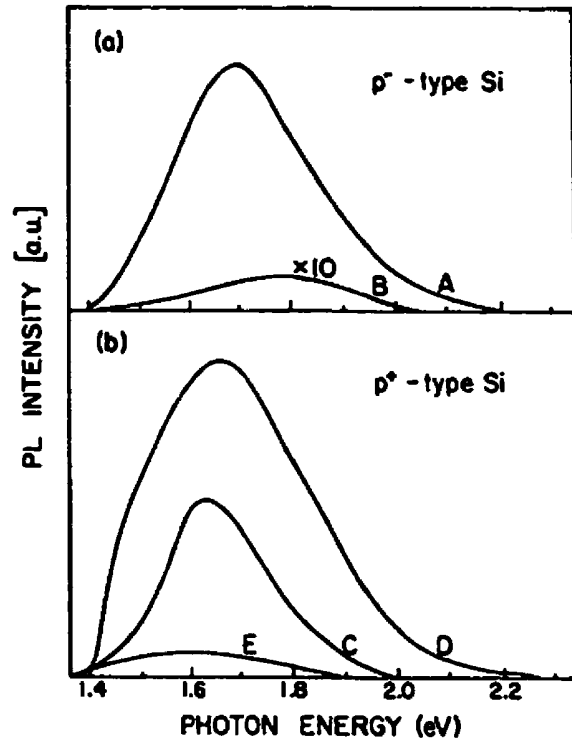
Figure 4.13: Room temperature PL spectra of the $\pi - Si$ layers of Set I formed from p^- type (A and B) and p^+ type (C, D and E) $c - Si$ substrates. The spectra were recorded with the 514.5 nm Ar^+ laser line in a quasi-backscattering geometry.

accord with the results expected for the quantum confinement origin of PL and will be discussed in greater detail in the following chapter.

Chapter 5

Discussion

5.1 Elastic Properties of $\pi - Si$

5.1.1 Surface Acoustic Wave Velocities

(i) Effect of Porosity

Considerable softening of the SAW velocity compared to that for $c - Si$ was observed for all $\pi - Si$ layers of the present work. For instance, for samples #1-#4 of set II, ($\xi = 30\% - 40\%$), the SAW velocity for phonons propagating in the $[2\bar{1}\bar{1}]$ direction ranges from 20% to 30% lower than the corresponding velocity for $c - Si$ (4840 m·s^{-1}). The SAW velocities for the samples of set III, which have similar porosities, are smaller than the $c - Si$ value by approximately the same amount. Also, for a given set, the velocity decreases with increasing porosity.

Similar results were obtained in microacoustic experiments [53] on $\pi - Si$ layers formed from p^+ type $c - Si$. In this study, the SAW velocity was determined from the Fourier transform spectra of the material acoustic signature and ranged from 4005 m·s^{-1} to 2270 m·s^{-1} for samples with porosities between 20% and 47%. The SAW velocity decreased with increasing porosity as observed in the current Brillouin scattering experiments. It should be noted that a quantitative comparison of the results from these two studies is not possible because the anisotropy of the porous layers was not taken into account in the microacoustic experiments.

76

The SAW velocity for phonons propagating in the [110] direction has also been measured as a function of the product of the measured frequency and the film thickness by phase velocity scanning of laser interference fringes [60]. These experiments were carried out on (001)-oriented samples with resistivities of $0.1 - 0.2$ Ω·cm and $10 - 20$ Ω·cm (both p^- type) and porosities in the range 41%-60%. Again, the SAW velocity was observed to decrease with increasing porosity as in the Brillouin scattering and microacoustic experiments. It was further noted that the measured velocities of these samples were as low as one-half to one-third the corresponding value for $c - Si$.

The softening of acoustic velocities in porous materials relative to their nonporous counterparts seems to be a general phenomenon and has been observed in numerous experiments on a wide range of materials.

(ii)   Effect of Native Oxide Film

The presence of native oxide films on $\pi - Si$ layers also affects the SAW velocity as evident from the results of the HF-dip experiments in Chapter 4. Such films are formed gradually on the hydrogen passivated surface of freshly etched $\pi - Si$ during storage in ambient air and typically have thicknesses of a few nanometres. This is small compared to the SAW wavelength and thus the SAW velocity should only be slightly perturbed by its presence on the $\pi - Si$ layer. The relatively small change in SAW velocity ($\sim 3\% - 6\%$) between the HF-dipped and air stored samples is consistent with this assumption and indicates that the native oxide films formed on the layers are quite thin. This is also in agreement with the results of optical studies on similarly-doped layers where it was concluded that only a small amount of oxide was present on layers formed from p^+ type substrates.

The presence of an oxide layer was also recognized in Brillouin light scattering experiments on Al-coated $GaAs$ and Si [92]. The film formed on the surface of the Al and

had an estimated thickness of 2-3 nm. This was much smaller than the wavelength of the phonons excited in the Al film and hence it was concluded that the oxide layer did not affect their measurements. The oxide layers in the present case are of comparable thickness and their effect on the SAW velocity is quite apparent as mentioned above. There is, however, a major difference between the Brillouin scattering experiments on the Al-coated semiconductors and the present work. In the former, the oxide formed on an optically flat Al surface, whereas the $\pi - Si$ surface is quite convoluted and has a very high surface area.

(iii)   Effect of Adsorbed Water

It was also seen earlier that heating low porosity $\pi - Si$ layers formed from p^+ type substrates under vacuum resulted in no change in the SAW velocity compared to pre-heat treatment values (see Table 4.13). The fact that both pre- and post-treatment velocities were the same within experimental error could indicate that there is adsorbed water on the $\pi - Si$ surface, but that the quantity is insufficient to alter the SAW velocity. It is difficult to determine the amount of adsorbed water necessary to effect such a change, but given the high specific surface area of $\pi - Si$ and the storage period of several months in humid air, it is not unreasonable to expect a difference between the pre- and post-treatment velocities.

A second possibility is that adsorbed water cannot be removed by such a simple heat/vacuum treatment because it has reacted with the $\pi - Si$ surface in some way. What water does when it comes into contact with the $\pi - Si$ surface is widely debated. There does, however, seem to be a consensus that it plays a significant role in the room temperature oxidation of $\pi - Si$ in ambient air. Fourier transform infrared (FTIR) studies performed on $\pi - Si$ samples under ultrahigh vacuum reveal that H_2O initially dissociates upon adsorption at 300 K (room temperature) to form SiH and $SiOH$ [93]. At higher

78

temperatures these surface species decomposed further. Secondary ion mass spectroscopy experiments suggest that the $\pi - Si$ surface composition changes due to hydrolysis of $Si - F$ bonds by water vapour [94]. Room temperature oxidation then proceeds via rupture of Si backbonds without breaking the hydride bonds of the pore wall surface. In the PL study of Maruyama and Ohtani [95], it is claimed that water vapour in ambient air gradually oxidized the surface of $\pi - Si$ through the formation of $Si - O - Si$ bonds. This room temperature oxidation progressively replaced the H-passivated surface with a more stable O-passivated surface. While all these reaction schemes are different, it is clear that they all prevent accumulation of H_2O on the $\pi - Si$ surface and this may partially explain why the pre- and post-treatment SAW velocities were the same.

5.1.2 Elastic Constants

The elastic constants of the porous layers are, in all cases, much lower than those of $c - Si$ (see Table 4.11). This is due to a combination of reduced density and reduced acoustic velocity compared to $c - Si$. The porosity dependence of the elastic constants of samples #1-#4 of set II and 543 and 557 of set III is shown in Figure 5.1. The error bars are approximately the same size as the symbols. As might be expected, the elastic constants of samples from a given set decrease with increasing porosity. While $\pi - Si$ appears to be unique in the sense that it is a porous material formed from a crystalline solid, other studies on ceramics and sintered materials show similar behaviour. For instance, experimental data from several ceramics such as alumina, silicon nitride, uranium oxide, rare-earth oxides and $YBa_2Cu_3O_{7-\delta}$ all have Young's modulus values which decrease with increasing porosity [96].

The only other $\pi - Si$ elastic constants available for comparison were those determined by Yamanaka *et al.* [58-60] using the technique of phase velocity scanning of interference fringes. In two papers by this group [59, 60], excellent agreement between measured and
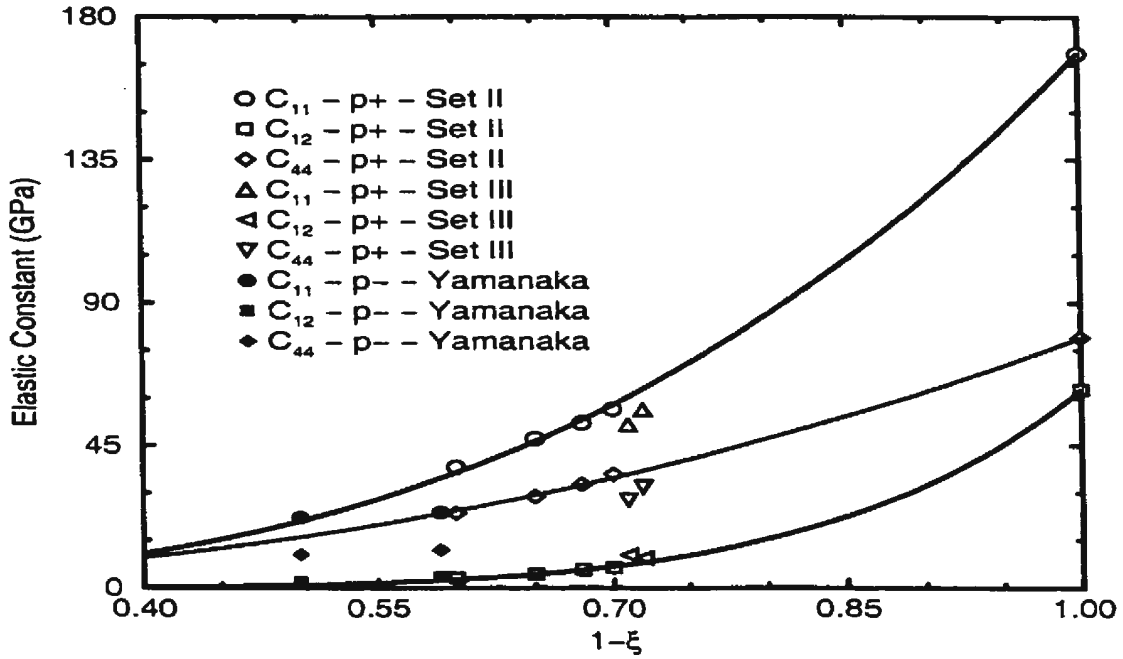
Figure 5.1: Elastic constants of $\pi - Si$ prepared from p^- and p^+ type $c - Si$. The open symbols correspond to elastic constants of p^+ samples from Sets II and III of the present study. The solid symbols are the elastic constants of p^- type $\pi - Si$ determined by phase velocity scanning of interference fringes. The solid lines are fits to expressions of the form $C_{ij}^{\pi - Si} = C_{ij}^{c - Si}(1 - \xi)^{m_{ij}}$.

calculated SAW velocity dispersion curves was obtained by assuming that the elastic constants of the $\pi - Si$ layers formed from p^- type $c - Si$ were $x\%$ (x ranged from 3.8 to 12) those of $c - Si$. This assumption, for which no physical basis was provided, implies that the porous layers have the same anisotropy factor and Poisson's ratio as $c - Si$. It also implies that Young's modulus is greater for $\pi - Si$ than for $c - Si$. This is not consistent with the results of the present work where all three parameters (η, σ and E) were found to be significantly smaller than the corresponding $c - Si$ values. In fact, Poisson's ratio and Young's modulus reach values as low as $\sim 25\%$ those of $c - Si$ (see Table 4.12). A reduction in elastic anisotropy, while not as dramatic (reaching a low

80

Table 5.1: Complete sets of elastic constants for both p^- and p^+ type $\pi - Si$ layers of various porosities.

Sample	Type	Porosity (%)	C_{11} (GPa)	C_{12} (GPa)	C_{44} (GPa)	E [100] (GPa)	η	σ
p-Si #1	p^+	30	56.4	6.4	35.9	70.9	1.44	0.102
p-Si #2	p^+	32	52.1	5.8	32.7	64.8	1.41	0.100
p-Si #3	p^+	35	47.2	4.3	28.9	57.1	1.35	0.083
p-Si #4	p^+	40	38.1	3.0	23.5	46.0	1.34	0.073
p-Si 543	p^+	28	56.3	9.5	32.0	67.4	1.37	0.144
p-Si 557	p^+	29	51.5	10.4	27.8	60.2	1.35	0.168
Yamanaka	p^-	41	23.8	3.42	11.9	25.7	1.16	0.126
Yamanaka	p^-	50	22.2	1.89	10.5	22.4	1.04	0.078

of $\sim$ 85% that of $c - Si$), is also clearly observed. The results of other experiments on $\pi - Si$ show behaviour similar to that observed in the present work. For example, a Poisson's ratio of 0.09 was obtained for a p^+ type $\pi - Si$ layer with a porosity of 54% in the X-ray diffraction study of Barla et al. [22]. Reduced Young's modulus values (compared to $c - Si$) for $\pi - Si$ layers of various porosities have also been observed in X-ray diffraction [22], acoustic microscopy [53] and nanoindentation experiments [55]. This will be discussed in greater detail later in this section.

In a more recent work by Yamanaka [58], elastic constants of two $\pi - Si$ layers fabricated from p- type $c - Si$ substrates were evaluated in a more quantitative fashion by applying an inverse analysis to SAW velocity dispersion and anisotropy data. These values are tabulated in Table 5.1 and plotted in Figure 5.1 along with those for samples of the present study. The elastic anisotropy, Poisson's ratio and Young's modulus calculated from the elastic constants are also given in the table.

The elastic constants obtained for the p^+ samples by Brillouin scattering and those for p^- type samples by phase velocity scanning of interference fringes have some features

in common. For instance, while only two $\pi - Si$ samples fabricated from p^- type Si were studied, the general behaviour of the elastic constants appears to be the same as for samples formed from the p^+ type substrates, *i.e.*, they decrease with increasing porosity (for samples of a given set). From Table 5.1, it can also be seen that for both the p^- and p^+ type layers, elastic constant C_{12} is reduced from its nonporous ($c - Si$) value by a factor which is larger than the corresponding factor for C_{11} or C_{44}. In addition, the anisotropy factor and Young's modulus also decrease with increasing porosity for the p^- type layers as well as for the p^+ layers from Sets II and III.

It is particularly interesting to compare the elastic constants of the 41% porous p^- layer to those of the 40% porous p^+ layer (#4) because their porosities are nearly equal. It is clear (Table 5.1) that the elastic constants of these two samples are quite different. C_{11} and C_{44} for the p^+ layer are much larger (by factors of approximately 1.6 and 2.0, respectively) than the corresponding constants for the p^- layer, while C_{12} is about 15% larger for the p^- type layer. Given the relatively small difference in porosity, these differences are probably artefacts of the distinct microstructures formed during anodization of p^- and p^+ type $c - Si$ substrates. As discussed in Chapter 1, $\pi - Si$ formed from p^- type $c - Si$ substrates typically consists of an interconnected random pore network with characteristic pore diameters and interpore spacings in the range 1 nm-5 nm. In contrast, $\pi - Si$ fabricated from p^+ type starting material exhibits channel formation and significant sidebranching with typical pore diameters and interpore spacings between 5 nm and 15 nm. This hypothesis is supported by the results of nanoindentation experiments on p^- and p^+ type $\pi - Si$ ($\xi = 70\%$) where a large difference was seen between the Young's modulus of the two samples (Young's modulus of the p^- type sample was smaller than that of the p^+ type sample by a factor of 5). In fact, many other studies on a wide variety of materials confirm that elastic moduli are very sensitive to microstructure [97, 98].

The effect of microstructure on the elastic properties of $\pi - Si$ may be investigated in greater detail by examining the porosity dependence of the elastic constants of layers formed from p^- and p^+ type substrates (see Figure 5.1). Yamanaka $et\ al.$ [58] fitted expressions of the form

$$C_{ij}^{\pi-Si} = C_{ij}^{c-Si}(1 - \xi)^{m_{ij}}, \quad ij \equiv 11,\ 12,\ 44,\quad\quad (5.1)$$

to their experimental data. Here, $C_{ij}^{\pi-Si}$ (C_{ij}^{c-Si}) is one of the three elastic constants of $\pi-Si$ $(c-Si)$, ξ is the sample porosity and m_{ij} is a dimensionless constant corresponding to elastic constant $C_{ij}^{\pi-Si}$. Since $\pi - Si$ formed from both p^- and p^+ type substrates have essentially the same zero-porosity elastic constants (ignoring doping effects), any differences in the m_{ij} between p^- and p^+ type layers (or even between sets of p^+ or p^- layers) must be due to microstructural differences. This type of fitting, therefore, provides some insight into the influence of microstructure on the elastic constants.

The values of the m_{ij} obtained for the p^- type samples are given in Table 5.2 along with those obtained from the porosity dependence of the elastic constants of p^+ samples from Set II of the present work. Explicitly, for Set II, the corresponding equations are

$$
\begin{aligned}
C_{11}^{\pi-Si} &= 168.5(1 - \xi)^{3.00} \\
C_{12}^{\pi-Si} &= 62.6(1 - \xi)^{6.23} \\
C_{44}^{\pi-Si} &= 79.0(1 - \xi)^{2.30}.
\end{aligned}
\quad\quad (5.2)
$$

While the values of m_{11}, m_{12} and m_{44} are of the same order of magnitude for both sets of samples, significant differences are evident. The values of m_{11} and m_{44} obtained for the p^+ type samples are $\sim 10\%$ and $\sim 30\%$ lower than the corresponding values for $\pi - Si$ fabricated from the p^- type layers, respectively. On the contrary, m_{12} for the p^+ samples is $\sim 15\%$ larger than m_{12} for the p^- samples. This means that for any fixed porosity, the elastic constants $C_{11}^{\pi-Si}$ and $C_{44}^{\pi-Si}$ for a p^+ sample will be larger than those of a sample formed from p^- type $c - Si$. On the other hand, $C_{12}^{\pi-Si}$ for a p^+ type sample

Table 5.2: Exponents m_{ij} obtained from fitting elastic constant data from set II to functions of the form $C_{ij}^{\pi-Si} = C_{ij}^{c-Si}(1 - \xi)^{m_{ij}}$. Also shown are values obtained by Yamanaka et al..

Set	m_{11}	m_{12}	m_{44}
II	3.00 ± 0.03	6.23 ± 0.17	2.30 ± 0.06
Yamanaka	3.34	5.42	3.31

will be smaller than $C_{12}^{\pi-Si}$ of a p^- type sample. It is also interesting to note that for both the p^- and p^+ type layers, elastic constant C_{12} decreases much more rapidly with increasing porosity than C_{11} or C_{44}. The reason for this is unknown.

The values of m_{11}, m_{12} and m_{44} obtained for $\pi - Si$ samples formed from p^- type $c - Si$ by Yamanaka et al. [58] led them to conclude that the microstructure of this kind of $\pi - Si$ is intermediate between a relatively ordered and isolated pore structure and a disordered and interconnected pore structure. This conclusion was based on the results of an ultrasonic study of the strength and elastic modulus of a porous brittle solid (gypsum) [99]. Examination of the porosity dependence of Young's modulus of gypsum revealed that fitting expressions of the form $E = E_o(1 - \xi)^m$ to experimental data resulted in very different values of m for gypsum samples which exhibited different microstructures (as seen in electron micrographs). Gypsum which showed intergrowth and interlinking of crystals gave a value of m around 3.2, whereas samples consisting of fragmented and shorter crystals with interconnected pores gave a much higher value of m (> 9.5).

The difference in microstructure also appears to manifest itself in the elastic anisotropy. It is evident form Table 5.1 that the anisotropy factor of the 41% p^- type layer is approximately 13% lower than that of the 40% porous p^+ type layer. This suggests that the p^- type layer is much more elastically isotropic than the p^+ type layer of similar

84

porosity. This might be due to the extremely small crystal size and random nature of the pore network of the p^- type samples.

As alluded to earlier in this section, there are some studies in which Young's modulus has been determined for $\pi - Si$ samples of various porosities and initial substrate dopant concentrations. The first of these was the X-ray diffraction study of Barla et al. [22]. They showed that a difference in lattice parameter exists between $\pi - Si$ and $c - Si$ and that this mismatch induces wafer curvature. The lattice mismatch and curvature were related by an equation involving Young's modulus of the layer and the substrate. It was shown that Young's modulus for a 54% layer (formed from p^+ type $c - Si$) is smaller than that for $c - Si$ by a factor of ten. Estimates were also obtained for layers with porosities of 34% and 72% by assuming that Poisson's ratio for these samples was the same as for the sample with $\xi = 54\%$.

Microacoustic techniques have been used by DaFonseca et al. [53] to measure both surface and longitudinal acoustic wave velocities in low porosity $\pi - Si$ layers formed from p^+ type substrates. Young's modulus was calculated from these velocities and was found to decrease with increasing porosity. The expression $E^{\pi - Si} = A\rho^{\pi - Si}(V_L^{\pi - Si})^2$ was fitted to the experimental data (see Figure 5.2). Here, A is a parameter which depends on the $\pi - Si$ shear and longitudinal acoustic wave velocities (which, in turn, depend on the porosity), $\rho^{\pi - Si}$ is the density of $\pi - Si$ and $V_L^{\pi - Si}$ is the $\pi - Si$ longitudinal acoustic wave velocity.

Bellet et al. [55] used nanoindentation techniques to determine Young's modulus for p^+ type $\pi - Si$ layers over a range of porosities from 36% to 90%. These values were compared to those predicted by a model developed for open-celled materials [56]. In this model, the Young's modulus of the porous solid, E_p is related to the that of the corresponding bulk material (E) according to $E_p = CE(1 - \xi)^2$, where $C \sim 1$ (see Figure 5.2). By fitting this expression to their experimental data, they obtained
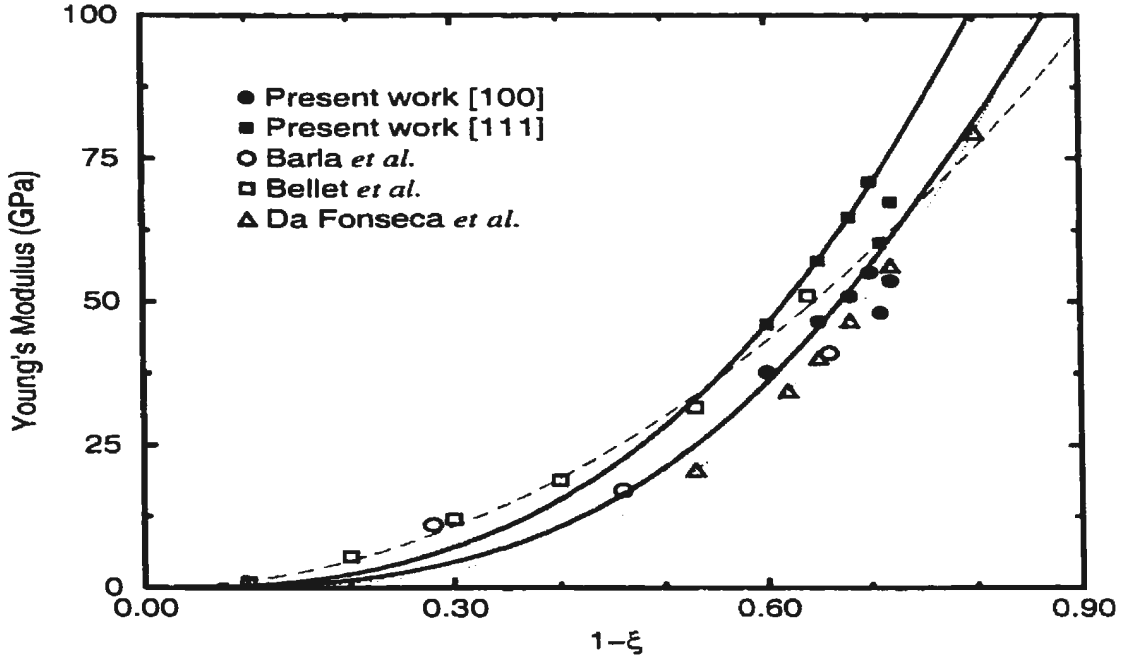
Figure 5.2: Young's modulus of $\pi - Si$ formed from p^+ type $c - Si$ substrates. The dotted curve is the best-fit obtained by DaFonseca et $al.$ using the expression $E^{\pi-Si} = A\rho^{\pi-Si}(V_L^{\pi-Si})^2$. The dashed curve is the best-fit obtained by Bellet et $al.$ assuming that $\pi - Si$ can be treated as an open cell foam ($E^{\pi-Si} = E^{c-Si}(1-\xi)^2$). The solid curves were obtained by substituting elastic constant expressions 5.2 into equation 2.26 for the [100] and [111] directions.

reasonable agreement between theory and experiment (see Figure 5.2).

Unfortunately, neither of the above models take into account the effects of elastic anisotropy even though, as pointed out in an earlier section, $\pi - Si$ is anisotropic. In fact, no previous studies of $\pi - Si$ account for the anisotropy when determining the Young's modulus. If the anisotropy of $\pi - Si$ is taken into account, Young's modulus depends on the direction in the solid under consideration. For cubic crystals, E has extremum values in the directions of the crystal axes ([100]) and along the cube diagonals ([111]). Substituting the empirical expressions for the elastic constants given above (equation 5.2)

86

into equation 2.26, Young's modulus was calculated as a function of $1 - \xi$ in the [100] and [111] directions. These curves are given in Figure 5.2 along with data from this experiment and several other experiments in which Young's modulus of various $\pi - Si$ layers was calculated assuming acoustic isotropy.

It should also be noted that the cellular solid model does not account for the influence of microstructure on the elastic properties. As can be seen in figure 5.2, significant differences in Young's modulus exist even among samples formed from p^+ type $c - Si$ substrates. Any theory attempting to accurately describe the elastic properties of $\pi - Si$ must, therefore, consider the influence of the geometry of the Si skeleton.

5.2 Structural Properties of $\pi - Si$

5.2.1 Morphology and the First-Order Raman Spectrum of $\pi - Si$

There are differences between the first-order Raman spectra collected from $\pi - Si$ samples formed from p^- and p^+ type $c - Si$. The spectra of the p^- samples have lower Raman shifts and larger linewidths than the p^+ type samples of similar porosity. Similar results have been observed in other Raman scattering experiments on $\pi - Si$ prepared from substrates with different resistivities. For example, Munder *et al.* [29] present very different Raman spectra for p^- and p^+ layers, both with porosity of 65%. The Raman shifts of the first-order peak were ~ 519 cm^{-1} and ~ 516 cm^{-1} for the p^+ and p^- layers, respectively. The corresponding $FHWM$ were ~ 6 cm^{-1} and ~ 18 cm^{-1} (for the p^+ and p^- layers, respectively). The results for the p^+ layer are in very good agreement with those of the present work for the p^+ type layer with $\xi = 65\%$ ($FWHM = 8.3$ cm^{-1} and $\omega = 519$ cm^{-1}). Kozlowski and Lang [28] also obtained qualitatively distinct spectra for p^- type layers formed from Si of resistivity 0.2 Ω·cm and $1 - 15$ Ω·cm. The 0.2 Ω·cm samples had Raman shifts between 518.5 cm^{-1} and 519.5 cm^{-1} and $FWHM = 4 - 10$ cm^{-1}.

87

These values are very similar to those obtained for samples C and E of the present work (see Table 4.16). The higher resistivity samples had Raman shifts of 510.5 cm^{-1}- 513.5 cm^{-1} and $FWHM$ in the range 28-44 cm^{-1}. The first-order Raman peak of sample B (p^- type substrate, $R = 10$ Ω·cm, $\xi = 80\%$) has a Raman shift and $FWHM$ quite similar to that of the high resistivity samples ($\omega^{\pi-Si} = 513.9$ cm^{-1}, $FWHM = 24.3$ cm^{-1}).

At first glance, the Raman spectrum of sample D ($\xi = 80\%$) appears to contradict the above argument. The first-order Raman peak is located at a shift of 514.7 cm^{-1} and has a $FWHM$ of ~ 20 cm^{-1}. These values are larger than the typical ones for $\pi - Si$ prepared from p^+ type substrates and, in fact, are quite similar to those of sample B, fabricated on a p^- type substrate. The Raman peak has a smaller Raman shift and its width is much greater than for the p^+ samples of lower porosity. From a microscopic point of view, this probably corresponds to a change of the dominant nanocrystallite type from wire-like to sphere-like. This may be explained by a widening of the channels in p^+ type material as a result of the increase in anodization current density when producing highly porous Si. In such a case, a local breaking of the columnar skeleton is expected which, in turn, creates isolated Si grains.

The differences in first-order Raman spectra observed on $\pi - Si$ formed from substrates of different resistivities may be explained by morphological differences between the samples (spherical and wire-like for p^- and p^+ type samples, respectively). The p^+ type Raman spectrum of Munder et al. [29] could be accurately reproduced by assuming a distribution of nanocrystallite sizes ranging from 2 nm to 15 nm as well as an amorphous background. The nanocrystal size distribution required to accurately reproduce the p^- spectrum required diameters smaller than 3.5 nm.

The phonon confinement model was found to describe the Raman spectra reasonably well (to a first approximation) and permitted estimation of the predominant nanocrystallite size present in the samples. However, some discrepancies exist between the calculated

and experimental spectra (see Figures 4.11 and 4.12). The most obvious of these is the extended tail at low Raman shifts in some of the experimental spectra (particularly noticeable in the spectra collected from samples B, D and E). Simulations show that this tail can be attributed to contributions to the spectrum from crystallites of very small average diameters. This implies, as might be expected, that a distribution of crystallite sizes exists in any given $\pi - Si$ sample. No evidence for an amorphous phase of Si was observed in the present work (*i.e.*, no peak at a Raman shift of ~ 480 cm^{-1}). There are some studies, however, which report the existence of an amorphous phase in $\pi - Si$. In particular, Gregora *et al.* [31] noticed a pronounced shoulder in the Raman spectra of their samples prepared from p^- type Si . This feature was located at a shift of 478 ± 2 cm^{-1} and was said to be an "amorphous-like" contribution to the spectrum.

The nanocrystallite sizes obtained for the samples from Set I are presented in Table 4.16. The p^+ samples of the present work show a trend of decreasing crystallite size with increasing porosity. This is in agreement with the general observation that as porosity increases, the pore size also increases, resulting in a decrease in average nanocrystallite size. Another interesting point to note is that the characteristic nanocrystallite size for sample B (formed from a p^- type substrate) is smaller than that of sample D (formed from a p^+ type substrate) even though both samples have a porosity of 80%. Thus, it appears that the differences in first-order Raman spectra observed on $\pi - Si$ formed from substrates of different resistivities may be explained by morphological differences between the samples. As mentioned earlier, typical crystallite sizes for $\pi - Si$ prepared from p^- type material are < 5 nm. For $\pi - Si$ fabricated from p^+ type $c - Si$, crystallite sizes are usually ~ 10 nm.

It is important to note that in the determination of nanocrystallite size above, the effect of strain (known to exist in $\pi - Si$ layers) on the first-order Raman spectrum was neglected. This is because the strain-induced shifts of the Raman peaks for the samples of

89

Table 5.3: Nanocrystallite sizes calculated using the phonon confinement model for $\pi - Si$ layers formed from both p^- and p^+ type $c - Si$ substrates.

Reference	Type	ξ (%)	ρ (Ω·cm)	$\Delta\omega$ (cm^{-1})	Γ (cm^{-1})	L (nm)
Present work	p^+	35	0.005	519.5	10.0	16.0 (w)
	p^+	65	0.03	518.9	8.3	9.5 (w)
	p^+	80	0.03	514.7	19.9	5.2 (s)
	p^-	80	10	513.9	24.3	4.6 (s)
Gregora et al. [31]	p^+	70	0.01	517-518	6-8	4-5 (w) 6-8 (s)
	p^-	70	1	509-514	15-30	2.6-3.9 (w)
Sui et al. [27]	p^-	—	150	508.0-510.1	32-40	2.5-3.0

the present work were not known. However, X-ray diffraction [29] data show that strain reduces the Raman shift of the first-order peak for p^+ and p^- type samples ($\xi = 65\%$) by ~ 0.5 cm^{-1} and ~ 3 cm^{-1}, respectively. If similar strain-induced shifts occur in the Raman spectra of the p^+ and p^- samples of the present study then the characteristic sizes reported in Table 5.3 are too small (i.e., the actual crystallite sizes are larger than those given in Table 5.3).

The results of two other Raman scattering experiments [27, 31] are presented in Table 5.3. As is evident, the overall agreement with the results of the present study is quite good. In general, the nanocrystallites found in the p^- type samples are smaller than those found in p^+ type samples of the same porosity. In addition, the shape of the crystallites in p^- type samples is spherical whereas it is wire-like in the p^+ samples.

5.2.2 Changes in Microstructure with Depth

The increase in Raman shift and concomitant reduction in width for the first-order $\pi - Si$ Raman peak of sample D (formed from p^+ type $c - Si$) excited with a laser excitation

90

wavelength of 514.5 nm compared to the 488.0 nm excited spectrum clearly indicate an increase in nanocrystallite size with increasing depth from the sample surface. This is in agreement with the results of Guha *et al.* [46] who investigated the excitation wavelength dependence of the first-order Raman spectrum of $\pi - Si$ samples ($\xi = 70\%$) formed from p^- type $c - Si$ substrates. As above, the Raman linewidth decreased and the shift increased with increasing excitation wavelength (458 nm, 488 nm and 514.5 nm). Using the phonon confinement model, they fitted theoretical spectra to their experimental spectra and noted an increase in crystallite size with increasing wavelength. This was attributed to a distribution of nanocrystallite sizes in a porous layer. Similar experiments were carried out by Zhang *et al.* [45] on p^- type samples of unspecified porosity using incident laser wavelengths from the violet to the near infrared. They found that the Raman shift tends towards that of $c - Si$ and the linewidth narrows as the excitation wavelength increased. This was attributed to a decrease in average pore size and porosity with increasing depth from the layer surface. This conclusion is also consistent with the results of the present work since it implies an increase in crystallite size with increasing depth.

Analogous structural information has been obtained using single-wavelength micro-Raman scattering to probe different depths on cleaved $\pi - Si$ layer cross-sections (as opposed to the top of the layer). Mariotto *et al.* [43] used this method to obtain spectra from air-stored samples of low porosity fabricated from p^- type substrates. The depth dependence of the nanocrystallite size was analyzed using a phenomenological model based on the spatial confinement of phonons. Considerable reduction of the crystallite size was found from the analysis of the spectra excited at the $\pi - Si$ /vacuum interface. Their results also indicate that an $\alpha - Si$ component is present at all depths within the porous layer. In contrast, no evidence for an amorphous phase was observed in the present experiments. As mentioned in the preceding section, the Raman spectra of the

present work are reasonably well described by the phonon confinement model which does not include any amorphous contribution to the scattering. The variation in crystallite size with depth in highly porous layers ($\xi = 75\%$) formed from p^- type substrates has also been studied using micro-Raman scattering techniques [44]. Using the phonon confinement model, with the assumption of spherical grains, crystallite sizes of 4.6 nm and 3.6 nm were deduced from spectra collected from a region in the porous layer near the $\pi - Si$ /substrate interface and the $\pi - Si$ /vacuum interface, respectively. The smaller crystallite size near the surface was said to be due to extra chemical dissolution of the already formed layer. In addition, no Raman peak was observed at a shift of 480 cm^{-1}, indicating no substantial contribution from an $\alpha - Si$ phase. Micro-Raman scattering experiments [26] on cleaved cross-sections of $\pi - Si$ films produced from n^- type starting wafers show similar trends in first-order Raman peak shift and linewidth, including the reduction in the Raman shift of the peak near the layer surface. These observations were interpreted as being due to a continual decrease in crystallite size as the depth from the surface decreased. Near the sample surface the Raman results suggest that the characteristic size is less than a few nanometres.

It is particularly relevant to compare the results of the Raman scattering studies of Thonissen *et al.* [48] with those of the present study because the $\pi - Si$ layers involved were formed from similarly-doped substrates (p^+ type). Their results indicate that the gradient in microstructure for p^+ type samples changes from large crystallites at the surface to smaller ones at the $\pi - Si$ /substrate interface. This was attributed to a decrease in the HF concentration with depth which occurs at high anodization current densities (250 mA·cm^{-2} in this case). Such a trend is at variance with the results of the present study. It is generally true, however, that a decrease in HF concentration causes an increase in characteristic pore size. This may be interpreted as a decrease in crystallite size and hence this could explain the different trends in crystallite size between

the two studies. It should also be noted that the sample (D) used in the present study was produced using a current density of 15 mA·cm^{-2} which is approximately a factor of 17 smaller than the value above making the difference in HF concentration from the top to the bottom of the layer much smaller. In any case, the existence of a nanocrystallite size gradient complicates the estimation of an average crystallite size for a given layer using the phonon confinement model since the size deduced depends on the Raman peak position and the linewidth which, in turn, depend on the penetration depth of the incident light.

5.2.3 Nanocrystallite Size and Photoluminescence

Referring to Table 4.16, the general trend for samples prepared from the p^+ type Si (C,D and E) is in accord with the results expected for the quantum confinement origin of PL, $i.e.$, a lower PL peak energy and a PL intensity which increases with increasing porosity. The maxima of the PL spectra, however, are at much higher photon energies than those calculated from the quantum confinement theory [100] using L values estimated for the same samples from Raman scattering (see Table 5.4). In the case of sample D, a calculated optical band gap energy of $\sim$ 1.5 eV corresponds to spherical crystallites having an average diameter of 4.7 nm. A weak shoulder observed around this energy (see Figure 4.13) correlates with the above band gap. A large variation in nanocrystallite size for sample D, which is expected from the Raman spectrum in Figure 4.12, is consistent with the greater width of the corresponding PL spectrum, as compared to the others. One cannot assume, however, that a quantum confinement mechanism is sufficient to explain all the PL spectra, even when taking into account larger contributions to the PL from smaller crystallites. There are probably other effects, mostly of surface origin, that are also important [21, 32]. A good example is sample C, of 65% porosity, which showed a moderately broad PL band at 1.63 eV (Figure 4.13). The optical band gap energy, which

93

Table 5.4: Experimental and theoretical (based on quantum confinement model) PL peak energies for p^- and p^+ type $\pi - Si$ layers of Set I.

Sample	Type	Porosity (%)	L (nm)	Experimental PL (eV)	Theoretical PL (eV)
A	p^-	80	—	1.69	—
B	p^-	80	4.6 s	1.78	1.56
C	p^+	65	9.5 w	1.63	1.18
D	p^+	80	5.2 s	1.67	1.19
E	p^+	35	16.0 w	1.60	1.15

corresponds to a quantum wire of diameter 9.5 nm, is $\sim$ 1.18 eV [100], $i.e.$, beyond the accessible spectral region of the present experiment. Therefore, the PL band of sample C at 1.63 eV, as well as that of E cannot be due to quantum confinement effects in wires of the estimated sizes. Also, since the Raman band of sample C is well described by the phonon confinement model (indicating a narrow range of crystallite sizes), no significant contribution from finer crystallites is expected. On the contrary, for sample E of 35% porosity, the Raman spectrum shows a tail at low Raman shifts which may be attributed to an admixture of the smallest (spherical) nanocrystallites with a continuous broad distribution extending to about 3 nm. Although it might be surprising in the case of such low porosities, this observation is supported by earlier investigations performed also on p^+ type samples [29]. Because of its weak intensity it is difficult to investigate the PL spectrum of sample E in greater detail. The PL peak energy of 1.60 eV, however, cannot be explained by spheres or wires with diameters consistent with the Raman spectrum.

5.3 Conclusions

Brillouin light scattering spectroscopy has been used to investigate the elastic properties of (111)-oriented $\pi - Si$ samples formed from p^- and p^+ type $c - Si$ substrates. In

the frequency regime studied, Brillouin spectra of the low porosity p^+ samples consist only of a single set of inelastic peaks due to the surface acoustic wave. The velocities of these waves were found to be significantly lower than the corresponding $c - Si$ velocity, and, for samples of a given set, decreased with increasing porosity. Removal of the thin native oxide film present on low porosity p^+ type samples by an HF dip, results in a 3%-6% decrease in SAW velocity compared to pre-dip values. Adsorbed water on the $\pi - Si$ surface appears to have no measurable effect on the SAW velocity.

Complete sets of elastic constants for several low porosity layers formed from p^+ type substrates were determined from the directional dependence of the SAW velocity in the (111) plane. The elastic constants were found to be much smaller than those for $c-Si$ and, for a given set, decreased with increasing porosity. Empirical fitting of expressions of the form $C_{ij}^{\pi-Si} = C_{ij}^{c-Si}(1-\xi)^{m_{ij}}$ to the experimental data leads to the following relations for the porosity dependence of the elastic constants:

$$\begin{aligned}
C_{11}^{\pi-Si} &= 168.5(1-\xi)^{3.00} \\
C_{12}^{\pi-Si} &= 62.6(1-\xi)^{6.23} \\
C_{44}^{\pi-Si} &= 79.0(1-\xi)^{2.30}.
\end{aligned} \qquad (5.3)$$

The exponents m_{11}, m_{12} and m_{44} differ from those of porous samples formed from p^- type substrates. This is attributed to microstructural differences between porous layers formed from p^- and p^+ type substrates. In addition, Young's modulus values were calculated and compared to those determined in other experiments. In contrast to other studies, elastic anisotropy is taken into account.

A limited number of Brillouin spectra were also obtained from intermediate porosity samples fabricated from p^- type substrates. These spectra exhibited multiple broad Brillouin peaks at relatively low frequency shifts (< 15 GHz) and are qualitatively similar to those collected by Beghi *et al.* [51] from samples with similar porosity formed from p^- type substrates.

Raman scattering has been used to study the structural and light-emitting properties of $\pi - Si$ layers formed from p^- and p^+ type (111)-oriented $c - Si$ substrates. An analysis of the Raman lineshapes was performed using a phonon confinement model with realistic longitudinal and transverse optic phonon dispersion curves. Characteristic nanocrystallite sizes and shapes were determined for samples with porosities in the range 35% to 80%. The highly porous samples consist of fine Si spheres, while those of lower porosity are primarily wire-like. The photoluminescence spectra are less size-sensitive than the Raman spectra and no clear correlation between the Raman scattering structural information and the photoluminescence spectra has been observed.

Bibliography

[1] A. Uhlir, Bell Syst. Tech. J. **35**, 333 (1956).

[2] D.R. Turner, J. Electrochem. Soc. **105**, 402 (1958).

[3] Y. Watanabe, Y. Arita, T. Yokoyama, and Y. Igarashi, J. Electrochem. Soc. **122**, 1351 (1975).

[4] M.J.J. Theunissen, J. Electrochem. Soc. **119**, 351 (1972).

[5] M.I.J. Beale, N.G. Chew, M.J. Uren, A.G. Cullis, and J.D. Benjamin. Appl. Phys. Lett. **46**, 86 (1985).

[6] H. Unno, K. Imai, and S. Muramoto, J. Electrochem. Soc. **134**, 645 (1987).

[7] R. Herino, G. Bomchil, K. Barla, C. Bertrand, and J.L. Ginoux, J. Electrochem. Soc. **134**, 1994 (1987).

[8] G. Bomchil, R. Herino, K. Barla, and J.C. Pfister, J. Electrochem. Soc. **130**, 1611 (1983).

[9] K. Imai, Solid State Elec. **24**, 159 (1981).

[10] T. Unagami and K. Kato, Jpn. J. Appl. Phys. **16**, 1635 (1977).

[11] C. Pickering, M.I.J. Beale, D.J. Robbins, P.J. Pearson, and R. Greef, J. Phys. C **17**, 6535 (1984).

[12] L.T. Canham, Appl. Phys. Lett. **57**, 1046 (1990).

[13] V. Lehmann and U. Gosele, Appl. Phys. Lett. **58**, 856 (1991).

[14] P. Menna, G. DiFrancia, and V. LaFerrara, Solar Energy Materials and Solar Cells **37**, 13 (1995).

[15] L.T. Canham, J.P. Newey, C.L. Reeves, M.R. Houlton, A. Loni, A.J. Simons, and T.I. Cox, Adv. Mater. **8**, 847 (1996).

[16] M. Thust, M.J. Schoning, S. Frohnhoff, R. Arens-Fischer, P. Kordos, and H. Luth, Measurement Science and Technology **7**, 26 (1996).

[17] R.T. Collins, P.M. Fauchet, and M.A. Tischler, Physics Today **50**, 24 (1997).

[18] L. Brus, J. Phys. Chem. **98**, 3575 (1994).

[19] A.G. Cullis, L.T. Canham, and P.D.J. Calcott, J. Appl. Phys. **82**, 909 (1997).

[20] R.L. Smith and S.D. Collins, J. Appl. Phys. **71**, R1 (1992).

[21] G.C. John and V.A. Singh, Physics Reports **263**, 93 (1995).

[22] K. Barla, R. Herino, G. Bomchil, J.C. Pfister, and A. Freund, J. Cryst. Growth **68**, 727 (1984).

[23] B. Hamilton, Semicon. Sci. Technol. **10**, 1187 (1995).

[24] P.C. Searson and J.M. Macaulay, Nanotechnology **3**, 188 (1992).

[25] L.T. Canham, A.G. Cullis, C. Pickering, O.D. Dosser, T.I. Cox, and T.P. Lynch, Nature **368**, 133 (1994).

[26] K. Inoue, O. Matsuda, K. Maehashi, H. Nakashima, and K. Murase, Jpn. J. Appl. Phys. **31**, L997 (1992).

[27] Z. Sui, P.P. Leong, I.P. Herman, G.S. Higashi, and H. Temkin, Appl. Phys. Lett. **60**, 2086 (1992).

[28] F. Kozlowski and W. Lang, J. Appl. Phys. **72**, 5401 (1992).

[29] H. Munder, C. Andrzejak, M.G. Berger, U. Klemradt, and H. Luth, Thin Solid Films **221**, 27 (1992).

[30] I. Gregora, B. Champagnon, L. Saviot, and Y. Monin, Thin Solid Films **255**, 139 (1995).

[31] I. Gregora, B. Champagnon, and A. Halimaoui, J. Appl. Phys. **75**, 3034 (1994).

[32] Y. Kanemitsu, H. Uto, Y. Masumoto, T. Matsumoto, T. Futagi, and H. Mimura, Phys. Rev. B **48**, 2827 (1993).

[33] M. Yang, D. Huang, P. Hao, F. Zhang, X. Hou, and X. Wang, J. Appl. Phys. **75**, 651 (1994).

[34] D.J. Lockwood, Solid State Commun. **92**, 101 (1994).

[35] R. Tsu, H. Shen, and M. Dutta, Appl. Phys. Lett. **60**, 112 (1992).

[36] X.L. Wu, F. Yan, M.S. Zhang, and D. Feng, Phys. Lett. A **205**, 117 (1995).

[37] H.J. Lee, Y.H. Seo, D.H. Oh, K.S. Nahm, E.K. Suh, Y.H. Lee, H.J. Lee, Y.G. Hwang, K.H. Park, S.H. Chang, and E.H. Lee, Appl. Phys. Lett. **62**, 855 (1993).

[38] A.K. Sood, K. Jayaram, and D.V.S. Muthu, J. Appl. Phys. **72**, 4963 (1992).

[39] H. Richter, Z.P. Wang, and L. Ley, Solid State Commun. **39**, 625 (1981).

[40] I.H. Campbell and P.M. Fauchet, Solid State Commun. **58**, 739 (1986).

[41] P.M. Fauchet and I.H. Campbell, Mater. Res. Soc. Symp. Proc. **164**, 259 (1990).

[42] P.M. Fauchet and I.H. Campbell, Crit. Rev. Solid State and Mater. Sciences **14**, S79 (1988).

[43] G. Mariotto, F. Ziglio, and F.L. Freire, J. Non-Cryst. Solids **192&193**, 253 (1995).

[44] Y. Monin. L. Saviot. B. Champagnon. C. Esnouf. and A. Halimaoui. Thin Solid Films **255**, 188 (1995).

[45] S.L. Zhang, Y. Hou. K.S. Ho, B. Qian, and S. Cai. J. Appl. Phys. **72**, 4469 (1992).

[46] S. Guha, P. Steiner, F. Kozlowski, and W. Lang, Thin Solid Films **276**, 73 (1996).

[47] S. Guha, P. Steiner, and W. Lang, J. Appl. Phys. **79**, 8664 (1996).

[48] M. Thonissen, S. Billat, M. Kruger, H. Luth, M.G. Berger, U. Frotscher, and U. Rossow, J. Appl. Phys. **80**, 2990 (1996).

[49] D.J. Lockwood and A.G. Wang, Solid State Commun. **94**, 905 (1995).

[50] P. Deak, Z. Hajnal, M. Stutzmann, and H.D. Fuchs, Thin Solid Films **255**, 241 (1995).

[51] M.G. Beghi, C.E. Bottani, G. Ghislotti, G. Amato, and L. Boarino, Thin Solid Films **297**, 110 (1997).

[52] R.J.M. da Fonseca, J.M. Saurel, A. Foucaran, E. Massone, T. Taliercio, and J. Camassel, Thin Solid Films **255**, 155 (1995).

[53] R.J.M. da Fonseca, J.M. Saurel, A. Foucaran, J. Camassel, E. Massone, T. Taliercio, and Y. Boumaiza, J. Mater. Sci. **30**, 35 (1995).

[54] R.J.M. da Fonseca, J.M. Saurel, G. Despaux, A. Foucaran, E. Massone, T. Taliercio, and P. Lefebvre, Superlattices Microstruct. **16**, 21 (1994).

[55] D. Bellet, P. Lamagnere, A. Vincent, and Y. Brechet, J. Appl. Phys. **80**, 3772 (1996).

[56] L. J. Gibson and M.F. Ashby, *Cellular Solids: Structure and Properties* (Pergamon, New York, 1988).

[57] C.C. Matthai, J.L. Gavartin, and A.A. Cafolla, Thin Solid Films **255**, 174 (1995).

[58] K. Yamanaka, Jpn. J. Appl. Phys. **36**, 2939 (1997).

[59] H. Cho, H. Sato, H. Nishino, Y. Tsukahara, M. Inaba, A. Sato, M. Takemoto, S. Nakano, and K. Yamanaka, in *IEEE Ultrasonics Symposium: Proceedings*, edited by M. Levy, S.C. Schneider, and B.R. McAvoy (IEEE, New York, 1995).

[60] H. Cho, H. Sato, M. Takemoto, A. Sato, and K. Yamanaka, Jpn. J. Appl. Phys. **35**, 3062 (1996).

[61] W. Hayes and R. Loudon, *Scattering of Light by Crystals* (John Wiley and Sons, New York, 1978).

[62] P.M.A. Sherwood, *Vibrational Spectroscopy of Solids* (Cambridge University Press, Cambridge, 1972).

[63] S. Califano, *Vibrational States* (John Wiley and Sons, London, 1976).

[64] D. Steele, *Theory of Vibrational Spectroscopy* (W.B. Saunders Company, Philadelphia, 1971).

[65] M. Born and M. Bradburn, Proc. R. Soc. London, Ser. A **188**, 161 (1947).

[66] R. Loudon, Adv. Phys. **13**, 423 (1964).

[67] C. Kittel, *Introduction to Solid State Physics* (John Wiley and Sons, New York. 1986), p. 308.

[68] G.B. Benedek and K. Fritsch, Phys. Rev. B **149**, 647 (1966).

[69] K.R. Subbaswamy and A.A. Maradudin, Phys. Rev. B **18**, 4181 (1978).

[70] B.I. Bennett, A.A. Maradudin, and L.R. Swanson, Ann. Phys. (N.Y.) **71**, 357 (1972).

[71] R. Loudon, Phys. Rev. Lett. **40**, 581 (1978).

[72] N.L. Rowell and G.I. Stegeman, Phys. Rev. B **18**, 2598 (1978).

[73] A.M. Marvin, V. Bortolani, and F. Nizzoli, J. Phys. C **13**, 299 (1980).

[74] A.M. Marvin, V. Bortolani, F. Nizzoli, and G. Santoro, J. Phys. C **13**, 1607 (1980).

[75] R. Loudon and J.R. Sandercock, J. Phys. C **13**, 2609 (1980).

[76] J.R. Sandercock, Phys. Rev. Lett. **28**, 237 (1972).

[77] J.R. Sandercock, in *Light Scattering in Solids III*, edited by M. Cardona and G. Guntherodt (Springer-Verlag, Berlin, 1982).

[78] R. Loudon, J. Phys. C **11**, 403 (1978).

[79] A. Dervisch and R. Loudon, J. Phys. C **9**, L669 (1976).

[80] L.D. Landau and E.M. Lifshitz, *Theory of Elasticity* (Pergamon Press, Oxford, 1986), p. 92.

[81] G.W. Farnell, in *Acoustic Surface Waves*, edited by A.A. Oliner (Springer-Verlag, Berlin, 1978).

[82] G.W. Farnell, in *Physical Acoustics*, edited by W.P. Mason and R.N. Thurston (Academic Press, New York, 1970), Vol. 6.

[83] J.F. Nye, *Physical Properties of Crystals* (Clarendon Press, Oxford, 1972).

[84] W. Demtroder, *Laser Spectroscopy: Basic Concepts and Instrumentation* (Springer-Verlag, Berlin, 1982).

[85] J.R. Sandercock, in *Proceedings of the 2nd International Conference on Light Scattering in Solids*, edited by M. Balkanski (Flammarion, Paris, 1971).

[86] W.H. Press, B.P. Flannery, S.A. Teukolsky, and W.T. Vetterling, *Numerical Recipes in C* (Cambridge University Press, New York, 1988).

[87] O.L. Anderson, in *Physical Acoustics*, edited by W.P. Mason (Academic Press, New York, 1965), Vol. 3.

[88] N.C. Craig and I.W. Levin, Appl. Spectrosc. **33**, 475 (1979).

[89] J.C. Tsang, M.A. Tischler, and R.T. Collins, Appl. Phys. Lett. **60**, 2279 (1992).

[90] J. Kulda, D. Strauch, P. Pavone, and Y. Ishii, Phys. Rev. B **50**, 13347 (1994).

[91] G. Dolling, in *Inelastic Scattering of Neutrons in Solids and Liquids* (IAEA, Vienna, 1962).

[92] V. Bortolani, F. Nizzoli, G. Santoro, A. Marvin, and J.R. Sandercock, Phys. Rev. Lett. **43**, 224 (1979).

[93] P. Gupta, A.C. Dillon, A.S. Bracker, and S.M. George, Surf. Sci. **245**, 360 (1991).

[94] L.T. Canham, M.R. Houlton, W.Y. Leong, C. Pickering, and J.M. Keen, J. Appl. Phys. **70**, 422 (1991).

[95] T. Maruyama and S. Ohtani, Appl. Phys. Lett. **65**, 1346 (1994).

[96] A.S. Wagh, R.B. Poeppel, and J.P. Singh, J. Mater. Sci. **26**, 3862 (1991).

[97] T. Adachi, J. Mater. Sci. **25**, 4732 (1990).

[98] J.G. Berryman and P.A. Berge, in *Homogenization and Constitutive Modeling for Heterogeneous Materials, Proceedings of the Symposium on Homogenization and Constitutive Modeling for Heterogeneous Materials*, edited by C.S. Chang and J.W. Ju (ASME, New York, 1993).

[99] K.K. Phani, S.K. Niyogi, A.K. Maitra, and M. Roychaudhury, J. Mater. Sci. **21**, 4335 (1986).

[100] C. Delerue, M. Lannoo, G. Allan, and E. Martin, Thin Solid Films **255**, 27 (1995).